Microstructure and Mechanical Properties of Dissimilar Friction Stir Welding of AA6061-T6 and AA7075-T6 under Water Cooling Condition

Khosro Bijanrostami

Submitted to the
Institute of Graduate Studies and Research
in partial fulfillment of the requirements for the degree of

Doctor of Philosophy
in
Mechanical Engineering

Eastern Mediterranean University
August 2017
Gazimağusa, North Cyprus

Approval of the Institute of Graduate Studies and Research

Assoc. Prof. Dr. Ali Hakan Ulusoy
Acting Director

I certify that this thesis satisfies the requirements as a thesis for the degree of Doctor of Philosophy in Mechanical Engineering.

Assoc. Prof. Dr. Hasan Hacişevki
Chair, Department of Mechanical Engineering

We certify that we have read this thesis and that in our opinion it is fully adequate in Scope and quality as a thesis for the degree of Doctor of Philosophy in Mechanical Engineering.

Assoc. Prof. Dr. Ghulam Husain
Co-supervisor

Prof. Dr. Majid Hashemipour
Supervisor

Examining Committee

1. Prof. Dr. Murat Bengisu
2. Prof. Dr. Majid Hashemipour
3. Prof. Dr. Nurşen Saklakoğlu
4. Assoc. Prof. Dr. Qasim Zeeshan
5. Asst. Prof. Dr. Mohammed Basher A. Asmael

ABSTRACT

The application of aluminum alloys has been growing in the past decades in many industries. The main group of aluminum alloys, which are most often used, are the wrought alloys. With the growth of wrought alloys within the industries, the friction stir welding (FSW) of these materials has become attractive. Many alloys have been subjected to similar and dissimilar FSW in different ambient conditions. Recently, FSW conducted in water cooling (WC) condition has showed improvement in mechanical property of the welded joints. However, lack of research in joining of dissimilar alloys in WC condition is obvious.

In this dissertation FSW of dissimilar materials of AA6061-T6 and AA7075-T6 is investigated. The materials are meant to be in T6 (artificial aged hardening) condition. T6 materials are considerably harder and stronger due to formation of β phase (precipitates) unsolved in the supersaturated aluminum matrix during the hardening process. Properties of joined wrought aluminum alloys depend on FSW parameters due to generation of various heat signatures. Therefore, heat input during the process may count as a risk to the strength of materials if the generated heat is large and steady enough to dissolve the precipitates.

Aim of this dissertation is to investigate dissimilar FSW under WC condition with variable parameters of traverse and rotational speed and to find the optimized process parameters. Ultimate tensile strength (UTS) analysis and hardness (H) were obtained. In addition, microstructure analysis of the joints were evaluated by transmit electron microscope (TEM), optical microscope (OM) and scan electron microscope (SEM).

The results revealed that higher traverse speed and lower rotational speeds generate lower heat input which led to finer average grain size (D_{av}) thus larger H and UTS and lower elongation (El%). The grain boundaries and dislocations were identified as responsible for the higher H and UTS of the joints welded at lower heat input conditions. Moreover, the Hall–Petch relationship showed a deviation from its linear classical equation, which was due to the formation of substructures such as dislocations inside the grains. In comparison with the optimum condition, higher heat inputs caused grain growth and reduction in dislocation density and hence led to lower H and UTS and larger El%. The results show that by adopting WC FSW instead of FSW, 6% and 4% improvement in UTS and El% is achieved respectively. Furthermore, mathematical models were developed to predict the UTS, El%, H and D_{av} which are evaluated to be precise.

Keywords: Friction Stir Welding, Aged Hardened Aluminum Alloys, Water Cooling.

ÖZ

Alüminyum alaşımlarının uygulaması son yıllarda pek çok sanayide büyümektedir. En çok kullanılan alüminyum alaşım grubu, dövme alaşımlardır. Endüstride dövülmüş alaşımların kullanımının artmasıyle, bu malzemelerde sürtme karıştırma kaynağı (SKK) çekici hale geldi. Birçok alaşım farklı ortam koşullarında benzer ve farklı SKK'na tabi tutulmuştur. Son zamanlarda, su soğutmalı (SS) koşullarında yapılan SKK'larda, kaynak birleştirme yerlerindeki mekanik özelliklerinde iyileşme görüldü. Bununla birlikte, SS koşullarda farklı alaşımların birleştirilmesinde araştırma eksikliği vardır.

Bu tezde, benzer olmayan AA6061-T6 ve AA7075-T6 materyallerinin SKK'ları incelenmiştir. Malzemelerin T6 (suni yaşlanmış sertleştirilmiş) durumunda olması amaçlanmıştır. T6 malzemeleri, sertleştirme işlemi sırasında aşırı doymuş alüminyum matrisinde çözülmemiş β fazının (çökelti) oluşması nedeniyle oldukça sert ve daha güçlüdür. Birleştirilmiş dövme alüminyum alaşımlarının özellikleri, çeşitli ısı işaretlerinin oluşması nedeniyle SKK parametrelerine bağlıdır. Bu nedenle, işlem esnasında ısı girişi, üretilen ısı fazla ve çökeltileri çözecek kadar sabitse, malzemelerin mukavemeti açısından bir risk olarak sayılabilir.

Bu tezin amacı, SS koşullarda, değişken çapraz ve dönme hızı parametreleriyle farklı SKK'nı araştırmak ve optimize edilmiş proses parametrelerini bulmaktır. Kopma mukavemeti (KM) analizi ve sertliği (S) elde edilmiştir. Ayrıca, birleşme yerlerinin mikroyapı analizi, transmisyon elektron mikroskopu (TEM), optik mikroskop (OM) ve taramalı elektron mikroskopu (SEM) ile değerlendirildi. Sonuçlar daha yüksek

çapraz hız ve daha düşük dönme hızlarının daha düşük ısı girdisi oluşturduğunu ve bunun sonucunda daha küçük ortalama tane boyutuna (D_{av}) yol açtığını, böylece S ve KM'nin daha büyük olmasına ve daha düşük uzamaya (El%) yol açtığını ortaya koymuştur. Gren (tane) sınırları ve dislokasyonlar, düşük ısı girdi koşullarında, kaynakla birleştirilme yerlerinde olan daha yüksek S ve KM'den sorumlu olarak tanımlanırlar. Dahası, Hall-Petch ilişkisi, doğrusal klasik denkleminden sapma gösterdi, bu da, taneler içinde dislokasyonlar gibi altyapıların oluşmasından kaynaklanmıştır. Optimum koşulla karşılaştırıldığında, daha yüksek ısı girdileri tane büyümesine ve dislokasyon yoğunluğunda azalmaya neden oldu, bundan dolayı S ve KM'nin daha düşük olmasına ve El% 'e daha büyük olmasına yol açtı. Sonuçlar, SKK yerine SS SKK'nı benimseyerek sırasıyla KM'de ve El%'de % 6 ve % 4'lük iyileşme sağladığını göstermektedir. Ayrıca, KM, El%, S ve D_{av}'i kesin olarak tahmin etmek için matematiksel modeller geliştirildi.

Anahtar Kelimeler: Sürtünmeli Karıştırma Kaynağı, Yaşlanmış Sertleştirilmiş Alüminyum Alaşımları, Su Soğutma.

DEDICATION

I dedicate my dissertation work to the three ladies of my life. My mother, Batool Najirad, whose words of encouragement and push for tenacity ring in my ears. My Wife, Sheyda Hasanzadeh, who stood by me in every steps of my life and my sister, Soolmaz, who have never left my side and is very special to me.

ACKNOWLEDGMENT

Firstly, I would like to express my sincere gratitude to my supervisor and co-supervisor, Prof. Dr. Majid Hashemipour and Assist. Prof. Ghulam Husain, for their continuous support of my Ph.D study and related research, for their patience, motivation, and immense knowledge. Their guidance helped me in all the time of research and writing of this thesis.

Besides my supervisor, I would like to thank the rest of my thesis committee: Assoc. Prof. Dr. Qasim Zeeshan, Assist. Prof. Dr. Mohammed Bsher Asmael, for their insightful comments and also for the hard questions which incented me to widen my research from various perspectives.

My sincere thanks also goes to Assist. Prof. Dr. Reza Vatankhah Berenji, who provided me knowledge support and covered my lack of experience in publication which concluded to two journal publications. Without his precious support it would be much more complicated to conduct this research.

TABLE OF CONTENTS

LIST OF TABLES

LIST OF FIGURES

Chapter 1

INTRODUCTION

1.1 Overview

The Welding Institution invented FSW in 1991. It is a solid state joining process at which a non-consumable tool joins two adjacent work-pieces without melting them. In fact friction between work-pieces and the rotating tool generates heat which softens and mixes regions near the tool thus binds the work-pieces together [1]. This process is known as the most important development in joining of metals in its time [2]. It was such an energy efficient, green and adaptable welding technology [2] and also a prospering process in joining aluminum alloys that the application spread out quickly in various industries such as aerospace, ship, building, automotive and nuclear power-plants. FSW owes its success to its low heat input compared to elevated heat input in conventional fusion welding processes at which melting and recrystallization results in porosity, hot cracking and distortion [3].

From phase points of view, the heat generated by FSW in nugget zone (NZ) is the cause of dissolving large fraction of β phase (precipitates) and dislocation loss, formed during age hardening heat treatment process [4]. During FSW, there are two low hardness zones (LHZ) generated on both sides of the weld away from NZ. Several studies indicated that in FSW joining of precipitation hardened aluminum alloys the LHZ lies on heat affected zone (HAZ) due to significant precipitates dissolution as a

result of heat generated during FSW process [1, 2, 5, 6]. Thus, HAZs should be considered as the weakest area to determine the behavior of FSW joint.

1.2 Problem Statement

By vast application of wrought aluminum in industries and utilization of variety of alloys, joining of dissimilar materials seems to be necessary. One of the challenges of FSW of dissimilar aluminum alloys is different alloy characterization during welding process. Moreover, during welding process of heat treated wrought aluminum alloys heat generation has to be controlled and kept adequately. In fact anther challenge is about over heating of the base materials around the joining line. Therefore, cooling systems are deployed to extract the generated heat from the weldment and minimize precipitates dissolution as well as dislocation loss.

Aluminum alloys of 7000 series are known and applied in industries due to their elevated mechanical property compared with other series. Among aluminum alloys of 7000 series, 7075-T6 is the famous and available in the market around the globe. While, aluminum alloys of 6000 series have intermediate mechanical property, 6061-T6 is cheapest alloy than any other alloys in other series.

The objective of joining these two alloys is because of their close properties which enables the industries to substitute one by the other one when it is necessary [7]. In addition, as reported WC condition has significant effect on properties of FSW joint [8-10]. However, effects of WC condition on dissimilar FSW of AA7075-T6 and 6061-T6 in terms of heat generation, heat distribution and heat disposal pattern is still unclear.

1.3 Research Contribution and Objectives

In spite of enormous numbers of researches carried out on different conditions of FSW of various aluminum alloys, relatively few studies investigates FSW of dissimilar heat treated aluminum alloys under WC condition. The main contribution of this dissertation is investigating the mechanical properties, micro and macro structural characteristic of the welded joints of AA6061-T6 and AA7075-T6 under WC condition using FSW. The novelty of this dissertation is that the thermal histories of the joining processes are highlighted as the most influencing event. Thermal history related factors such as peak temperature and heating and cooling rates are interpreted and then correlated with the mechanical behavior and microstructure of the joints at different WC FSW parameters. Investigating wide range of welding parameters on twenty dissimilar joints shades a light to optimize joining parameters under the new condition. More specifically in analyzing the thermal history of the FSW joints, stablishing the parameters of heat generation rate, heat loss rate and the maximum heat for each joint is done for the first time and correlating them with the mechanical property and microstructure characteristics of each joint is a unique and novel method.

The main objectives of this dissertation are as following:

- To investigate the effects of different welding parameters on microstructure characterization of the NZ.
- To investigate the effects of different welding parameters on mechanical behavior of the joints.
- To correlate the effects of WC condition (heat generation & heat disposal pattern) at various FSW parameters on microstructure characterization and mechanical property of the joints.

- To stablish equations correlating FSW parameters with mechanical properties applicable for industries.

1.4 Research Methodology

The proposed methodology of this thesis contains three phases namely problem identification, research & development and Results & Comparison (Figure 1).

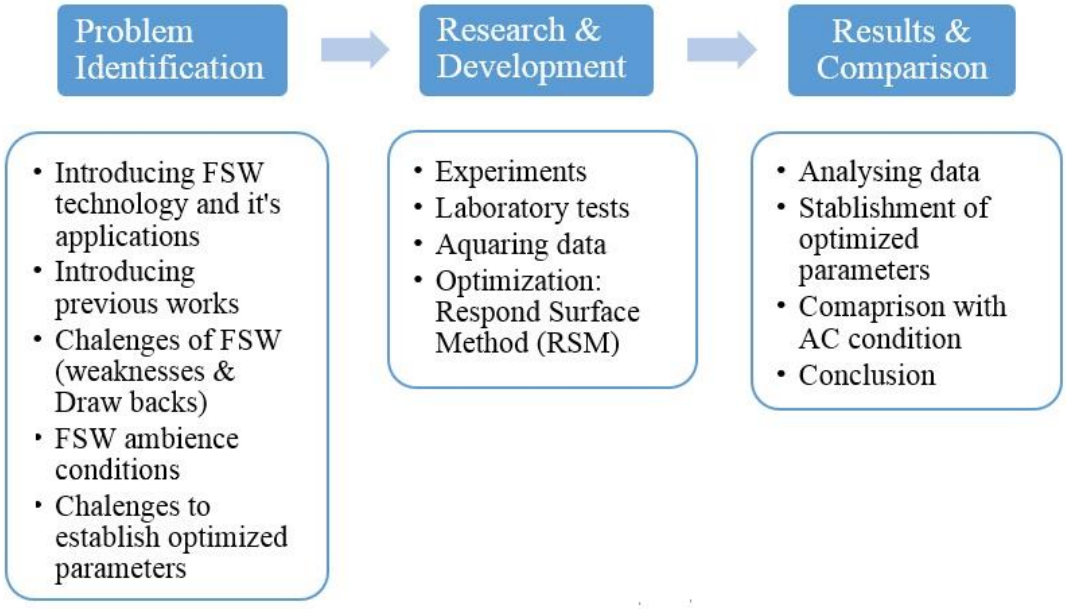

Figure 1: Proposed Methodology

1.5 Structure of This Dissertation

The rest of this research is organized as following:

- Chapter 2 is the literature review of the research which also proposes the aim and contribution to science.
- Chapter 3 is the methodology of the research which include setup of the experiment align with introduction of base materials, tool selection, fixture design, thermocouple setup and FSW parameters as well as procedures of conducting tensile test, hardness test and metallographic studies.

- Chapter 4 demonstrates the results of the thermal fluctuation during WC FSW process, mechanical tests and metallographic studies. Moreover, this chapter analysis the results and describes the correlation between them.
- Chapter 5 discusses findings and methods of optimizations.
- Chapter 6 is the conclusion of the research.
- Chapter 7 offers the possible areas as future work.

The results of this dissertation are published in two journals as bellow:

- K. Bijanrostami, R. V. Barenji, M. Hashemipour, "*Effect of Traverse and Rotational Speeds on the Tensile Behavior of the Underwater Dissimilar Friction Stir Welded Aluminum Alloys*", Journal of Materials Engineering and Performance, 26(2), 2017, p 909-920.
- K. Bijanrostami, R. V. Barenji, "*Underwater dissimilar friction stir welding of aluminum alloys: Elucidating the grain size and hardness of the joints. Proceedings of the Institution of Mechanical Engineers*", Part L: Journal of Materials: Design and Applications, 0(0), 2017, p 1–13

Chapter 2

LITERATURE REVIEW

2.1 Aluminum and Its Alloys

Aluminum is the third most abundant element in the Earth's crust and constitutes 7.3% by mass. In nature, however it only exists in very stable combinations with other materials (particularly as silicates and oxides) and it was not until 1808 that its existence was first established [11].

The metal originally obtained its name from the Latin word for alum, alumen. The name alumina was proposed by L.B.G de Morev eau, in 1761 for the base in alum, which was positively shown in 1787 to be the oxide of a yet to be discovered metal. Finally, in 1807, Sir Humphrey Davy proposed that of aluminum so to agree with the "ium" spelling that end most of the elements [11].

Aside from steel and cast iron, aluminum is one of the most widely used metals owing to its characteristics of lightweight, good thermal and electrical conductivities. Despite these characteristics, however, pure aluminum is rarely used because it lacks strength. Thus, in industrial applications, most aluminum is used in the form of alloys [11].

There are a number of elements that are added to aluminum in order to produce alloys with increased strength and improved foundry or working properties. In addition to alloying aluminum with other elements, the mechanical properties can also be

enhanced by heat treatment. Generally, aluminum alloys can be classified into two main categories: cast alloys and wrought alloys [11].

2.1.1 Casting Alloys

These alloys suffer from higher shrinkage (up to 7%) which occurs during cooling or solidification. Higher mechanical properties in these alloys can be achieved by controlling the level of impurities, grain size, and solidification parameters such as the cooling rate [11].

A system of four-digit numerical designation is used to identify aluminum and aluminum alloys in the form of castings and foundry ingots. The first digit indicates the alloy group as shown in Table 1. The second and third digits identify the aluminum alloy or indicate the minimum aluminum percentage. The last digit, which is to the right of the decimal point, indicates the product form: XXX.0 indicates castings, and XXX.1 and XXX.2 indicate ingots [11].

Table 1: Cast aluminum alloy groups

Aluminum 99% minimum and greater	1xx.x
Aluminum alloy with major alloying elements as copper	2xx.x
Manganese	3xx.x
Silicon	4xx.x
Magnesium	5xx.x
Magnesium	6xx.x
Zinc	7xx.x
Other element	8xx.x
Unused	9xx.x

2.1.2 Wrought Alloys

These are alloys are shaped using certain working processes and are used as rolled plates, sheet metal, foil, extrusion tubes, rods, bars and wire. Wrought alloys are also designated by a four digit system as presented in table 2. Both wrought and cast aluminum alloys are divided into alloys which can be heat treated (in order to increase the mechanical properties) and alloys which cannot be heat treated [11].

Table 2: Wrought aluminum alloy groups

Aluminum 99% minimum and greater	1xxx
Aluminum alloys with major alloying elements copper	2xxx
Silicon, with added copper and / or magnesium	3xxx
Silicon	4xxx
Magnesium	5xxx
Unused series	6xxx
Zinc	7xxx
Tin	8xxx
Other element	9xxx

2.2 Friction Stir Welding

Friction Stir Welding is a solid state joining process at which a non-consumable tool joins two adjacent work-pieces without meting them. This process is performed by friction between work-pieces and the rotating and traversing tool which generates heat. The generated heat softens the facing materials and facilitates mixing regions near the tool thus binds the work-pieces together [1]. Therefore, the heat generated in FSW plays the most important role in the joining process [4]. The generated heat as the most

significant welding parameter is a function of some other parameters such as; rotational speed, traverse speed, base materials properties, plunging depth, tool geometry, tilt angle and welding ambient condition. While the rotating tool is traversing on the joining line, the plunged pin traverses through the facing work-pieces and the tilted shoulder pulls the surface of the materials down thus applies axial force. As illustrated in the figure 2-i, the tool's pin is plunged in the joining line of the materials until the tilted shoulder hits the surface and applies adequate force shown in 2-ii. The applied force magnifies the friction thus, increases the heat. Moreover, the tilt angle helps the tool to pull the material down and stir the softened material more effectively. Figure 2-iii shows the stirring phenomenon as the tool traverses on the joining line. Figure 3-vi demonstrates schematic of the cross section of the joint in which zones labeled as "D, C, and B" are the NZ, HAZ and TMAZ respectively. Furthermore, there is another section unaffected zone labeled as "a" in the figure 2-i.

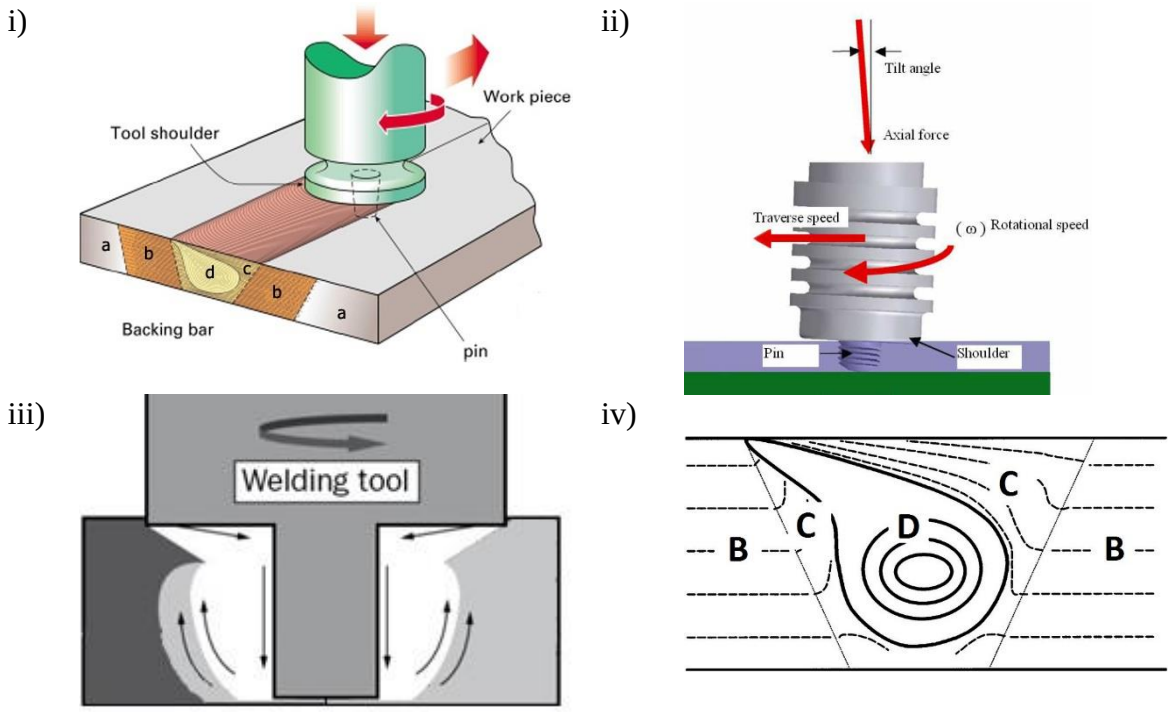

Figure 2: Schematic Views of FSW Process [12] i)Perspective View ii)Side View iii)Stirring Action iv)Zones Formation

NZ is a region of superplastic deformation as a result pin plunged in and thus forms the onion rings. The grains within the stir zone are equiaxed and often an order of magnitude smaller than the grains in the base materials [1, 13-15]. TMAZ forms on both sides of the NZ at which the temperature is mostly lower and the stirring is also much lower. The microstructure of these regions is recognizably that of the base materials [9]. HAZ occurs on both sides of the weld adjacent to the TMAZ. This region is only subjected to the thermal cycle and no deformation takes place [4].

2.3 Dissimilar Joints by FSW

Joining of dissimilar aluminum alloys by FSW is associated with many complications and challenges. These issues are caused by differences in mechanical, chemical and thermal properties of the alloys which led to differences in respond to applied mechanical and thermomechanical tensions. Moreover, on nugget zone a new type of metal matrix composite will be formed which indeed has its own property.

Dissimilar friction stir welding of AA6061-T6 and AA7075-T6 for the first time has been reported by Guo [7] with a tool consisted of 15 mm shoulder diameter and 5 mm pin diameter. Process parameters were; constant rotational speed and variable traverse speed of 160 to 300 mm/min and different positioning. In addition, the temperature history profiles of the slabs were captured during the joining process in three spots of close to NZ, HAZ and TMAZ. Objectives were to investigate, the effects of traverse speed and materials position on the tensile property, microstructure, microhardness distribution and material flow of the joints. Results showed that the material mixing is much more effective when AA7075 alloy was located on the retreating side. It was found that the tensile strength of the dissimilar joints increases with decreasing heat input. The highest joint strength was obtained when welding was conducted with

highest welding speed and AA7075 Al plates were fixed on the retreating side. At the end microstructure observations were analyzed trough their temperature histories and correlated with mechanical performance of the joints.

The formation of a new intermediate material based on mixture of dissimilar alloys, mechanical and metallurgical characterization of FSW in one hand and comparison between similar material joint and dissimilar material in another hand interested many researchers. As example, mechanical and metallurgical characterization of friction stir welded butt joints of AA6061-T6 with AA6082-T6 is investigated by Moreira et al. [16]. For comprehensive comparison between similar and dissimilar joints, the authors made two similar material joints from each one of the two base alloys. To join the plates a tool consisted of 17 mm shoulder diameter and 5 mm pin diameter. The constant FSW parameters were traverse speed, rotation speed and tilt angle which were 1120 mm/min, 224 rpm and 2.5˚ respectively. The tests included microstructure, microhardness, tensile and bending tests of all joints. The results showed that the FSW of dissimilar joint present intermediate mechanical properties compared with each base material.

Muruganandam et al. [17] draw a similar conclusion by investigating the mechanical and microstructural properties of FSW joining of dissimilar AA2024-T3 and AA7075-T6. Process parameters were kept constant; traverse speed of 1200 mm/min, rotation speed 160 rpm and tilt angle of 2˚ with a tool consisted of 20 mm shoulder diameter and 6 mm pin diameter. In order to analyze the mechanical response of the joints, they were tested under tension and fatigue endurance. The microstructure of the joints studied by OM and SEM either on welded and ruptured specimens. The results revealed the tensile strength of the welded joints perform 80% of what in base

materials. The microhardness distribution was in a typical “W” shape. Although, the presence of the FSW line reduces the fatigue behavior, compare to the parent materials is acceptable and allows considering the FSW as an alternative joining technology for the aluminum plate alloys.

Palanivel et al [18] applied FSW to join dissimilar aluminum alloys AA5083-H111 and AA6351-T6. The aim was to study effect of tool rotational speed and pin geometry on the microstructure and tensile strength of the joints. Dissimilar joints were produced applying three different tool rotational speeds (600, 950 and 1300 rpm) and five different tool pin geometry (straight square, straight hexagon, straight octagon, tapered square and tapered octagon). The results of observations in three different regions of NZ, HAZ and TMAZ revealed that the tool rotational speed and tool geometry have significant influenced on microstructure and tensile strength of the joints. The joint fabricated applying tool rotational speed of 950 rpm and straight square pin geometry resulted highest tensile strength. The two FSW parameters affected the joint property due to variations in material flow behavior, loss of cold work in the HAZ of AA5083 side, dissolution and over aging of precipitates of AA6351 side and formation of macroscopic defects in the weld zone.

Cavaliere et al. [19] studied the effect of FSW parameters on the mechanical and microstructural properties of dissimilar joints of AA6082 and AA2024. Multiple joints were produced by a constant rotational speed of 1600 rpm, two different traverse speeds of 80 and 115 mm/min and also different alloy position. Contrary with the other literatures, the joining line of the welds were kept perpendicular to the rolling direction for both alloys. Microhardness and tensile tests conducted to evaluate the mechanical properties of the joints. Moreover, to analyze the microstructural evolution of the

alloys, the joint cross-sections were observed optically. SEM observations were also made of the fracture surfaces. Results showed formation of various vortex-like structure resulted as different FSW configuration in the center of the welds. The best tensile property were obtained for the joints with the AA6082 on the advancing side and welded with the traverse speed of 115 mm/min.

Khodir et al. [20] focused on the microstructure and mechanical evolution of dissimilar joints of AA2024-T3 and AA7075-T6 produced by FSW. Joints were produced by a constant rotational speed of 1200 rpm and four stages of traverse speed of 42, 72, 102 and 198 mm/min and variable alloy positioning. The tool was consisted of a 12 mm shoulder diameter and a 4 mm pin diameter. Microstructures of various regions of welds were observed in the cross-section of the joint by optical microscopy. The homogeneity of constituents in the NZ was analyzed by SEM-EDS method. Microhardness and tensile tests were carried out. Effect of traverse speed on microstructures, hardness distributions, and tensile properties of the welded joints were investigated. SEM-EDS analysis revealed that the stir zone contains a mixed structure and onion ring pattern with a periodic change of grain size as well as a heterogeneous distribution of alloying elements. The best tensile strength was achieved for the joint produced at welding speed of 1.67 mm/s when 2024 Al alloy was positioned on the advancing side.

Amancio-Filho et al. [21] worked on dissimilar FSW of AA2024-T351 and AA6056-T4. Joints were produced by varying the rotational speed of 500 to 1200 rpm and the transverse speed of 150 to 400 mm/min. The tool was consisted of a 15 mm shoulder diameter and 5 mm pin diameter. The aim was to optimize the joining process based on the results of macrographic analysis and microhardness testing. Results indicated

that the best joint obtained by rotational speed of 800 rpm and transverse speed of 150 mm/min. OM and SEM observation revealed the presence of a lamellar material flow pattern due to the differential flow of materials. High level of strain and temperatures usually over 400˚C, resulted in a dynamically recrystallized stirred zone with refined grains. Tensile testing has shown that strength is up to 90% of the weakest joining partner 6056-T4. Fracture took place in the TMAZ of the alloy 6056-T4, where annealed structure led to decrease in microhardness.

2.4 Water Coolant Condition

Employing the FSW for joining aluminum alloys facilitate more successful joining process compared to conventional welding process at which melting and recrystallization led to severe defects. In spite of considerable reduction of heat generated during FSW. Controlling the heat disposal seems to be even more beneficial for heat treated aluminum plates. Aged hardened materials are considerably harder and stronger due to formation of β phase (precipitates) in the supersaturated aluminum matrix during the hardening process [11]. The precipitates may dissolve in the matrix under the application of heat and return the material into its original condition [22]. Therefore, heat input during the FSW process may count as a risk to the strength of material if the generated heat is large and steady enough to dissolve the precipitates.

WC FSW refers to FSW process occurring under the water. Figure 3 illustrates the water submerged process configuration.

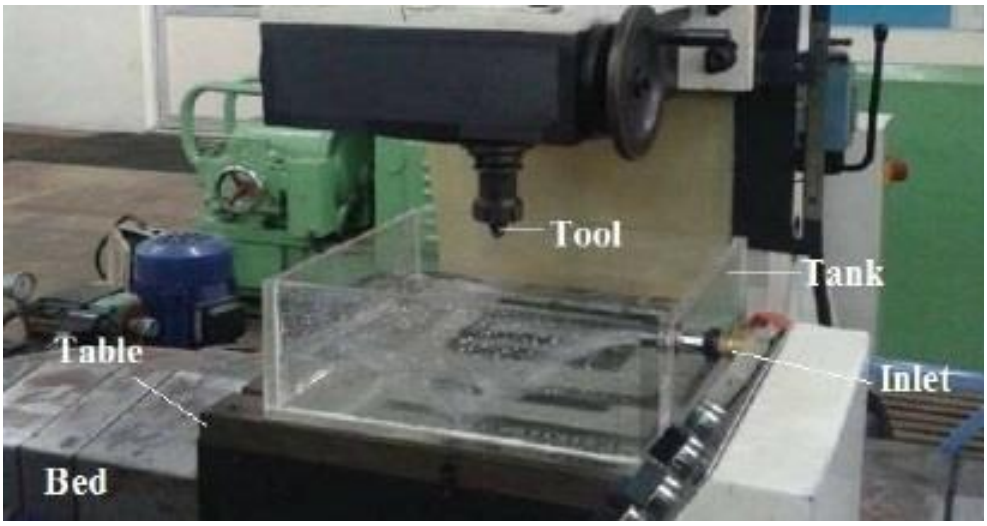

Figure 3: WC FSW Process Configuration [23]

This ambient condition has considerable effect on exposure of generated heat as the most significant FSW parameter. Unlike the FSW this concept has not been studied deeply. The sheets are fixed inside of a tank filled by water and the tool FSW process is conducted under WC condition.

FSW in three ambient conditions (air cold and hot water) was carried out for AA7050 by Fu et al [8]. The tool consisted of a 12 mm shoulder diameter and 6mm pin diameter. Traverse and rotational speed were kept constant; 100 mm/min and 800 rpm respectively. Transverse distributions of the microhardness of the joints were measured, the thermal histories of the joints were acquired from four spots on each side and their tensile properties were tested. The fracture surfaces of the tensile specimens were observed, and the microstructures at the fracture region were investigated. The peak temperature recorded during welding in air, cold and hot water were about 380, 220 and 300 °C, respectively. The microhardness distributions were a typical ‘‘W’’ shape. The best tensile property was achieved for joint welded in hot water with 92% of the base material strength. Similarly Zhang et al. [24] conducted FSW in two ambient conditions of air cooling (AC) and WC for AA2014-T6 at a

constant rotational speed of 800 mm/min and variable traverse speeds between 100–800 rpm. The tool consisted of a 20 mm shoulder diameter and an 8 mm pin diameter. The results showed successful joints obtained at all ranges of traverse speed under AC condition while under WC condition defect-free joint was only obtained under the minimum traverse speed of 100 mm/min and higher traverse speeds were not successful. Although the thermal histories were not recorded, the presence of thermal cycles led to formation of LHZ on both retreating and advancing sides. For the AC joints tensile strength increased by increase in traverse speed from 100 to 800 mm/min while results for WC joint indicated no enhancement on the hardness of LHZs and tensile strength of the joints.

Fratini et al [25] experimentally and numerically investigated the effects of WC treatment aimed to enhance the quality of FSW butt joints in terms of mechanical properties and metallurgy of the processed material. The tool consisted of 12 mm shoulder diameter and 4 mm pin diameter. For each of traverse speed and rotation rate two values were considered, 105 and 214 for traverse speed and 715 and 1500 for rotational rate. Results admitted the previous literatures; joint under WC condition found to be enhanced in strength. In addition, reducing the material softening usually observed in the thermo-mechanically affected zone area, with no harm on nugget integrity.

2.5 The Aim and Contribution of This Dissertation

Since invention of FSW, enormous researches carried out on FSW joining of similar aluminum alloys, however, FSW joining of dissimilar aluminum alloys was not investigated as many. Furthermore, only few literatures have considered dissimilar FSW joining under WC condition. Similar to this dissertation, Guo et al. [7] exposed

dissimilar FSW joining of AA6061 and AA7075, however, the heat treated base material and side effects on second phase particles is missing on the project. Moreover, their research did not cover FSW under WC condition.

The main contribution of this dissertation is more deeply investigating the mechanical properties, micro and macrostructural characteristic of the dissimilar welded joins of AA6061-T6 and AA7075-T6 under WC condition using FSW. In order to full fill the research on the early mentioned context, this dissertation is going to conduct comprehensive practical experiments and produce dissimilar joints under WC condition with variable parameters of; rotational speed and traverse speed and adequate constant parameters of tilt angle, tool geometry, axial force and positioning. Parameters of rotational speed and traverse speed are meant to be variable as the most influencing parameters and the values are selected from the studied literatures in literature review. The selection of range of variable parameters was in a manner to cover the wide range of variation in literatures used for both similar and dissimilar aluminum alloys as well as for AC and WC conditions. Similarly, the values of constant parameters are selected based on the optimum results of previous studies. For instance, in spite of importance of tilt angle role in stirring of materials under tool, the value has proven to be optimum in the range of 2 to 2.5 degree for all types of aluminum alloys [7, 10, 16, 24 and 25]. For positioning, it is proven in literatures that the optimum tensile strength is obtained when AA6061-T6 is positioned on advancing side as the softer alloy [7, 26].

While producing joints, thermal histories of both sides, advancing side and retreating side, will be acquired to be then analyzed and correlated with the joint's microstructures and other mechanical properties. Moreover, surface respond method

is employed to predict optimized values for variable parameters. Finally, mechanical performance of the optimized joint will be compared with the optimized joint of other literatures under AC condition.

Chapter 3

METHODOLOGY

3.1 Experimental Setup

The base materials studied in this dissertation were 5 mm thick (common thickness used in industries and available in the market) rolled plates of AA6061-T6 and AA7075-T6 both in artificially aged heat treated condition. As represented previously in the last chapter, selection of these base materials in T6 condition was to determine the side effects of WC FSW on second phase particles as well as dislocations formed at aged hardening heat treatment process. Therefore, it comes to importance to check for authenticity of the base materials first. It was done through chemical and mechanical tests. The chemical compositions of the base materials were tested in accordance with ASTM E8M-9. In order to prepare samples for chemical composition test, two square pieces of 20mm×20mm are cut from different randomly selected portion of each base material and surface grinded to remove aluminum oxide and other possible pollutions. Then, the two results of each sample were compared and average was presented. Tensile specimens were cut normal to the rolling direction in accordance with ASTM E8M-9. Tensile tests were carried out by Gothech-30T at room temperature with the strain rate of 1mm/min. Macrohardness tests were performed by InnovaTest 400 in accordance with ASTM E8M-9; load of 1kgf for 5 seconds. Table 3 presents the results of tensile, macrohardness and chemical composition tests performed on the base materials and compared with standard

properties [27]. Moreover, thermal properties of the base materials is presented based on the standard values [27].

Table 3: Mechanical Properties and Chemical Composition of the Base Materials

		AA6061-T6		AA7075-T6	
		Standard	Tested	Standard	Tested
Chemical Composition (wt.%)	Al	95.8 – 98.6	96.52	87.1 – 91.4	89.72
	Mg	0.8 – 1.2	1	2.1 – 2.9	2.1
	Si	0.4 – 0.8	0.5	Max 0.4	0.4
	Cr	0.04 – 0.35	0.3	0.18 – 0.28	0.2
	Fe	Max 0.7	0.7	Max 0.5	0.34
	Cu	0.15 – 0.4	0.3	1.2 – 2	1.8
	Zn	Max 0.25	0.25	5.1 – 6.1	5
	Ti	Max 0.15	0.1	Max 0.2	0.15
	Mn	Max 0.15	0.15	Max 0.3	0.12
	Other each	Max 0.05	0.04	Max 0.05	0.05
	Other total	Max 0.15	0.14	Max 0.15	0.12
Mechanical Properties	Macroardness (vickers)	107	105	175	200
	UTS (MPa)	310	302	572	600
	Elongation (%El)	12	10.9	11	13.1
Thermal Properties	Melting point (°C)	582 - 652	-	477 - 635	-

The base materials were then cut by power hacksaw cutting machine and milled to get the required size of 150mm×100mm. Rectangular butt joint configuration was then prepared to fabricate WC FSW joints. The initial joint configuration was obtained by positioning AA60601-T6 on advancing side and AA7075-T6 on retreating side and holding them on top of a steel backing plate. The baking plate was machined to have

2.5˚ angled surface along the FSW traverse direction. The decline surface of backing plate was associated with the same descend of the tool during the process to play the role of the tilt angle. This set were then put inside of a tank filled with water where the configured set was secured and tightened to the CNC bed using mechanical clamps as illustrated in figure 4.

Figure 4: WC FSW Setup

The direction of welding was normal to the rolling direction and along with slope of the backing plate's surface. A single descending pass has been used to fabricate the joints. The amount of downward movement was calculated based on the tilt angle (2.5˚) and length of the joint (150mm).

At the initial investigation the FSW samples contained four different regions as shown schematically in figure 5. They are as: (a) unaffected base metal (b) HAZ (c) TMAZ and (d) NZ.

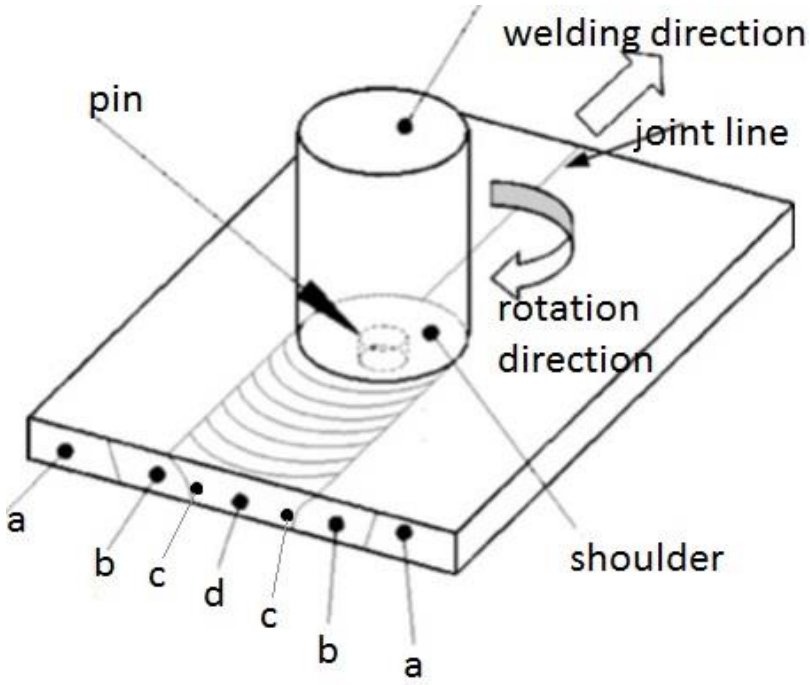

Figure 5: Welding Schematic

In order to measure the welding temperature and plot the profile for each joint, there were 3 thermocouples located at TMAZ, HAZ and unaffected zone of each side using K-type thermocouples [7, 22] with a 0.25mm diameter wire. Therefore, three holes were drilled at 5mm, 10mm and 15mm away from the joining line. Drilling was performed with 2mm diameter drill bit to the depth of 3mm.

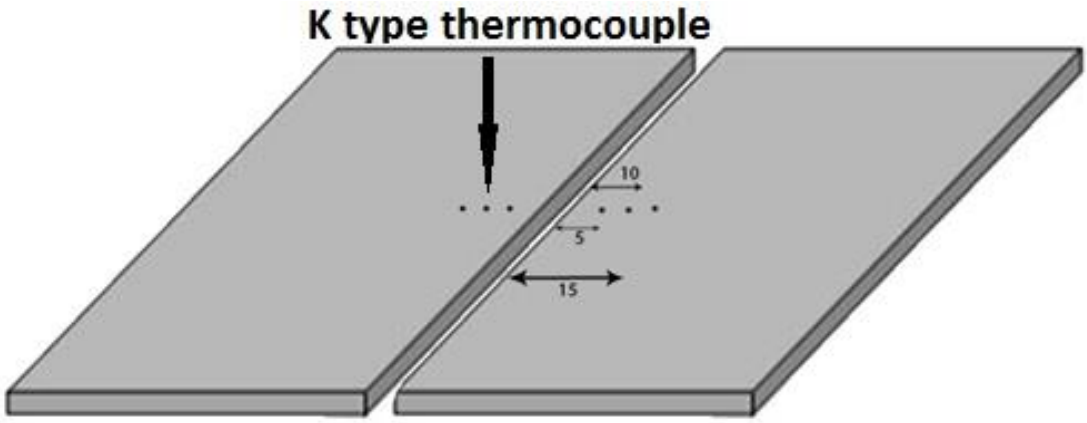

Figure 6: Schematic view of the holes drilled at the bottom surfaces of the plates

Then thermocouples were fixed into the holes with short bars of 1.8mm diameter Al filler wire. The filler wires were then mechanically punched to improve the contact between the thermocouples and workpieces.

No special treatment was carried out after welding and before testing. The material received in T6 condition and subsequently welded and tested immediately without any delay. In order to fabricate the joints, a non-consumable tool made of 2344 steel (heat treat able and hot working steel) [28] has been machined to have a threaded conic pin. Pin conic angle was considered to be 5 degree while the length was 4.5mm with maximum diameter of 5mm and the shoulder diameter was 15mm [7]. Then it was subjected to heat treatment to improve hardness up to 52 Rockwell C. Schematic and perspective views of the tool are shown in figure 6.

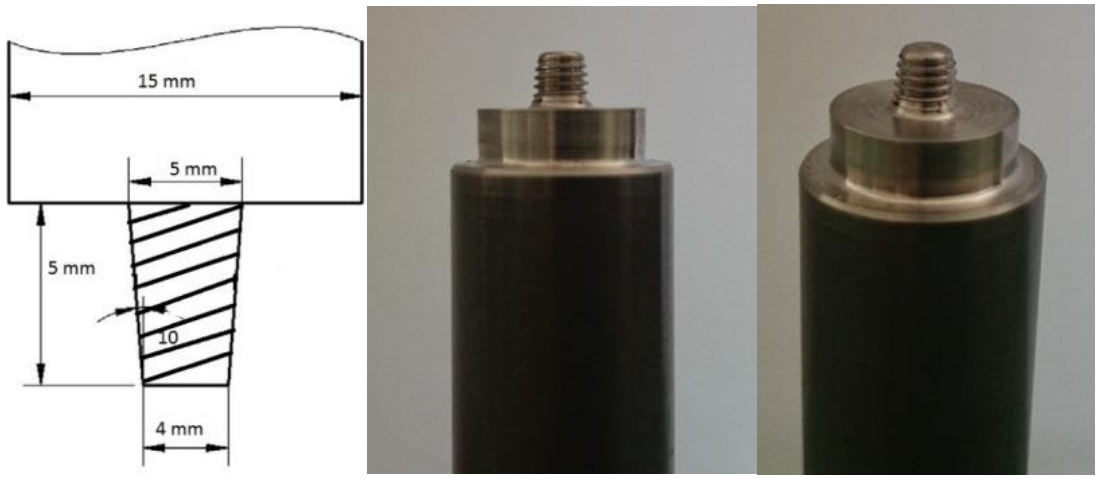

Figure 7: Tool geometry

3.2 Design of Experiment

A Dugard 3 axis CNC machine was employed to power up the tool and fabricate the joints. As mentioned in the previous chapter two parameters of traverse speed and rotational speed were meant to be variable and constant values for the other

parameters. Variable ranges of rotational speed (1000 rpm – 2500 rpm) and feed rate (50 mm/min – 350 mm/min) have been selected to fabricate 18 joints while the plunging depth of 0.4mm, the tilt angle of 2.5 degree and positioning were kept constant. The experiment was planned and comprehensively designed through 18 runs by expert design software (EX7). Full Factorials method of design of experiments (DoE) was used to create the experiment configuration, in terms of process parameters. The characteristic of these test samples will cause to achieve desirable characteristics of FSW joints. DoE reduces the numbers of experiments without any significant loss in the accuracy of the models developed. In addition, the developed test samples will be useful in predicting the effect of each response. It will also aid in the selection of the optimum process parameters to maximize or minimize the various response. Table 4 presents the DoE Coded and Actual Values of Parameters while table 5 presents DoE plan with the relative parameters.

Table 4: DoE Coded and Actual Values of Parameters

level	parameters	
	Traverse Speed (A) (mm/min)	Rotational Speed (B) (Rpm)
-1	50	1000
-0.5	125	1375
0	200	1700
0.5	275	2125
1	350	2500

Table 5: DoE Plan

Joint	Traverse speed (mm/min)	Rotational Speed (rpm)	Joint	Traverse speed (mm/min)	Rotational Speed (rpm)
1	50	2500	10	200	1750
2	350	2500	11	200	2500
3	275	1375	12	350	1750
4	200	1750	13	50	1000
5	200	1000	14	125	2125
6	275	2125	15	50	1750
7	50	1000	16	350	1000
8	350	1000	17	350	1750
9	350	2500	18	125	1375

Design-Expert (V7) is also used to predict the following responses:

- Joint strength
- Joint hardness

The developed models will be presented in various plots (such as, 2D plots and contour graphs). These plots and graphs will explain the effect of the precipitation parameters and their interactions on the above-mentioned responses.

Figure 8 shows the flowchart of the optimization stages in the Design Expert software.

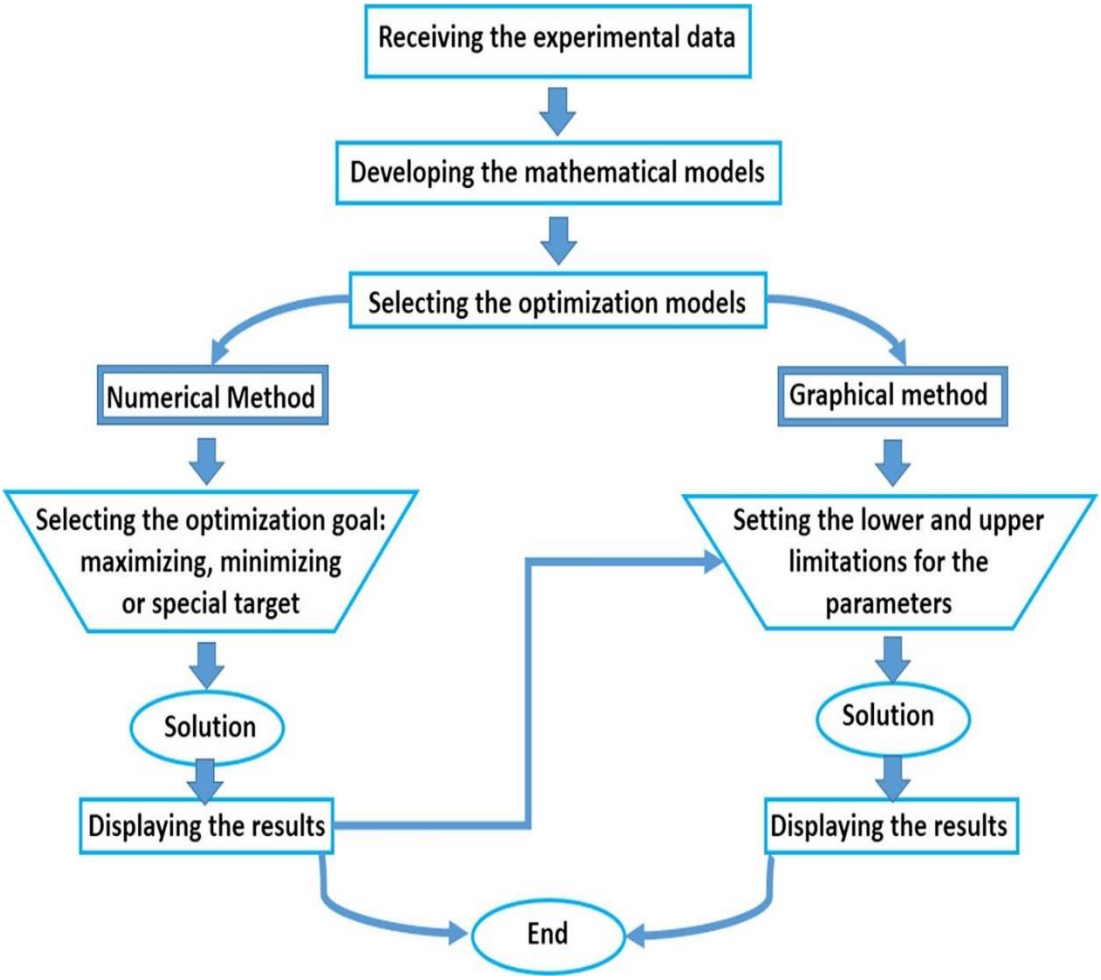

Figure 8: Flowchart of the optimization steps

3.3 Temperature Measurement

The temperature of the desired locations were read and recorded at 1second sampling intervals using OMEGA digital data logger with eight channels. The device was equipped to auto calibrate option and was used for calibration. The temperature history profile of the nugget zone was not measured due to difficulties in positioning the thermocouples however the temperature of the closest position to the NZ can be assumed as NZ temperature with a good approximation due to high thermal conductivity of the base materials. Moreover, a thermocouple was fixed near the traversing tool to record the water temperature.

3.4 Metallographic Inspection

Characterization of macrostructures was performed on the cross section of the joints using Meiji OM at 10× magnification. The samples were cut normal to the welding direction and polished based on metallographic polishing procedure. The polished surfaces were then etched in Keller's reagent (mixture of 2.5 ml nitric acid, 1.5 ml hydrochloric acid, 1 ml hydrofluoric acid and 95 ml water) for 20 seconds. Grain structures were also examined by OM, Olympus-MPG3. The average grain sizes were measured by the mean liner intercept technique (grain size = mean layer intercept×1.78). In order to demonstrate density of dislocations in the weakest area, TEM examination was carried out. TECNAI20 was employed and disk specimens were cut from LHZs and then electron transparent thin sections were prepared by double jet electro-polishing with a solution of 30% nitric acid in methanol (18 V and -35 ^{o}C). The TEM image analyses were conducted on [001] Al zone axis orientation.

3.5 Macrohardness Tests

Hardness specimens were cut normal to the weld direction from the center of the joint length by power hacksaw. The cut off cross sections were then grinded and polished to get smooth and parallel surfaces ready for hardness test. Note that, coolant was used during all the specimen preparation processes to take away the heat generated and prevent any modifications in the joint structure. Vickers Macrohardness test was performed on the polished cross section with the load of 1 kg by Wolfert722-N. Macrohardness was measured at 13 points on two lines on the thickness of the joint. The first line was 1.5mm below the top surface and the second line 1.5mm above the bottom surface. The arrangement of the index points was; one at the joint line six more on each side 2 mm away from the adjacent indent. So that 12 mm on both sides

undergoes macrohardness test which covers all the regions of NZ, TMAZ, HAZ and base materials.

3.6 Tensile Test

Once all the joints were successfully welded, a tensile test specimens was cut out (as shown in figure 9) from each joint in accordance with the same standard as used for the base materials (ASTM E8M-9).

Figure 9: Tensile specimen configuration

They were cut normal to the welding direction and top and bottom surfaces of the specimens were then grinded and polished to lose the onion rings marks left from welding process, un-welded left over on bottom and meet the standard thickness [29, 30]. Note that, coolant was used during all the specimen preparation processes to take away the heat generated and prevent any modifications in the joint structure. Specimens were then pulled by Gothech-30T universal tensile test machine at room temperature with strain rate of 1mm/min. Once a test is completed the specimen fractured parts are put back together and elongation is measured. Fractured specimens were then stored for further fractography investigation.

Chapter 4

RESULTS AND ANALYSIS

4.1 Introduction

The results and analysis of the joining process carried out in variable traverse speed and rotational speed other constant parameters such as tilt angle, tool geometry and positioning is presented in detail in this chapter. The values of the constant parameters are adopted from the optimum results selected from article [7, 10, 16, 24-26]. For instance, positioning the AA6061-T6 in the advancing side as the softer material makes the material turbulence much more effective, especially at higher feed rates [7, 26].

DoE was used to create the joint test samples, in terms of process parameters. The developed test samples are used to predict the effect of responses of the process characteristic. It also aids in selection of the optimum process parameters or, maximizing or minimizing the various responses. In general, the prominent goal in developing mathematical models, with the aid of Design-Expert (V7) statistical software is the prediction of the following responses:

- Joint strength
- Joint hardness

The developed models are presented in various plots (such as, 2D plots and contour graphs). These plots and graphs explain the effect of the precipitation parameters and their interactions on joint strength and hardness responses.

4.2 Temperature Profile

FSW is basically a thermo-mechanical process where the materials experience a thermal cycle and mechanical mixing simultaneously. It is well reported in the literatures that in FSW, microstructure evolution strongly depends on temperature history due to influence of localized thermal hysteresis on distribution, amount and size of precipitates [4, 5, 8]. Figures placed in appendix A (run 1 to 18) show the thermal profiles of FSW process.

As an example in thermal profile of joint 1 with traverse speed of 50 mm/min and rotational speed of 2500 rpm; heating and cooling rate of the joint are 16.5 C°/s and 15.4 C°/s respectively. The maximum amount of temperature occurred approximately on 420-430 C° domain. Table 6 provides a collection of thermal information of all samples it shows the maximum heat exposed to the TAMZ and HAZ. It also reveals which side experienced higher temperature as well as heating and cooling rate of each joint. Since the rate of heating and cooling play a significant role on the structure of materials, these values are extracted from the graphs, reported and analyzed. It shows the maximum heat input of three main zones (TMAZ, HAZ and the base, except NZ due to difficulties to precisely positioning thermocouples) of weldment in both sides and the heat input and output rate. Graphs reveal strong correlation between traverse speed and heating rate and insignificancy of rotational speed to both heating rate and max heat generation. It was expected to get asymmetric temperature profile at each side during FSW [7, 31], due to the characteristics of FSW process which poses more heat to the advancing side.

Table 6: Extract of Thermal Histories of Entire Experiments

Join	Rep	Traverse Speed (mm/min)	Rotational Speed (rpm)	Max. Heat Input				
				Side	TMAZ (°C)	HAZ (°C)	Heating Rate (°C/s)	Cooling Rate (°C/s)
1	2	50	2500	Retreat	417	285	16.5	15.4
2	2	350	2500	Retreat	383	221	78	84
3	1	275	1375	Advance	409	257	100	63
4	2	200	1750	Retreat	415	279	58	48
5	1	200	1000	Retreat	378	248	74	51
6	1	275	2125	Retreat	405	256	89	70
7	2	50	1000	A/R	389	252	19	12
8	2	350	1000	Retreat	363	219	110	85
9	2	350	2500	A/R	396	248	141	56
10	2	200	1750	Retreat	395	267	80	41
11	1	200	2500	Retreat	395	223	64	54
12	1	350	1750	Advance	350	232	83	62
13	2	50	1000	Advance	387	250	10	10
14	1	125	2125	Retreat	380	264	40	21
15	1	50	1750	Retreat	409	274	17	14
16	2	350	1000	Retreat	354	263	125	50
17	2	50	2500	Retreat	408	284	24	14
18	1	125	1375	Retreat	380	250	47	27

This phenomenon is more evident in FSW of dissimilar materials due to different mechanical and physical properties. As listed in table 4 and also thermal profile of the joints 1, 2 and 11, at a constant spindle rate, much higher peak temperature is obtained at 50 mm/min feed rate compared to that of 350 mm/min feed rate, which led that the heat generated during FSW is inversely proportional to the feed rate. Moreover, considering all the experiments, insignificancy of spindle rate to the peak temperature is found as well as proportional relation between feed rate and heating gradient. Approximately at all the experiments, slightly higher peak temperature in AA6061-T6

is obtained which can be interpreted as higher intensity of material transportation on the advancing side.

4.3 Macrostructural Evolution and Flow of Materials

Figure 10 shows OM images of the cross sections of the WC FSW joints. The AA6061-T6 is discernible by the darker color, while AA7075-T6 has a light color due to their different etching responses to the Keller's reagent.

Moreover, three microstructural zones, NZ, TMAZ and HAZ are discernible. It seems that the shape of the NZs verifies with process parameters. Rectangular shapes of NZ formed at higher traverse speed while at lower traverse speed elliptical shapes tend to form onion rings in NZs of the joints 1, 7, 8 and also 13 to 18. With increase in rotational speed from 1000 to 1750 rpm (Figures 10(J3, J5, J7, J8, J13, J16 & J18)), the size of the onion rings increased and opened up and shifted to the upper part. Further increase in rotational speed from 1750 to 2500 rpm, the onion ring structure disappeared (Figures 10(J4, J6, J10, J12, J14 & J15)). For high rotational speed, decrease in rotational speed eliminated the nugget boundary at the retreating side (Figures 10(J1, J2, J9, J11 & J17)).

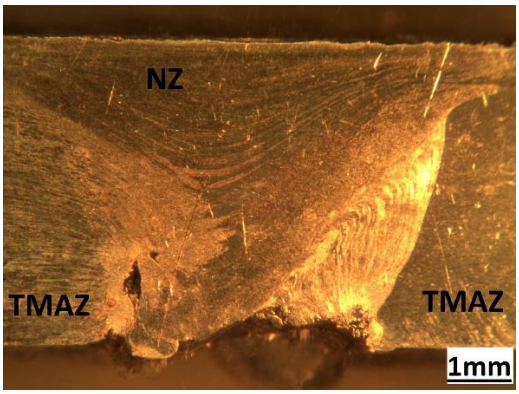

Joint 1

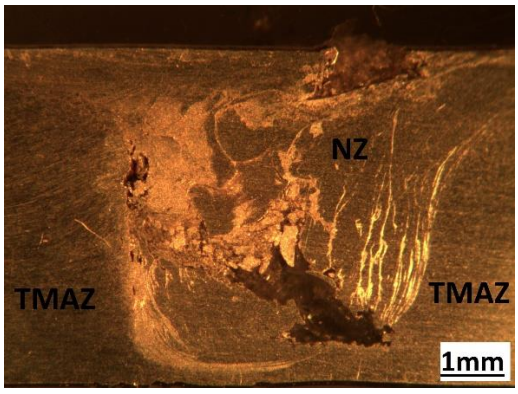

Joint2

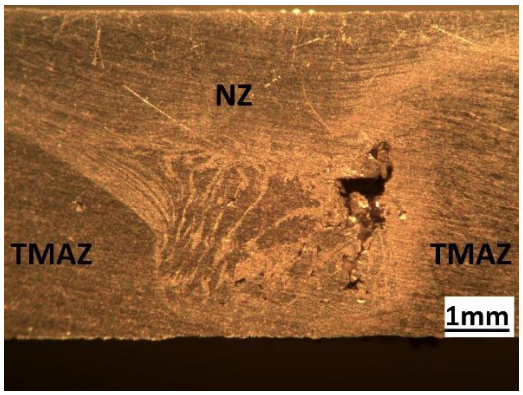

Joint3

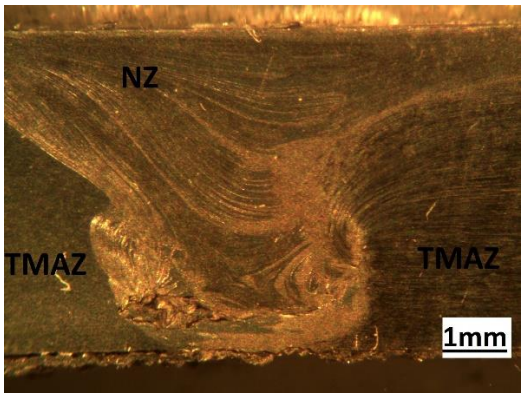

Joint4

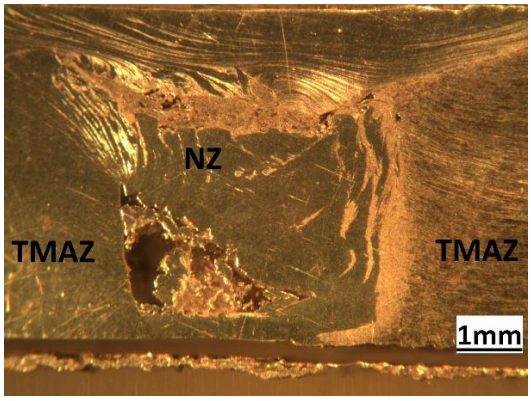

Joint5

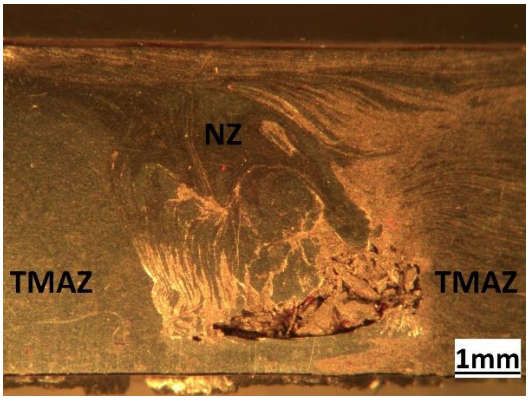

Joint6

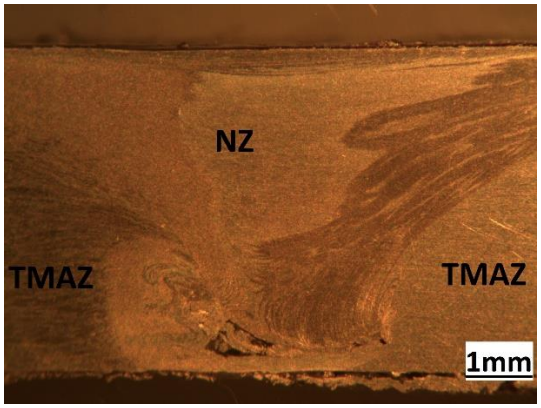

Joint7

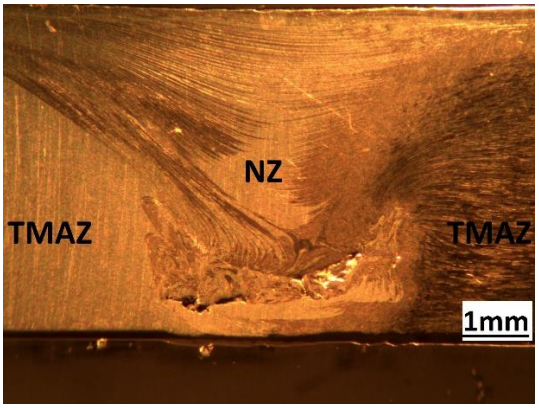

Joint8

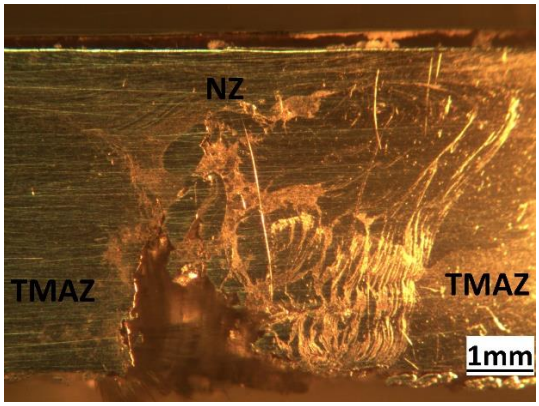

Joint9

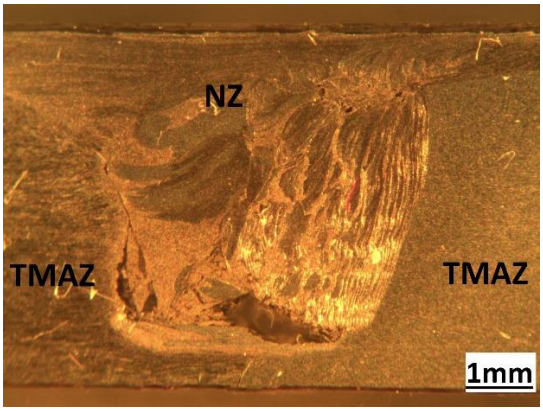

Joint10

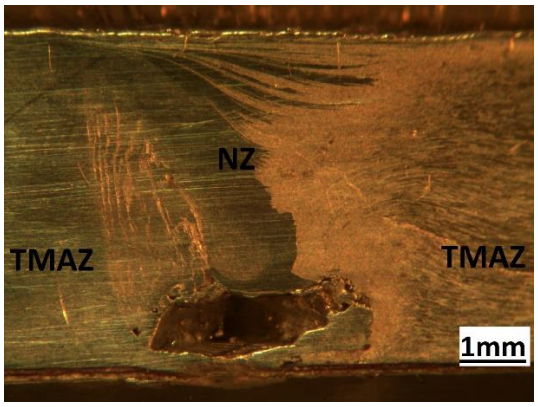

Joint11

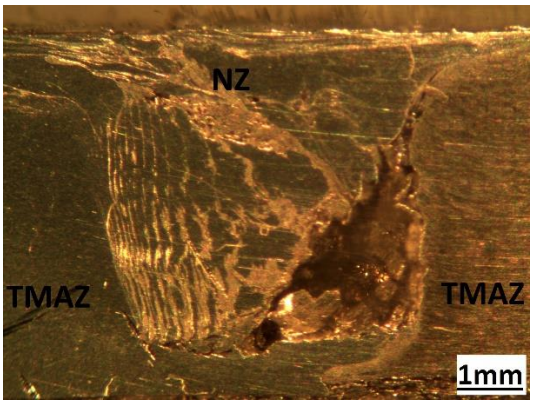

Joint12

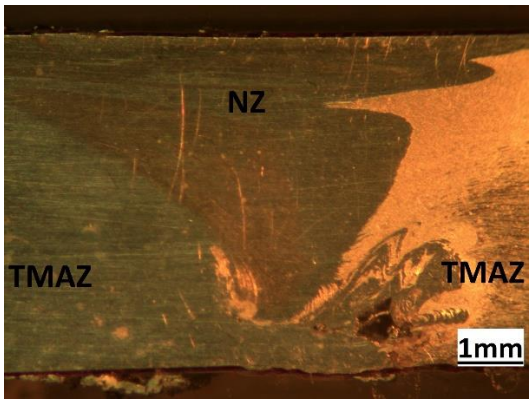

Joint13

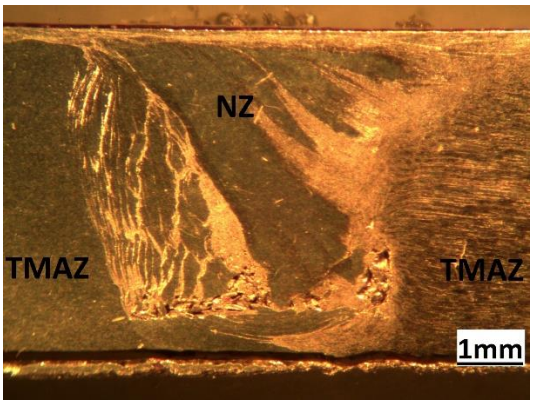

Joint14

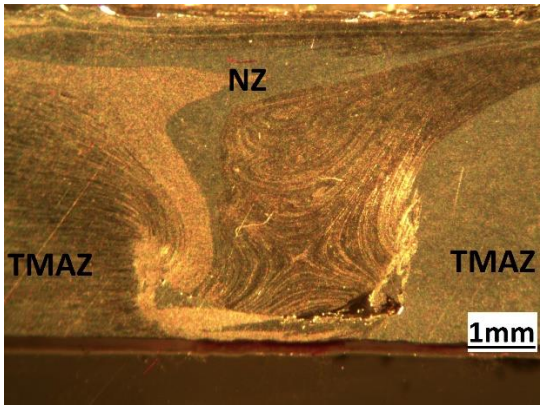

Joint15

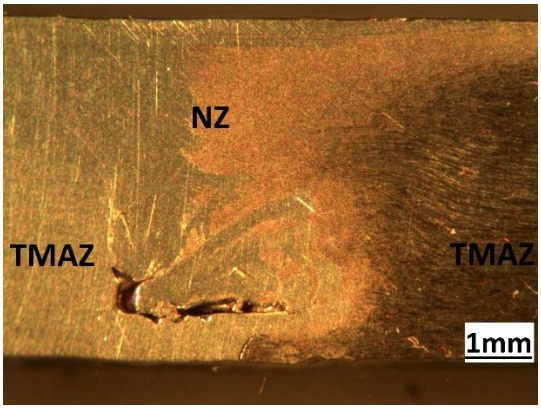

Joint16

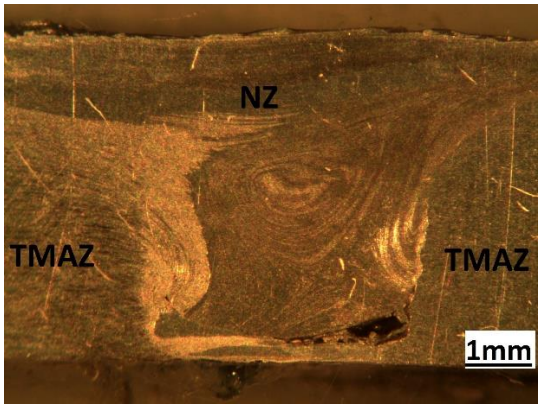

Joint17

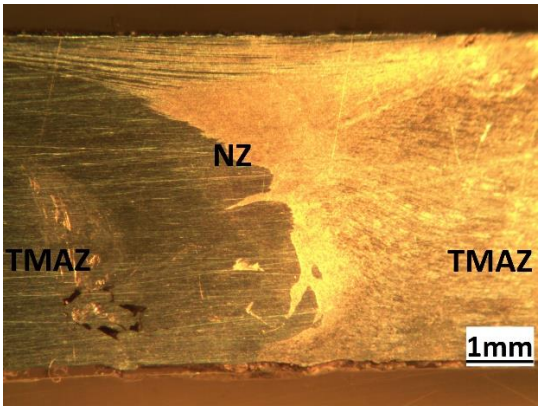

Joint18

Figure 10: OM of Joints' Cross Section (AA6061-T6 on left & AA7075-T6 on right)

Since the main aim of this study was covering wide range of parameters, some of the experiments were expected not to be very successfully joined. As a matter of the fact, this inconsistency in results will help later to establish optimum WC FSW parameters. In those joints with onion rings, variety of vortex centers can be observed which are more or less positioned vertically at the NZ. The compilation of vortexes feature observed in these samples, are quite unique in WC FSW in comparison to onion ring layers reported in AC FSW Compilation of such multiple vortexes has never been reported before. It seems, the threads pitch of the pin causes the formation mechanism of onion rings. At the cross section of the dissimilar welds of AA6061-T6 andAA7075-T6, onion rings with maximum three layers can be distinguishably observed (for example figure 10-J17). These sublayers are to be; i) 6061 alloy sub-layer (spectrum 1), ii) AA7075 alloy sub-layer (spectrum 2) and iii) mixed sub-layer of the two alloys (spectrum 3). The formations of AA6061 and AA7075 alloy sublayers are quite straight forward; while the formation of the mixed sub-layer could be attributed to that the plasticized materials contained in the spaces adjacent to the flats may have experienced intense extrusion turbulences and have enough time to be well mixed before finally deposited to the wake of the weld.

From flow of materials points of view, to get better results AA6061-T6 was located in the advancing side which is proven that the material turbulence is much more effective, especially at higher feed rates [7]. This is due to the higher flow stress of harder alloy, AA7075-T6, when positioned on the advancing side. This configuration makes the NZ impenetrable or hardly penetrable for softer alloy, AA6061-T6. In FSW, transportation of the materials on advancing side are much more intense around the tool before deposited in the wake of the weld then what are on retreating side [26]. Park et al subjected FSW of dissimilar AA5051-H32 and AA6061-T6 and concluded that the

mixture of materials were much more appropriate when the AA5052-H32 was located in the advancing side compared to the case of the AA6061-T6 in the advancing side [26].

4.4 Microstructural Inspection

4.4.1 TEM Inspection

Figure 11 depicts the TEM of the WC FSW joints near fractured area which accorded in retreating side.

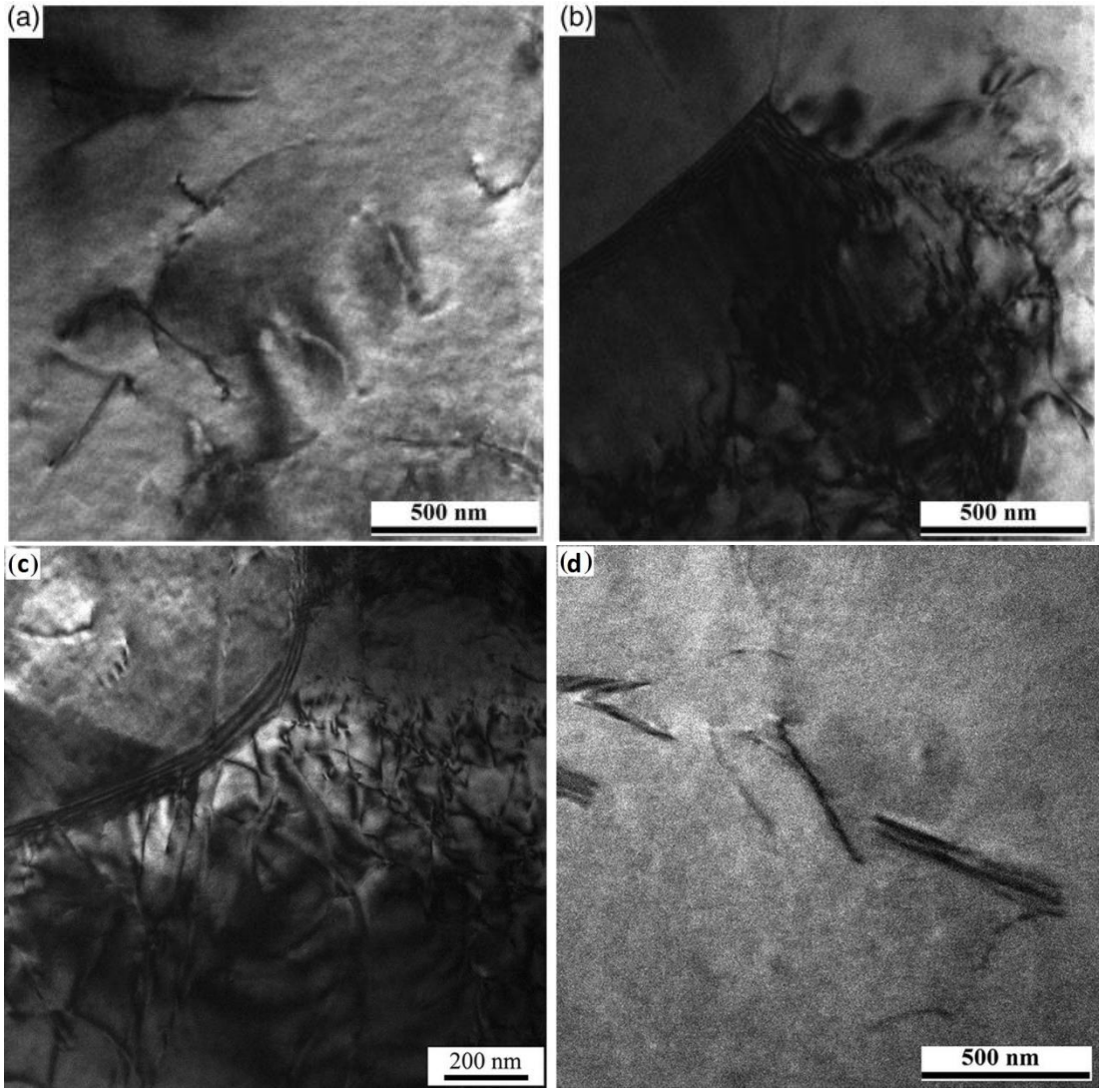

Figure 11: TEM images of the NZs of WC FSW at different thermal conditions

Images are provided from four samples which were exposed to four different thermal condition during WC FSW. These images reveal the effect of different thermal condition on density of dislocations which are known as obstacles to the growth of cracks thus delays the fracture. In other words the higher density of dislocation led to the higher UTS. Image 11-a, taken from joint 3 which was exposed to high peak temperature at high heating rate, depicts low density of dislocations while image 11-d, taken from joint 1 which was exposed to high peak temperature at low heating rate, depicts relatively lower density of dislocation. This comparison reveals significance of high peak temperature on lowering dislocation density and insignificance of heating rate. Image 11-b, taken from joint 13 which was exposed to low peak temperature at high heating rate, depicts high density of dislocation while image 11-c, taken from joint 16 which was exposed to high peak temperature at low heating rate, depicts relatively higher density of dislocation. This comparison reveals significance of lower peak temperature on maintain of dislocation density and insignificance of heating rate.

4.4.2 Evaluation of Grain Size

Figure 12 depicts the microstructure of the base metals (BMs) and NZs of the WC FSW joints. Images are provided from four samples which were exposed to four different thermal condition during the welding process. These images reveal the effect of different thermal condition on D_{av} which are known to be significant in strength of material by affecting the amount of grain boundary. In other words decrease in D_{av} increases the UTS of the joint. Image 12-a was taken from AA6061-T6 and image 12-b from AA7075-T6. Image 12-d, taken from NZ of joint 3 which was exposed to high peak temperature at high heating rate, depicts moderately large D_{av} while image 12-f, taken from NZ of joint 1 which was exposed to high peak temperature at low heating rate, depicts the largest D_{av}. This comparison reveals significance of both high peak

temperature and high heating rate on grain growth of NZs. Image 12-c, taken from NZ of joint 13, which was exposed to low peak temperature at high heating rate, depicts small D_{av} while image 12-e, taken from NZ of joint 16, which was exposed to high peak temperature at low heating rate, depicts relatively smaller D_{av}. This comparison reveals significance of lower peak temperature on generation of fine grains and insignificance of heating rate.

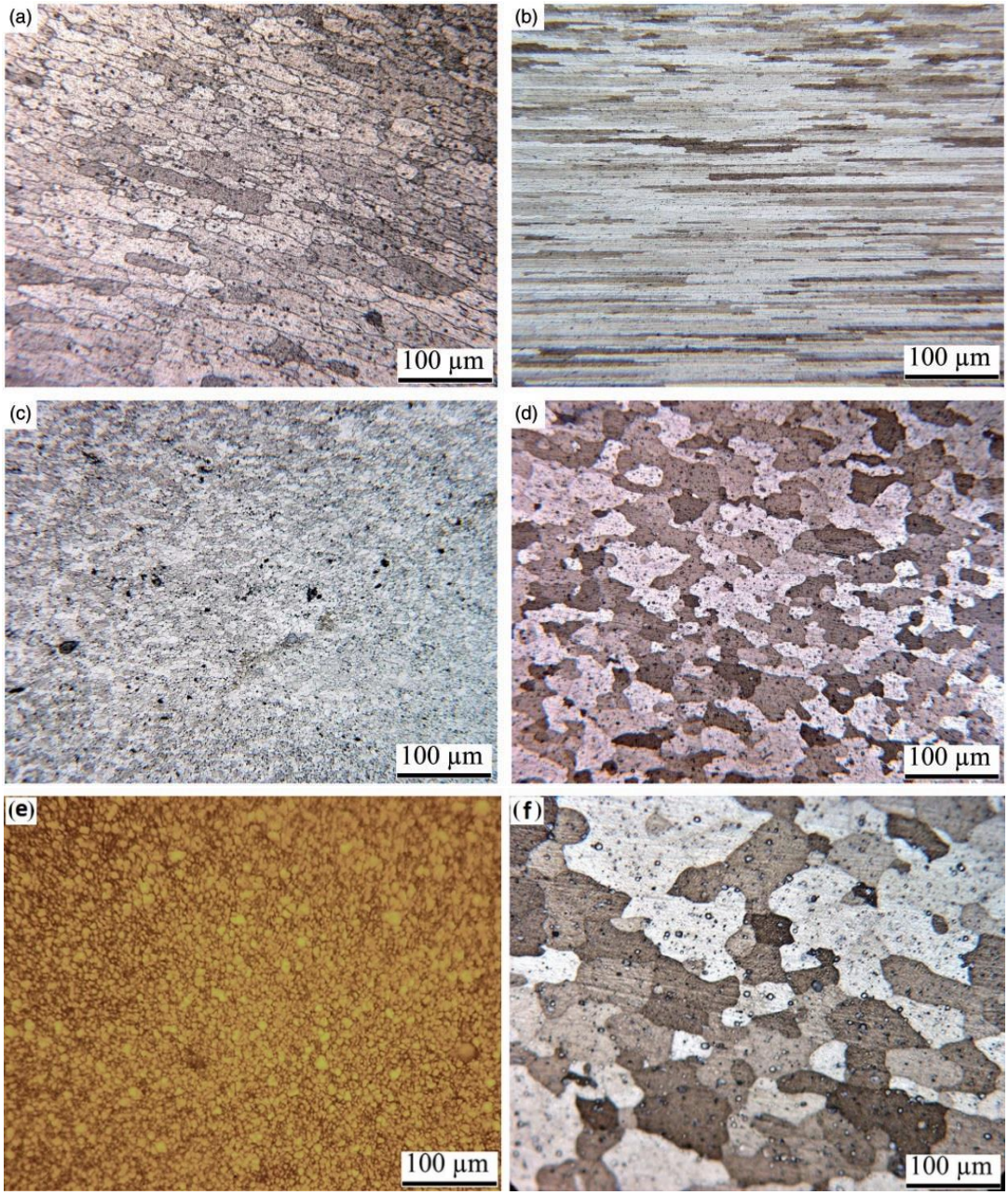

Figure 12: Microstructures of the BMs and NZs of the joints welded with different welding parameters

4.4.3 Fractographical Observations

Figures 13 depicts the SEM fractography of the fractured tensile samples. These images reveal the effect of different thermal conditions on formation a propagation of dimples and micro-voids which are known as the fracture mechanisms. Figure 13-a, taken from tensile sample of the joint 8, which was exposed to high peak temperature, contains fewer and larger dimples compared to figure 13-b, taken from tensile sample of the joint 9, which was exposed to low peak temperature.

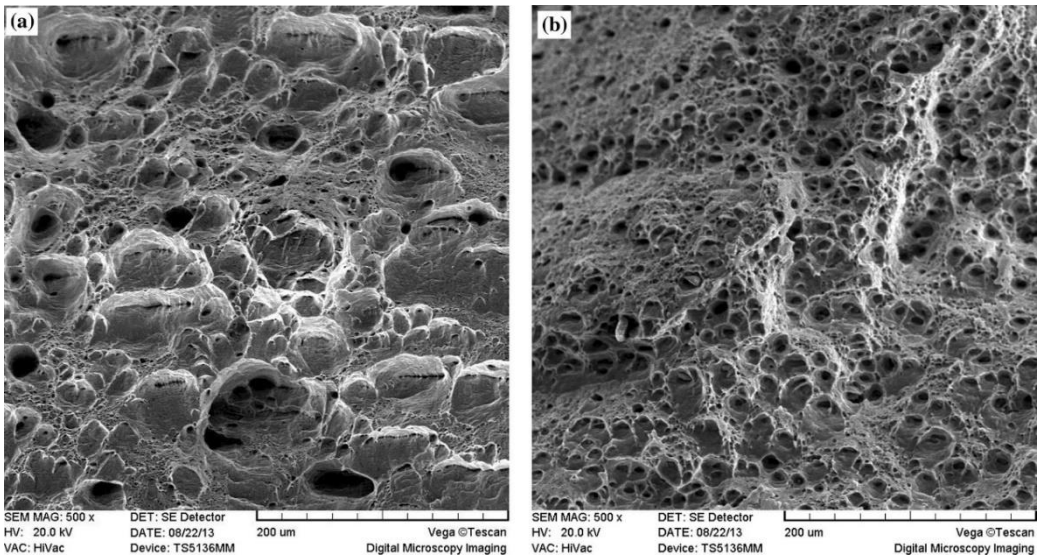

Figure 13: Fracture surface of the joints: (a) joint 8 and (b) joint 9

4.5 Macrohardness Results

In order to analyze the hardness evolution of the joined materials, 26 evenly distributed index points were subjected to macrohardness test. The distribution was managed to be in two classes. First class; upper and lower level of the cross section and second class; advance and retreat side of the joint. This evenly distributed index of hardness provides a comprehensive overview of macrohardness evolution of each joint. The wide of distribution was managed to cover 12mm on either sides of the joint. Hence, regions of NZ, TMAZ, HAZ and the base materials are studied for each joint as demonstrated in appendix B (run 1 to 18). Table 7 extracted from macrohardness

graphs and lists the lowest macrohardness of each joint align with the side and the located zone.

Table 7: Collection of Macrohardness Results

Joint	Rep	Traverse speed (mm/min)	Rotational Speed (rpm)	Lowest Hardness Side-mm away from center	Lowest Hardness Zone	Lowest Hardness (Vickers)
1	2	50	2500	Advance-6	TMAZ	70
2	2	350	2500	Advance-6	TMAZ	83.8
3	1	275	1375	Advance-8	HAZ	77.3
4	2	200	1750	Advance-6	TMAZ	76.6
5	1	200	1000	Advance-10	HAZ	70.3
6	1	275	2125	Advance-6	TMAZ	80.4
7	2	50	1000	Advance-6	TMAZ	60.3
8	2	350	1000	Advance-2	NZ	63.1
9	2	350	2500	Advance-10	HAZ	71.8
10	2	200	1750	Advance-0	NZ	71.8
11	1	200	2500	Advance-6	TMAZ	74
12	1	350	1750	Advance-10	HAZ	79.3
13	2	50	1000	Advance-4	TMAZ	54.5
14	1	125	2125	Advance-6	TMAZ	64.7
15	1	50	1750	Advance-4	TMAZ	64.9
16	2	350	1000	Advance-2	NZ	76.8
17	2	50	2500	Advance-6	TMAZ	61.9
18	1	125	1375	Advance-8	HAZ	71.4

Considering the location of LHZs, it shifts outward by increase in rotational speed and decrease in traverse speed. It is concluded that the location of LHZ is correlated with heat input, the more heat the more outward shifted LHZ which is in a good agreement with other articles [24].

Considering 5mm pin diameter and 15mm shoulder diameter, borders of NZ and TMAZ regions lay 2.5 and 7.5mm away from the center (joining line) respectively. As concluding from the macrohardness results, LHZ of just five joints is located in HAZ, this number is three for NZ and for the rest joints LHZ is located in TMAZ. Note that, all the LHZs located in TMAZ occurred 6mm away from the centerline which is so close to HAZ.

4.6 Tensile Strength Results

Table 8 shows the tensile properties of all the joints as well as the parent alloys. Values listed in table 8 are extracted from stress-strain curve of FSW joints demonstrated in appendix C (joint 1 to 18).

Those failures which occurred in HAZ indicate that seamless bonding has been achieved between parent alloys under that particular welding parameter and showed very good tensile property. In contrary, failure at center indicates week bonding between parent alloys.

Table 8: Collection of Tensile Strength Results

Joint	Rep	Feed Rate (mm/min)	Spindle Rate (rpm)	Tensile			Elongation (%El)
				Fracture Position	UTS (MPa)	Comparison with 6061	
1	2	50	2500	Advance, TMAZ	220.3	72.9%	3.8
2	2	350	2500	---- Unsuccessful ----			
3	1	275	1375	Center, NZ	138.7	45.9%	1.5
4	2	200	1750	Center, NZ	160	53%	3.1
5	1	200	1000	Center, NZ	117.3	38.8%	2.7
6	1	275	2125	Center, NZ	128	42.4%	2.9
7	2	50	1000	Advance, TMAZ	214.7	71.1%	4.6
8	2	350	1000	Advance, HAZ	242.7	80.4%	4.4
9	2	350	2500	Center, NZ	44	14.6%	1.5
10	2	200	1750	Center, NZ	100	33.1%	2.4
11	1	200	2500	Center, NZ	66.7	22.1%	2
12	1	350	1750	Center, NZ	16	5.3%	0.8
13	2	50	1000	Advance, TMAZ	206	68.2%	4.3
14	1	125	2125	Advance, TMAZ	239	79.1%	3.4
15	1	50	1750	Advance, TMAZ	217.4	72%	2.9
16	2	350	1000	Advance, TMAZ	237.3	78.6%	3.4
17	2	50	2500	Advance, TMAZ	214.4	71%	3.8
18	1	125	1375	Advance, HAZ	234.7	77.7%	5
6061		----		Center	302	----	10.9
7075		----		Center	600	----	13.1

Analyzing the obtained data from the experiments shows that the optimum spindle rate for WC condition is 1000 rpm since all the joints welded under this rate exhibit best of tensile properties. Moreover, at the constant spindle of 1000 rpm, UTS increases with the increase of feed rate. This increase in UTS is mainly due to maintain of precipitations and dislocations of the base materials for those joints which encountered less heat input and more importantly less time (high heating and cooling rate) during WC FSW [2]. Thus, less severe precipitate coarsening in the HAZ took place [2]. As illustrated in appendix A and also accordingly reflected in table 3 the peak temperatures at TMAZ and HAZ for joints 5 correspondingly are 378 ^{o}C and 248 ^{o}C, for join 7 these values are 389 ^{o}C and 252 ^{o}C for joint 8 are 363 ^{o}C and 219 ^{o}C. While for the same joints, 5, 7 and 8, the corresponding heat gradients are 74 ^{o}C /s, 19 ^{o}C/s and 110 ^{o}C /s. The interesting finding is that the rate of heat input is much more significant than the peak temperature. It is obvious that feed rate plays a significant role not only in the peak temperature but more importantly in rate of heat input. Therefore, it is not the peak temperature governing the structure of the welded material. As a matter of the fact these are the heating and of course cooling rates governing the performance of WC FSW joint. This point of view is quite unique and has never been reported. Comparison of the macrohardness profiles and the tensile data indicates the tendency of UTS is in a good agreement with the tendency of LHZ, which demonstrates the precipitate evolution caused by WC FSW thermal cycle determines both the macrohardness distribution and tensile property of the joints.

Chapter 5

OPTIMIZATION

5.1 Introduction

Response surface methodology is used to optimize the performance of the process in order to obtain the maximum benefit from the FSW. The software of Design Expert was performed to carry out the design of the experiments and develop the mathematical models. The analysis of variance (ANOVA) was used to confirm the established equations. In order to produce the joints, WC FSW was performed at the different traverse and rotational speeds according to Table 2 and 3.

5.2 Assessment of DoE

The fraction of design space (FDS) graph is shown in Figure 14.

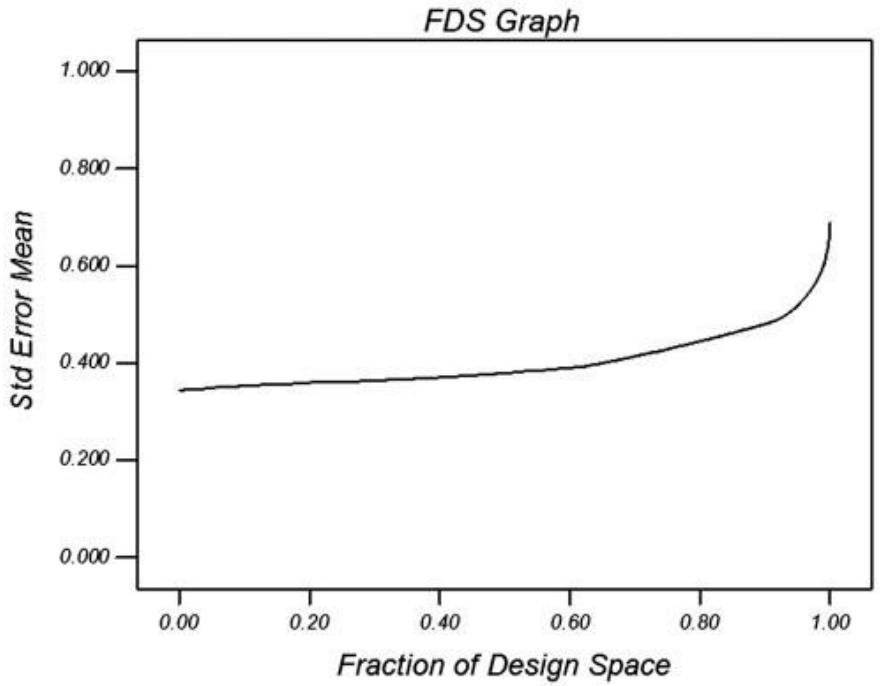

Figure 14: FDS graph of the developed design matrix

This type of diagram is a line graph illustrating the relationship between the volume of the design space (area of interest) and quantity of prediction error.

The plot reveals what percentage (fraction) of the design space includes a certain prediction error or lower. In common, a lower (approximately 1.0 or lower) and flatter FDS curve causes better results [32]. Furthermore, the Std Err (standard error) of design graph is illustrated in Figure 15. This type of diagram can be depicted as a contour (Figure 15-a) or 3D (Figure 15-b) plot revealing the standard error of prediction for regions in the design space.

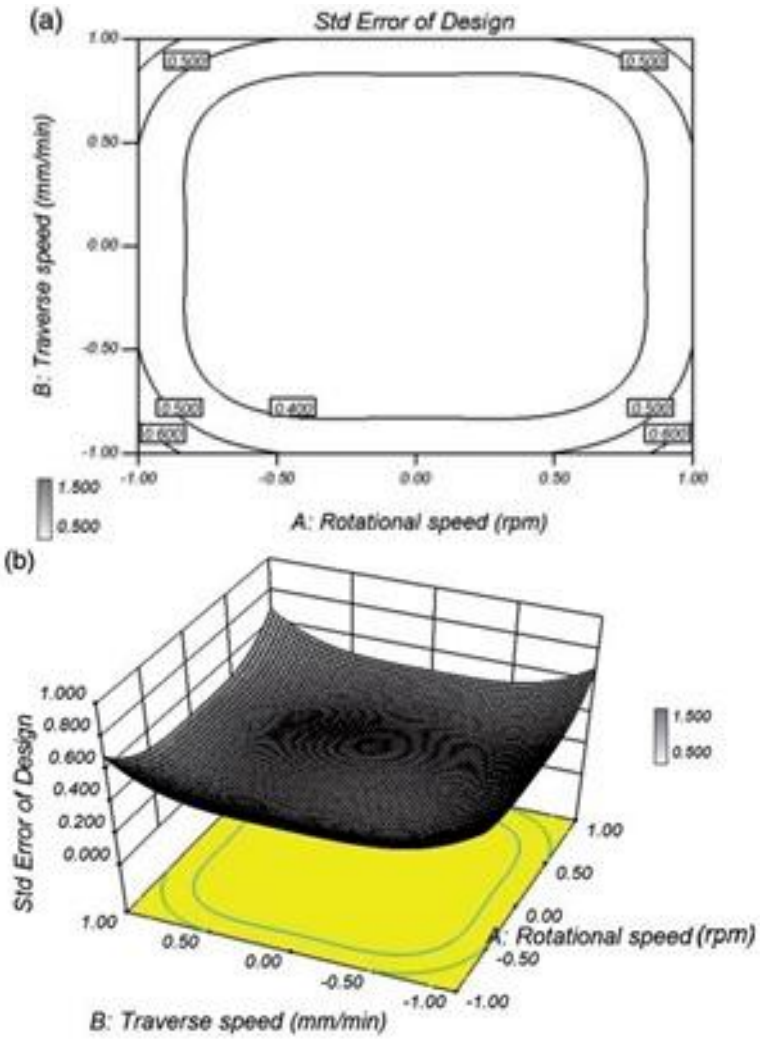

Figure 15: Std error of design graph: (a) contour plot and (b) 3D plot

By default, these amounts are calculated from the experimental design only, not of the responses. It means that the Std Err of design graphs are obtained before conducting the tests (of WC FSW), and they were calculated according the experimental design matrix. Normally, it will be superior this diagram to have somewhat lower standard error through the area of interest. Low is 1.0 or less [32].

5.3 Predicting Model

Table 9 confirms that the Design Expert software proposed the cubic models in the case of all responses.

Table 9: The results of different conducted models for hardness, D_{av}, UTS and El responses

	Source	P-value	R^2	Adjusted R^2	Condition
Hardness	Linear	<0.0001	0.9006	0.878	
	Quadratic	0.0003	0.9519	0.9197	
	Cubic	0.0001	0.9855	0.9739	Selected
	Quartic	0.6405	0.9838	0.9282	
	Fifth	0.4803	0.9838	0.8642	
D_{av}	Linear	<0.0001	0.9153	0.8997	
	Quadratic	<0.0001	0.9688	0.9612	
	Cubic	0.0453	0.9785	0.969	Selected
	Quartic	0.2722	0.9816	0.9523	
	Fifth	0.7205	0.9774	0.9304	
UTS	Linear	<0.0001	0.6734	0.589	
	Quadratic	0.1486	0.8366	0.7322	
	Cubic	0.011	0.909	0.7388	Selected
	Quartic	0.2295	0.9256	0.5336	
	Fifth	0.0836	0.9628	0.4238	
El	Linear	<0.0001	0.9272	0.9093	
	Quadratic	0.0009	0.9641	0.9401	
	Cubic	0.0006	0.9869	0.9794	Selected
	Quartic	0.6276	0.9855	0.9568	
	Fifth	0.5492	0.9845	0.8792	

Consequently, in this investigation, the relationships were established using a third-order polynomial regression model with the main and interaction effects of the input factors. More explanation of these type of models and the related mathematical equations are well discussed in the literature, which are developed using response surface methodology (RSM) [33, 34]. The statistical equations between the FSW factors and the responses have been reached as the following equations:

$$Hardness\ (H) = 95.57 - 17.95A + 16.16B + 1.56AB + 2.4A^2 - 8.17B^2 - 6.11A^2B + 6.46AB^2 - 0.53A^3 + 2.8B^3$$

Equation 1

$$D_{av}(\mu m) = 19.67 + 9.47A - 7.34B - 0.08AB - 2.46A^2 + 5.2B^2 + 1.94A^2B - 0.8AB^2 + 1.33A^3 - 4.13B^3$$

Equation 2

$$UTS\ (MPa) = 195.51 + 90.11A - 65.43B + 48.24AB - 23.66A^2 - 10.8B^2 + 21.26A^2B - 53.83AB^2 - 3.2A^3 + 10.4B^3$$

Equation 3

$$EL\ (\%) = 23.94 + 12.9A - 10.67B + 1.96AB - 2.58A^2 + 4.16B^2 + 1.99A^2B - 5.01AB^2 + 1.08A^3 - 1.61B^3$$

Equation 4

Equations (1) to (4) calculate and predict the value of H, D_{av}, UTS and El correspondingly. The predicted values and values extracted from experiments are listed in table 10 align with the corresponding levels of parameters.

Table 10: Design Layout Including Experimental and Predicted Values.

			Responses							
	Parameter Levels		Hardness (H)/Vickers		Average Grain Size (D_{av})/μm		UTS (MPa)		El (%)	
No.	A	B	Experimental	Predicted	Experimental	Predicted	Experimental	Predicted	Experimental	Predicted
1	-1	-1	91	90.1	22	21.9	231	210	29.4	28.8
2	-0.5	-1	74	76.9	30	30.7	226	234.9	37.5	36.1
3	0	-1	69	68.4	38	36.3	217	236.7	39.1	40.4
4	0.5	-1	67	64.2	39	39.8	208	222.1	41.4	42.4
5	1	-1	63	63.8	42	42	202	198.7	43.2	42.9
6	-1	-0.5	107	107.7	11	11.1	125	130.6	13.5	14.2
7	-0.5	-0.5	98	94.9	17	19.5	206	189.8	21.9	23.1
8	0	-0.5	83	85.1	28	25.2	262	243.2	33.3	30.5
9	0.5	-0.5	77	78.1	27	29.1	239	241.5	35.3	35.1
10	1	-0.5	72	73.4	33	32.4	223	239.3	39.4	38.7
11	-1	0	117	116	7	6.4	75	81.9	7.8	7.4
12	-0.5	0	105	105	16	14.2	130	138.9	17.8	16.7
13	0	0	95	95.6	19	19.7	213	195.5	23.4	23.9
14	0.5	0	88	87.4	24	24	239	234.3	30.4	29.9
15	1	0	82	79.9	28	28	247	258.8	34.3	35.4
16	-1	0.5	115	116.9	5	4.7	66	60.8	5.2	4.7
17	-0.5	0.5	110	109.4	10	11.6	103	108.2	11.9	12.6
18	0	0.5	103	102	17	16.8	154	161.4	19.6	19.5
19	0.5	0.5	92	94.2	20	21.2	218	208.1	24.6	25.5
20	1	0.5	86	85.7	27	25.9	243	245.9	31.7	31.6
21	-1	1	113	112.6	3	3	48	46	3.9	4.1
22	-0.5	1	111	110.2	8	8.8	89	87.2	10.6	10.6
23	0	1	105	106.4	15	13.4	121	129.7	15.4	15.8
24	0.5	1	102	100.6	18	17.7	162	170.9	21.5	20.8
25	1	1	92	92.6	22	22.8	220	208.6	26.3	26.2

The normal plot of residuals and the predicted versus actual response plot are shown in Figures 16 to 19, for the responses H and D_{av}. The normal probability plot is a graphical method to recognize substantive departures from normality. This comprises identifying outliers, skewness, kurtosis, a need for transformations, and mixtures.

Normal probability plots are drawn of raw data, residuals from model fits, and estimated parameters. In a normal probability plot, the sorted data are plotted vs. values selected to make the resulting image look close to a straight line if the data are approximately normally distributed. Deviations from a straight line suggest departures from normality. Figures 16-a, 17-a, 18-a and 19-a exhibit that errors are spread normally since the residuals follow a straight line.

Predicted vs. actual response plots show the accuracy of the model's prediction. In this type of plots, if the data lay on a 45° line, it means that there is a strong correlation between the predicted and actual responses. Figures 16-b, 17-b 18-b and 19-b disclose that the predicted data are in good agreement with the actual ones for the reason that the data points are fragmented uniformly by the 45° line.

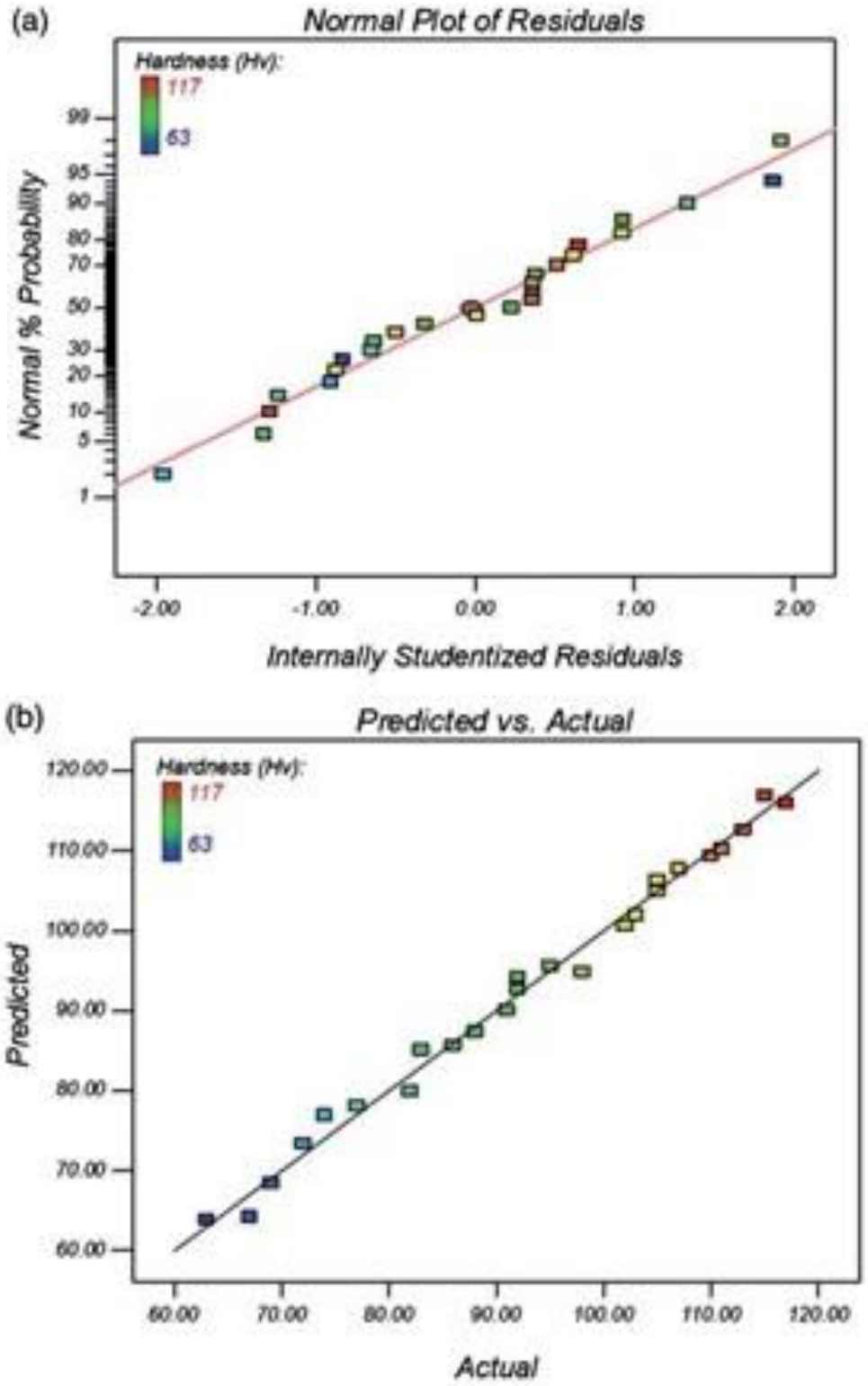

Figure 16: (a) Normal plots of residuals and (b) Actual response plot Vs. Predicted response for hardness

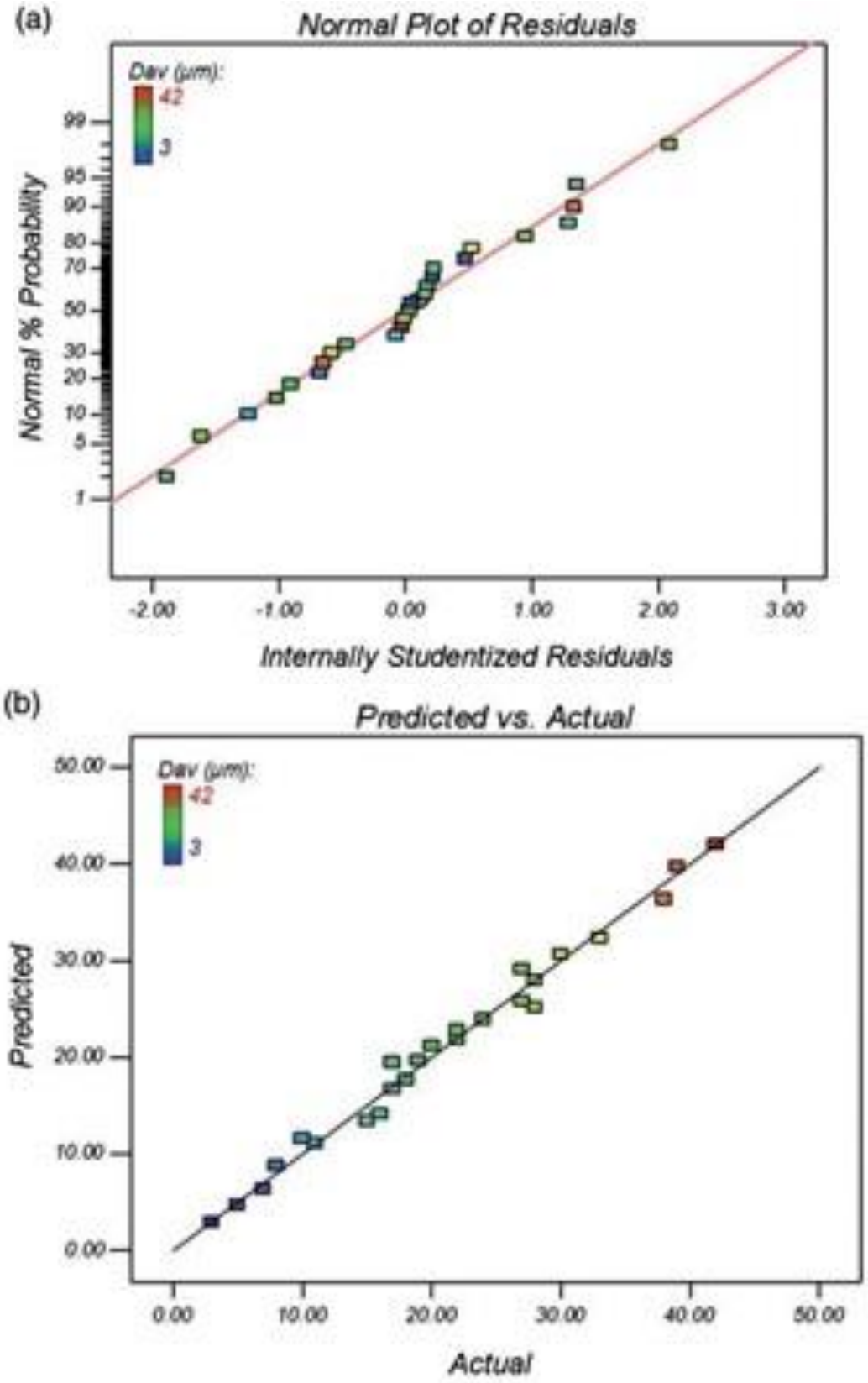

Figure 17: (a) Normal plots of residuals and (b) Actual response plot Vs. Predicted response for D_{av}

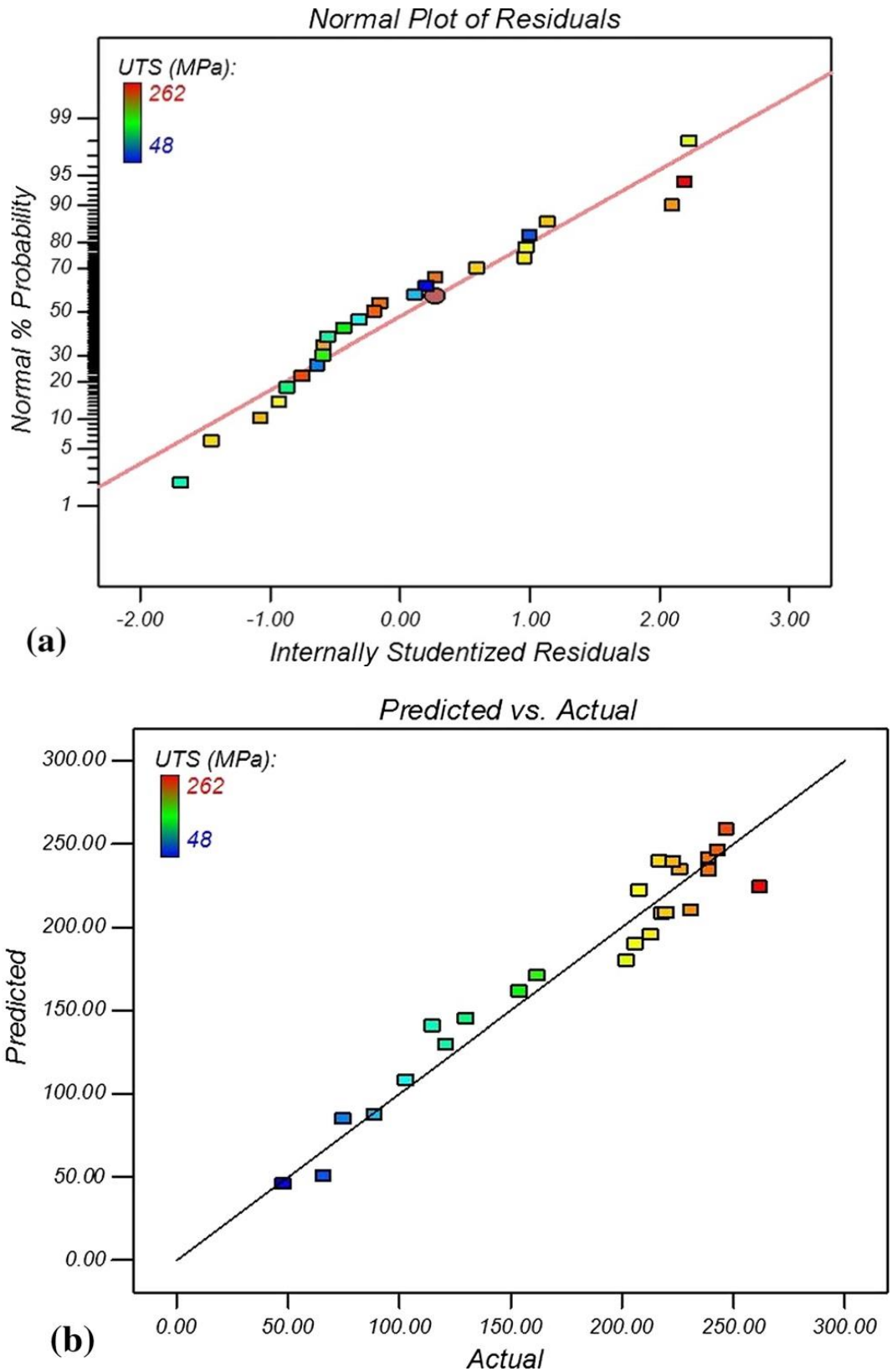

Figure 18: Normal plots of residuals and (b) Actual response plot Vs. Predicted response for UTS

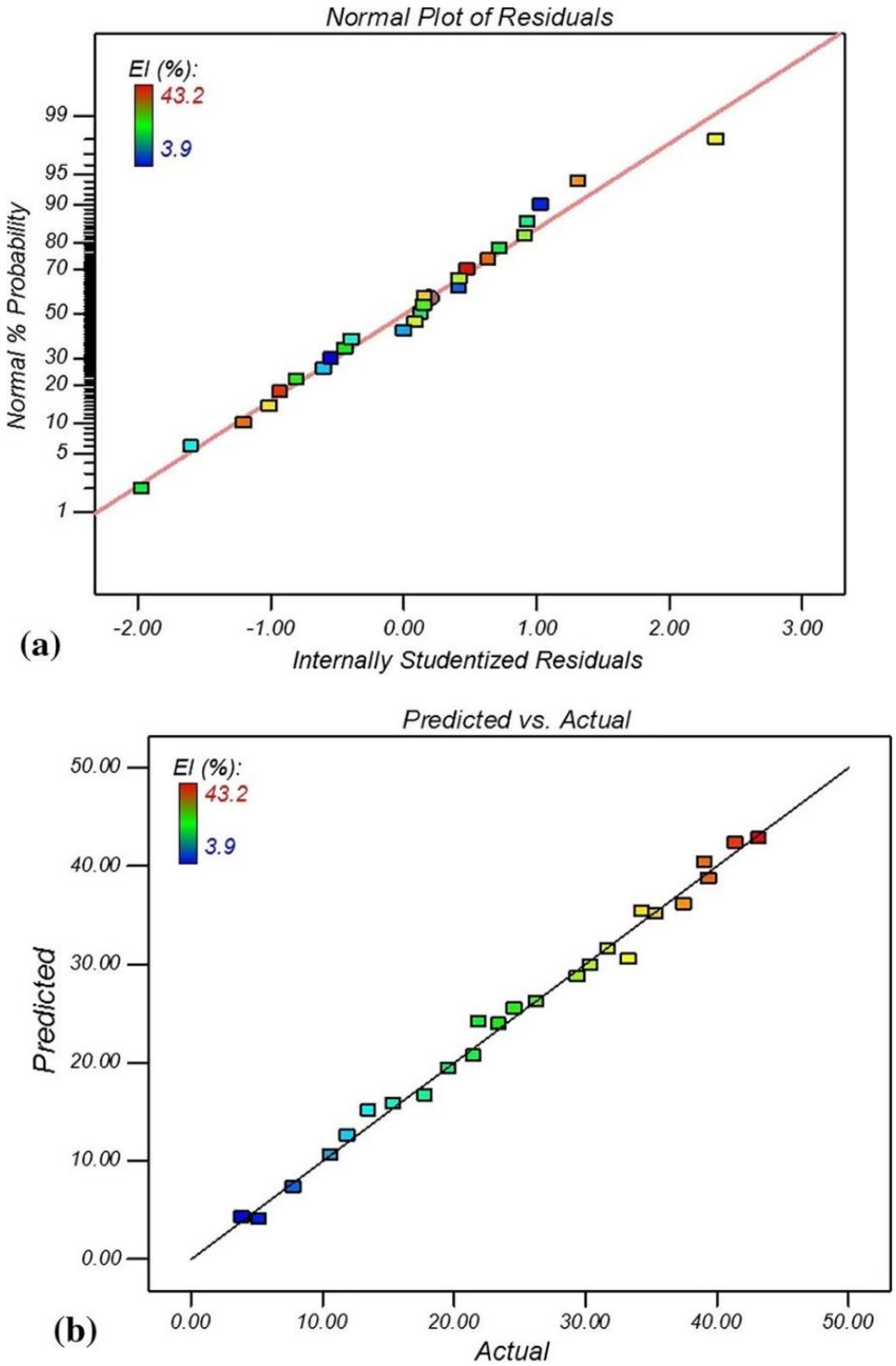

Figure 19: Normal plots of residuals and (b) Actual response plot Vs. Predicted response for El%

The ANOVA outcomes of the responses are summarized in Tables 11 to 14. The F-value, P-value, R^2 and adjusted R^2 are employed for indicating the more significant model and coefficients. Higher F-value, R^2 and adjusted R^2, and lesser P-value show that the model or a coefficient is significant.

Table 11: ANOVA table for the response Hardness (H)

Source	Sum of squares	Degree of freedom	Mean Square	F-value	P-value	
Model	6218.52	9	690.95	182.1	<0.0001	significant
A	365.91	1	365.91	96.43	<0.0001	
B	312.08	1	312.08	82.25	<0.0001	
AB	15.21	1	15.21	4.01	0.0637	
A^2	25.2	1	25.2	6.64	0.021	
B^2	292.13	1	292.13	76.99	<0.0001	
A^2B	81.78	1	81.78	21.55	0.0003	
AB^2	91.21	1	91.21	24.04	0.0002	
A^3	0.32	1	0.32	0.084	0.7755	
B^3	8.82	1	8.82	2.32	0.1482	
Residual	56.92	15	3.79			
R^2	0.9909					
Adjusted R^2	0.9855					

Table 12: ANOVA table for the response D_{av}

Source	Sum of squares	Degree of freedom	Mean Square	F-value	P-value	
Model	2696.31	9	299.59	122.62	<0.0001	significant
A	107.13	1	107.13	43.85	<0.0001	
B	64.37	1	64.37	26.35	0.0001	
AB	0.04	1	0.04	0.016	0.8999	
A^2	26.41	1	26.41	10.81	0.005	
B^2	118.3	1	118.3	48.42	<0.0001	
A^2B	8.26	1	826	3.38	0.0859	
AB^2	1.4	1	1.4	0.57	0.4608	
A^3	2	1	2	0.82	0.3799	
B^3	19.22	1	19.22	0.87	0.0133	
Residual	36.65	15	2.44			
R^2	0.9866					
Adjusted R^2	0.9785					

Table 13: ANOVA table for the response UTS

Source	Sum of squares	Degree of freedom	Mean Square	F-value	P-value	
Model	97090.05	9	10787.78	27.65	<0.0001	significant
A	9707.72	1	9707.72	24.88	0.0002	
B	5117.58	1	5117.58	13.12	0.0025	
AB	14544.36	1	14544.36	37.27	<0.0001	
A^2	2448.51	1	2448.51	6.28	0.0243	
B^2	510.3	1	510.3	1.31	0.2707	
A^2B	988.46	1	988.46	2.53	0.1323	
AB^2	6338.31	1	6338.31	16.24	0.0011	
A^3	11.52	1	11.52	0.03	0.8659	
B^3	121.68	1	121.68	0.31	0.5848	
Residual	5852.99	15	390.2			
R^2	0.9431					
Adjusted R^2	0.9090					

Table 14: ANOVA table for the response El

Source	Sum of squares	Degree of freedom	Mean Square	F-value	P-value	
Model	3332	9	370.22	201.97	<0.0001	significant
A	200.04	1	200.04	109.13	<0.0001	
B	136.2	1	136.2	74.3	<0.0001	
AB	23.91	1	23.91	13.05	0.0026	
A^2	29.06	1	29.06	15.85	0.0012	
B^2	75.71	1	75.71	41.3	<0.0001	
A^2B	8.7	1	8.7	4.75	0.0457	
AB^2	54.94	1	54.94	29.97	<0.0001	
A^3	1.31	1	1.31	0.72	0.4108	
B^3	2.93	1	2.93	1.6	0.2256	
Residual	27.5	15	1.83			
R^2	0.9918					
Adjusted R^2	0.9869					

Considering the Tables 11 to 14, the F-value, P-value, R^2 and adjusted R^2 for the established equations of H, D_{av}, UTS and El are 182.1, <0.0001, 0.9909 and 0.9855, and 122.62, <0.0001, 0.9866 and 0.9785 and 27.65, <0.0001, 0.9431 and 0.9090 and 201.97, <0.0001, 0.9918 and 0.9869 correspondingly. Thus, it can be determined that the established equations predict very adequate and significant data. Furthermore, P<0.05 validate that the coefficients are significant and P>0.1 confirm that the coefficients are not significant. Hence, consistent with the P-values, A, B, A^2, B^2, A^2B and AB^2 are significant terms in the developed equation of H. Similarly, A, B, A^2 and B^2 are significant terms in the developed equation of D_{av} and A, B, AB, A^2 and AB^2 are significant terms in the developed equation of UTS and finally, A, B, AB, A2, B2, A2B and AB2 are significant terms in the developed equation of El.

Therefore, by eliminating the non-significant terms of the developed equations, the reduced models are reached as the following mathematical equations:

$$Hardness\ (H) = 95.57 - 17.95A + 16.16B + 2.4A^2 - 8.17B^2 - 6.11A^2B + 6.46AB^2$$

Equation 5

$$D_{av}(\mu m) = 19.67 + 9.47A - 7.34B - 2.46A^2 + 5.2B^2$$

Equation 6

$$UTS\ (MPa) = 195.51 + 90.11A - 65.43B + 48.24AB - 23.66A^2 - 53.83AB^2$$

Equation 7

$$EL\ (\%) = 23.94 + 12.9A - 10.67B + 1.96AB - 2.58A^2 + 4.16B^2 + 1.99A^2B - 5.01AB^2$$ Equation 8

Likewise, the F-values demonstrate that the orders of the most significant parameters in the model of H are A>B>B^2>AB^2>A^2B>A^2, in the model of D_{av} are B^2>A>B>A^2, in the model of UTS are AB>A>AB^2>B>A^2 and in the model of El are AB>A>AB^2>B>A^2.

5.4 Optimization

The contour, 3D and perturbation diagrams for the response D_{av} are shown in Figure 20.

From Figures 20, larger values of traverse speeds and smaller amounts of rotational speeds lead to finer D_{av} which is in a good agreement with the results obtained in microstructure inspection demonstrated in figure 12. According to the equiaxed grains and fine grain size in the NZ of the joints, FSW resulted in occurrence of dynamic recrystallization (DRX) during the process. FSW can be considered as a hot deformation procedure because of presence of heat and deformation. Thus, the D_{av} would be ruled by thermomechanical factors such as strain rate and temperature [35].

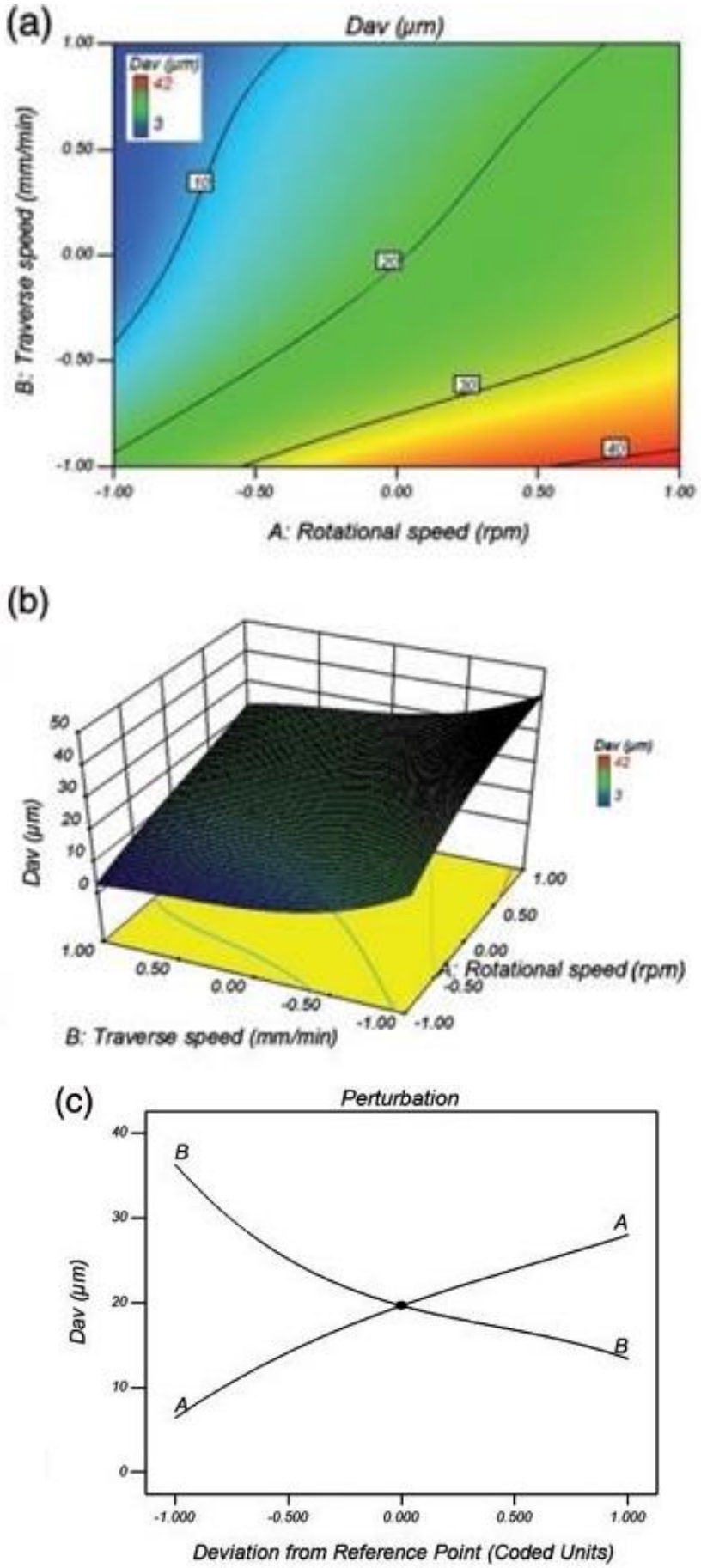

Figure 20: Counter, 3D and perturbation plots for the response D_{av}

In thermomechanical processes, the Zener–Hollomon parameter is commonly used for correlation between the temperature and strain rate as follow [36]:

$$Z = \dot{\varepsilon} \exp(\frac{Q}{RT}) \qquad \text{Equation 9}$$

where Z stands for Zener-Hollomon factor, $\dot{\varepsilon}$ belongs to strain rate, Q refers to activation energy, T is temperature and R represents the gas constant. The T and $\dot{\varepsilon}$ are estimated by means of subsequent relationships, respectively [37].

$$\dot{\varepsilon} = R_m . 2\pi r_e / L_e \qquad \text{Equation 10}$$

$$\frac{T}{T_m} = K^2 \left(\frac{\omega^2}{10^4 . v}\right)^a \qquad \text{Equation 11}$$

In equation (10), R_m, r_e, and L_e stand for half of tool rotational speed, the impressive radius, and depth of the dynamically recrystallized region, respectively.

In equation (11), k and α belong to constants between 0.04–0.06 and 0.65–0.75, ω refers to tool rotational speed, υ denotes tool traverse speed and T_m stands for the melting point of the alloy [36]. In addition, it has been proved that the D_{av} through thermomechanical procedures has a contrary relationship with Z. Thus, regarding equations (9) to (11), higher amount of $\dot{\varepsilon}$ leads to lesser D_{av} where larger T causes bigger D_{av}. Therefore, the $\dot{\varepsilon}$ and T are competing in specifying the final D_{av} after the thermomechanical procedures of the metals. From Figures 12 and 20, by increasing the rotational speeds (larger T and smaller $\dot{\varepsilon}$) and by decreasing the traverse speeds (larger T), the D_{av} grows. Therefore, in the current research, the main parameter which rules the final D_{av} of the NZs is T. For instance, the thermal history of the two joints

welded at low and high heat input conditions are illustrated in Figure 21, which shows that the peak temperature produced during FSW in high heat input condition is much higher than that of the low heat input one.

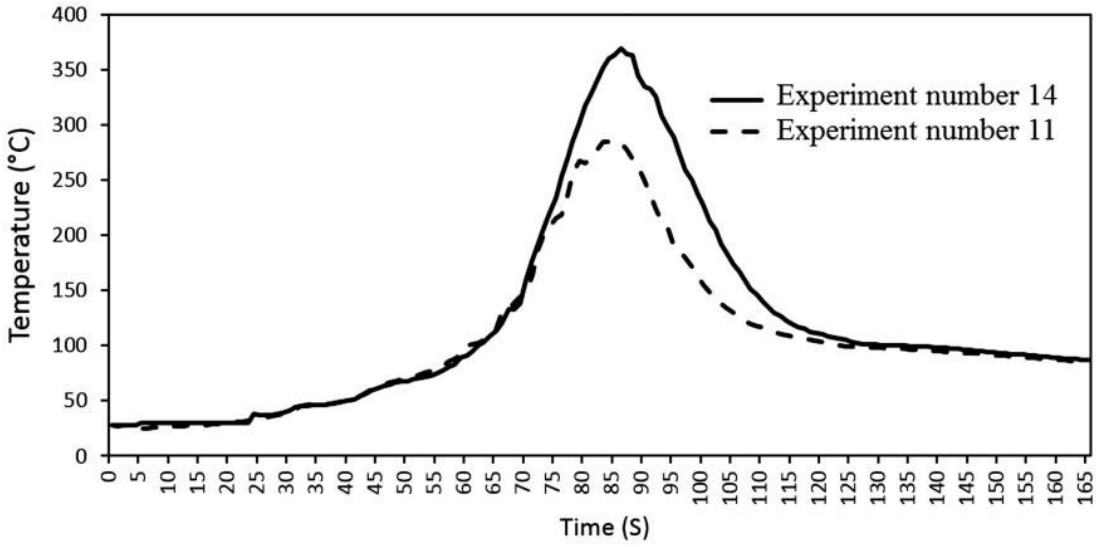

Figure 21: Thermal history of the joints welded at different thermal conditions: (a) lower heat input condition or experiment number 11, and (b) higher heat input condition or experiment number 14

The influences of FSW factors on the H of the joints are shown in Figure 22 by means of counter, 3D and perturbation plots.

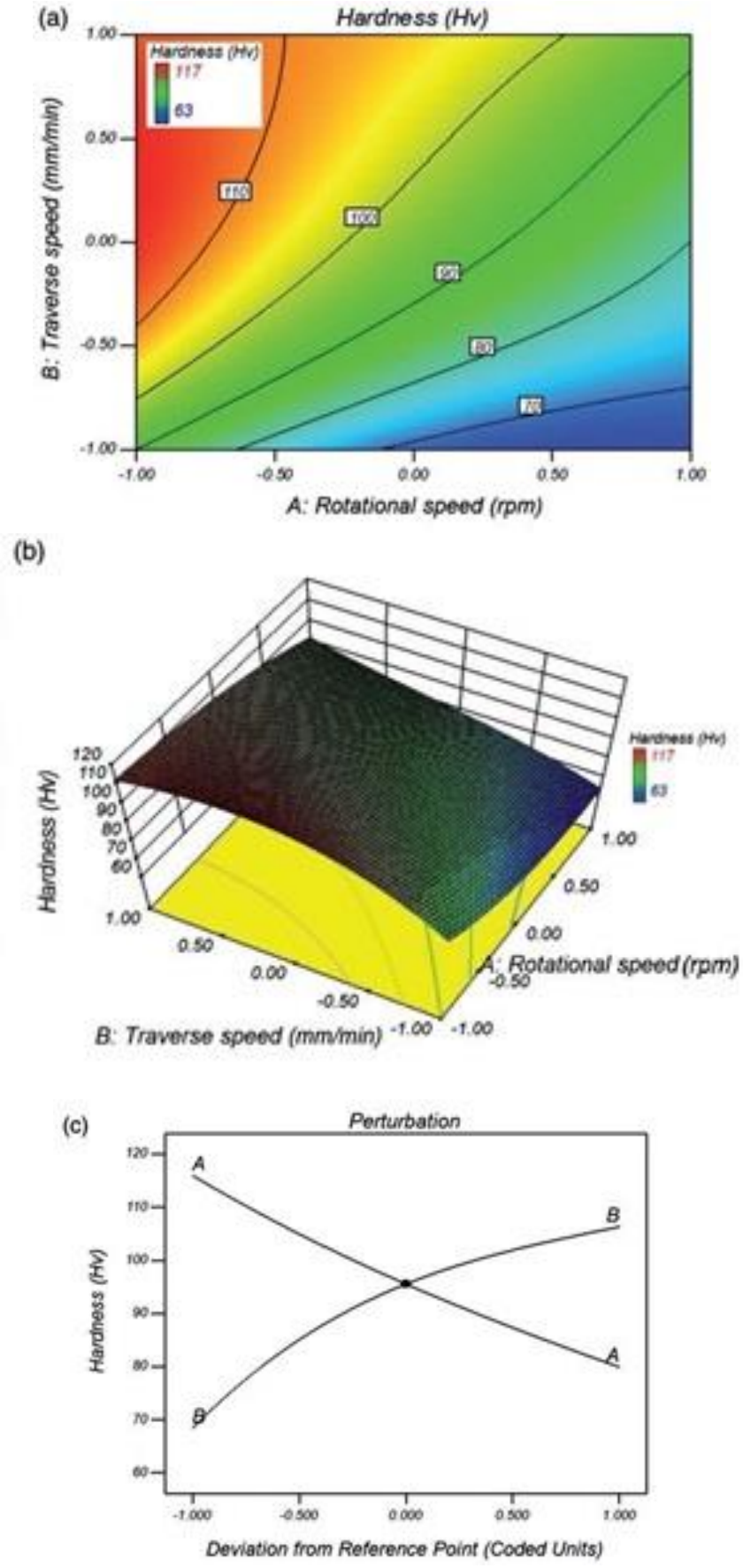

Figure 22: Counter, 3D and perturbation plots for the response H

From Figure 22, lesser the rotational speeds and higher the traverse speeds results in higher H amounts that can be because of finer D_{av} as discussed in the prior section (Figures 12 and 20). The strengthening mechanisms that lead to larger critical resolved shear stress (CRSS) in polycrystalline metals are the precipitation strengthening ($\Delta\tau_{ppt}$), the solution strengthening ($\Delta\tau_{ss}$), the dislocation strengthening ($\Delta\tau_D$), the grain boundary strengthening ($\Delta\sigma_{gb}$), the strengthening due to crystallographic texture, and the strengthening by reason of the second phase effect (in multi-phase alloys). Hence, the yield strength (σ_y) can be defined by the following equation [36]:

$$\sigma_y = \Delta\sigma_{gb} + M\tau_{tot} = \Delta\sigma_{gb} + M\left[\Delta\tau_0 + \quad \Delta\tau_{ss} + \quad \left(\Delta\tau_D^2 \quad \Delta\tau_{ppt}^2\right)^{1/2}\right]$$

Equation 12

where M stands for a crystallographic orientation parameter (commonly the Taylor factor), τ_{tot} refers to the CRSS (Critical resolved shear stress is the component of shear stress, resolved in the direction of slip, necessary to initiate slip in a grain.) and $\Delta\tau_0$ denotes the inherent strength of pure metal.

From equation (12), the strengthening mechanisms of $\Delta\sigma_{gb}$ and $\Delta\tau_D$ can be responsible for higher H at lower heat input conditions in this study $\Delta\sigma_{gb}$ in a recrystallized metal can be formulated as follows [33]:

$$\Delta\sigma_{gb} = \alpha_2 Gb\left[(1 - f_{Re})\left(\frac{1}{\delta}\right) + f_{Re}\left(\frac{1}{D}\right)\right] \qquad \text{Equation 13}$$

where α_2 stands for a constant, G refers to the shear modulus, b belongs to the Burgers vector, f_{Re} denotes the recrystallized volume fraction, σ represents the subgrain size of

the unrecrystallized part, and the D states the grain size of the recrystallized part. According to equation (9), D_{av} of the NZs (Table 10), and the microstructure of the NZs (Figure 12), the $\Delta\sigma_{gb}$ for the NZs of the joints welded at lower heat input conditions would have higher values compared to those of the welded at higher heat input conditions. Furthermore, the increase in CRSS owing to dislocations can be formulated as follows [38]:

$$\Delta\sigma_D = \alpha_1 Gb\sqrt{\rho} \qquad \text{Equation 14}$$

where α_1 refers to a constant and ρ stands for the dislocation density.

According to the TEM images of the NZs (Figure 11-a and 11-b), it is clear that the dislocation densities in the NZ of the joints welded at lower heat input conditions are higher than that of the joints welded at higher heat input conditions, hence higher values of $\Delta\sigma_D$. Moreover, the influence of texture on the strength has been stated in terms of the parameter M in equation (12). Mironov et al. [37, 39] have demonstrated that the FSW of alloys does not alter the texture parameters (i.e. Taylor or Schmitt factors). Thus, the M parameter is supposed to be almost constant in equation (12) for the NZs. As a result, it can be concluded that maintain of fine grain boundaries and amount of dislocations are the main mechanisms responsible for the higher hardness of the joints welded at lower heat input conditions.

This fact can be also clearly found from the tensile properties of the two joints welded at lower and higher heat input conditions (respectively, experiments number 8 and 9). The stress–strain curves of these joints are comprised in Figure 23.

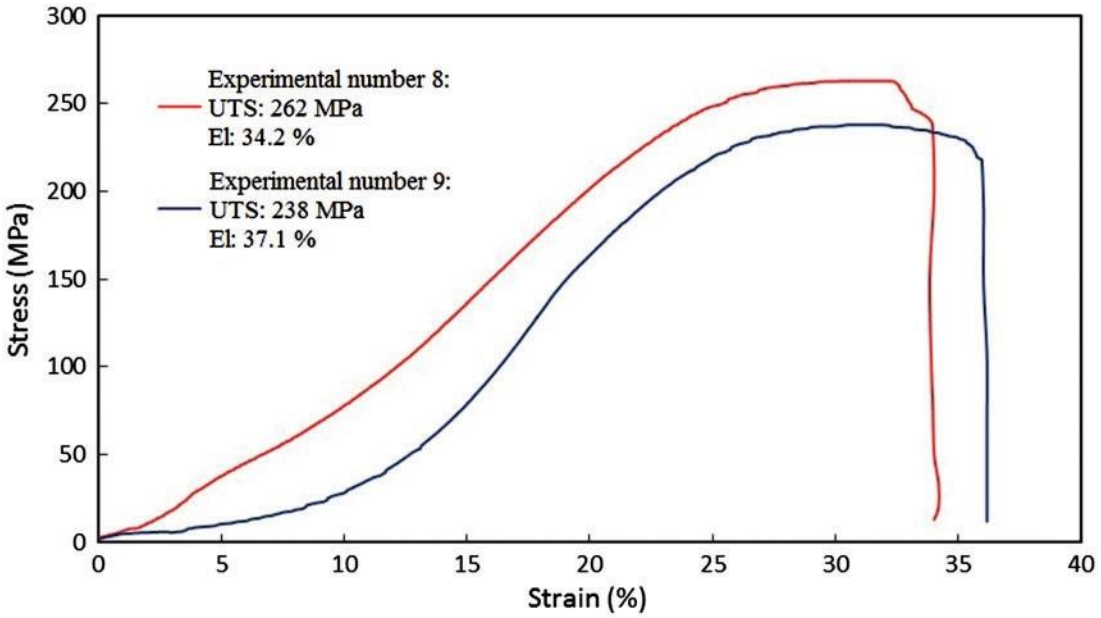

Figure 23: The stress–strain curves of the tensile samples welded at different thermal conditions

The sample welded at lower heat input condition (sample 8) has larger UTS of 262MPa compared to that of joint welded at higher heat input conditions (sample 9) i.e. 238 MPa, which is in good agreement with hardness results.

Along with the relationships between FSW factors and the joint properties, the dealings between microstructures and mechanical features play a key role. Hall–Petch (H–P) equation is the best way to define the correlation between microstructure and hardness. The H–P equation in the case of hardness could be stated as follows [40]:

$$H = H_0 + kd^{-1/2}$$ Equation 15

where H refers to the hardness, d stands for the average grain size, H_0 and k denote the appropriate constants associated with hardness amounts, correspondingly. In addition, k represents the H–P slope which designates the relative strengthening involvement of grain boundaries. It has been shown that the H–P relationship requires modification in

the case of severe plastic deformed metals because of the effect of substructures [41]. Therefore, after FSW, which causes a severe plastic deformation, the H–P relationship can be deviated from its linear equation as represented in equation (15). In the present investigation, for correlation between H and D_{av} of the NZs, the H–P equation were calculated according to the records in Table 8 as shown in Figure 24.

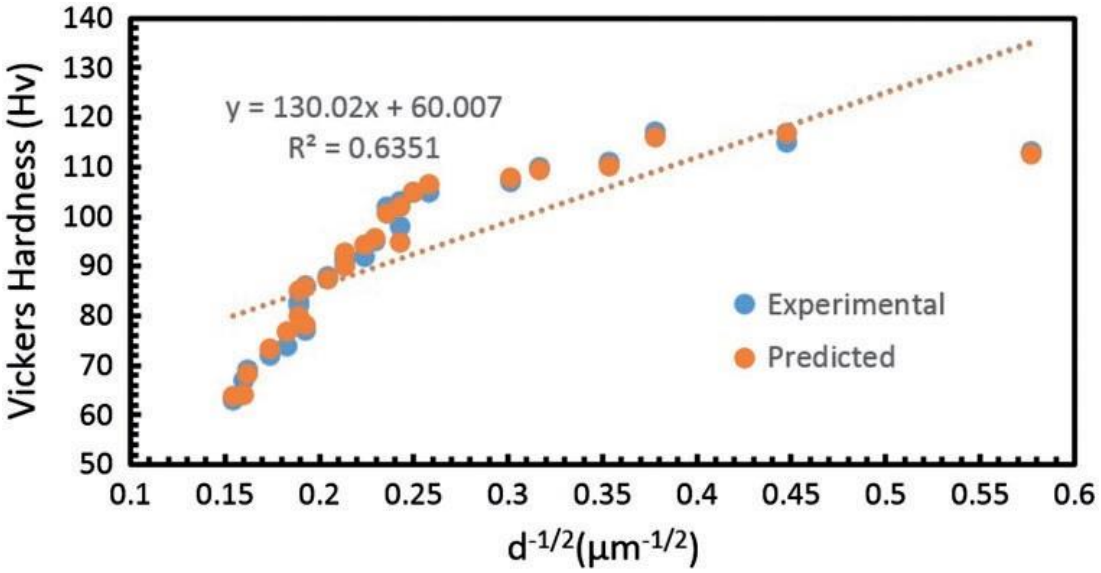

Figure 24: Plots for H–P relationship

The H–P equation for the NZs was achieved as follows:

$$H = 60.007 + 130.02d^{-1/2}$$ Equation 16

Regarding to the R^2 amount (=0.63), the H–P relation shows a deviation from its linear equation. As mentioned before, the reason of this phenomenon is that in the classical H–P equation, only the high angle grain boundaries are considered as impediments to the movement of dislocation [42]. Therefore, the presence of substructures, for instance precipitates, dissimilar structures of dislocation and the second phase particles could influence on the H–P equation [43, 45]. These microstructural properties inhibit

the movement of dislocations and stuck them in area lesser than the D_{av}, and after this decrease the influence of D_{av} on the hardness. The TEM images of the NZs (Figure 11) disclose that the inside of the grains have different densities of dislocations. Thus, the cause of the deviation from linear H–P equation is the presence of dissimilar densities of dislocations inside the NZ of the various joints.

The contour and 3D diagrams for the UTS are shown in Figure 25. These diagrams elucidate the interaction effect of any two factors on the UTS when the other factors are at their zero level (central level).

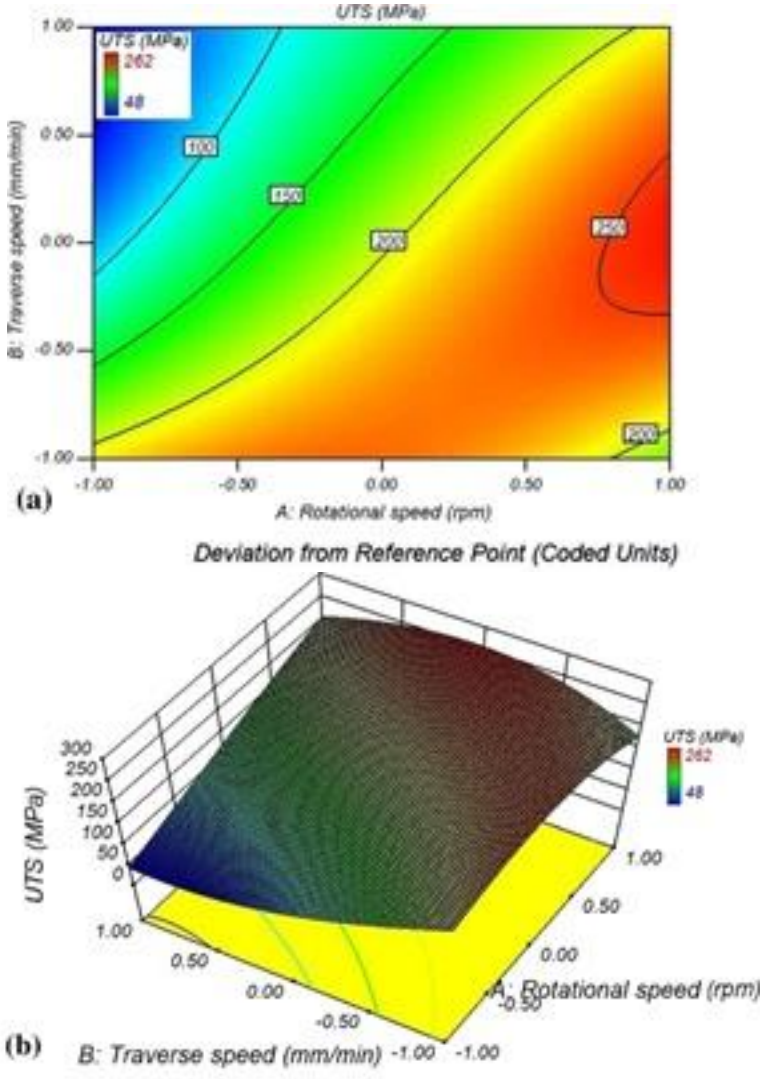

Figure 25: Counter and 3D surface plots for the response UTS

According to Figure 25, by increasing the rotational and traverse speeds, the UTS of the joints increases up to a maximum amount and then decreases. The lower rotational speeds and higher traverse speeds produce inadequate temperature and plastic deformation that result in weak plastic flow and defect formation, and hence cause lower UTS. For example, the macrostructures of the joints welded at high and low rotational speeds are shown in Figure. 26, which shows that defect-free joint has been produced in higher rotational speed (Figure26-a and d) where a void defect has been formed in the joint welded at lower rotational speed (Figure 26-b and c).

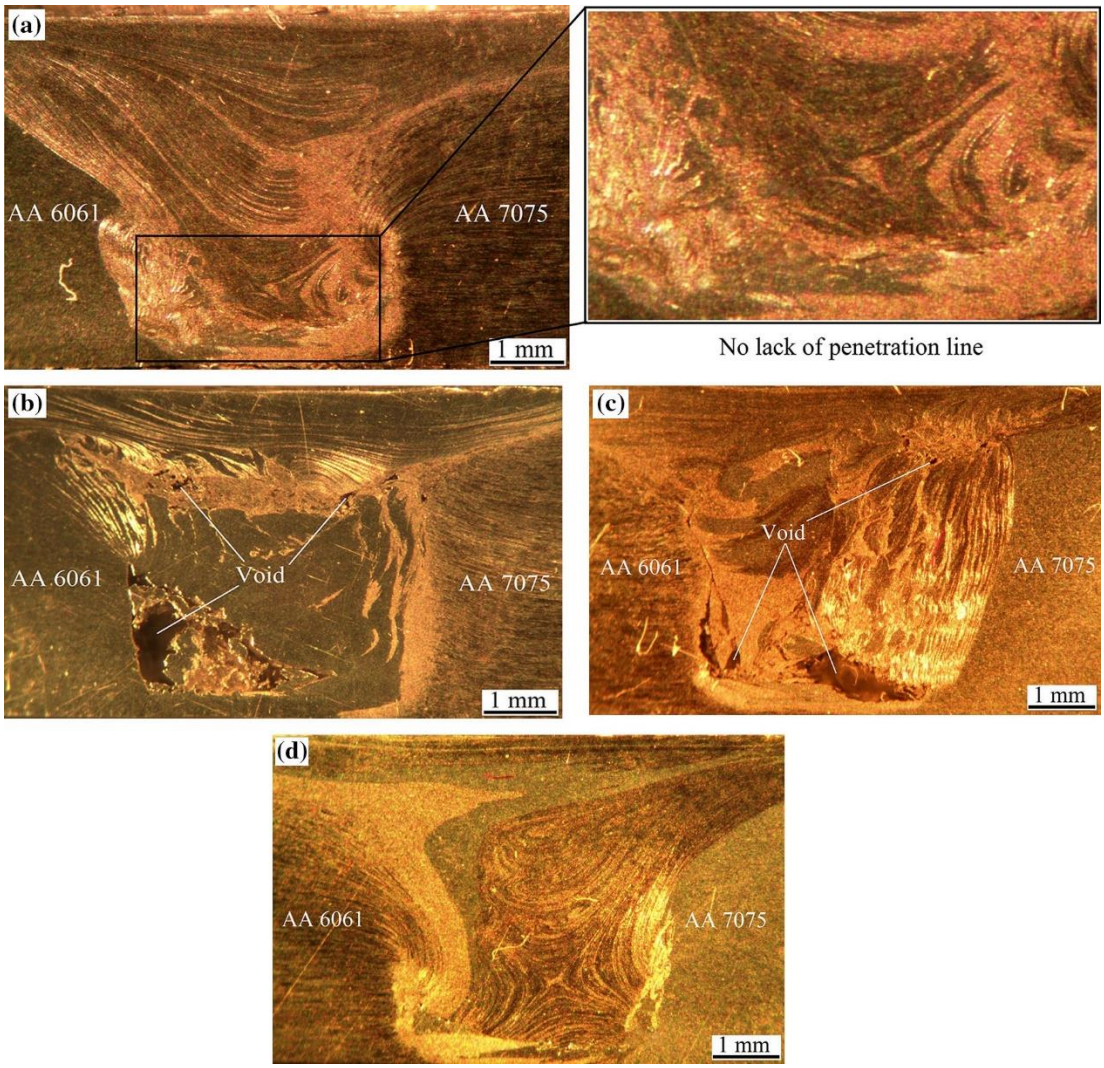

Figure 26: Macrostructure of the NZ produced at: (a, d) higher heat input condition and (b, c) lower heat input condition

In addition, the enlarged part of the NZ bottom of the defect-free joint (Figure 26-a) reveals a complete welding penetration to the bottom of the joint. The lack of penetration defect usually forms when the FSW tool pin is distant from the backing plate. Thus, in this study due to a sufficient depth of penetration (the pin length, plunging depth and plate thickness were 4.7, 0.2 and 5 mm, respectively) this defect was not observed. The comparison between Fig. 25-b and c shows that by increasing the heat input (by decreasing the traverse speed from 350 to 200 mm/min at constant rotational speed of 1000 rpm) the amount of void defects decreases. Moreover, from Fig. 26-a and d it can be found that by decreasing the heat input (by decreasing the rotational speed from 2500 rpm to 2125 rpm at constant traverse speed of 50 mm/min) the width of the joints decreases to some extent. The higher rotational speeds or lower traverse speeds lead to defect-free joints, but can generate sufficient temperature and heat for some metallurgical occurrences such grain growth [46, 47], solubilization and coarsening of strengthening precipitates [48], and decrease in dislocation density [46], which reduces the UTS of the welds.

The counter and 3D surface diagrams for the El of the joints are illustrated in Figure 27. Rise in rotational speed and reduction in traverse speed result in higher El, continuously. Higher heat input situations (i.e., higher rotational speed and lower traverse speed) cause enough plastic deformation and the removal of the voids in the joints and hence lead to higher El. In addition, higher heat input situations result in grain growth, coarsening of precipitates and eliminating the dislocations. According to Figure 20, higher heat input situations cause larger D_{av}, which is not in accordance with higher El of the joints. Thus, the better El of the joints welded at higher heat input situations may be contributed to other reasons such as lower dislocation densities in these joints (Figure11).

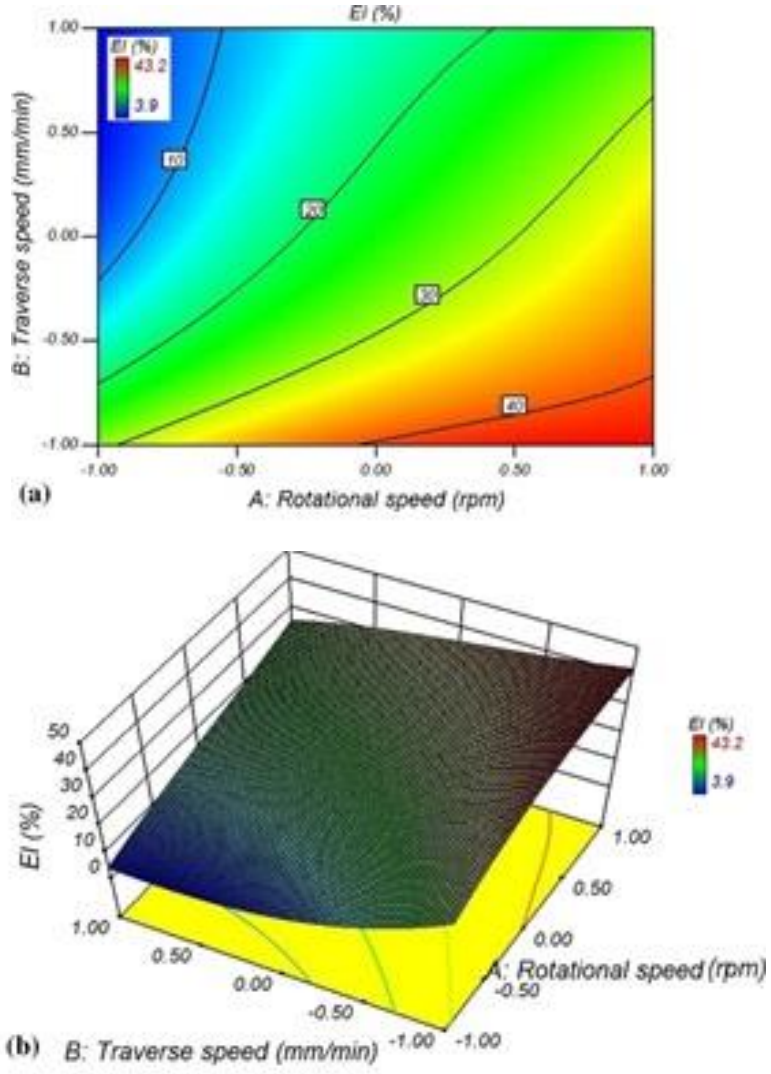

Figure 27: Counter and 3D surface plots for the response El

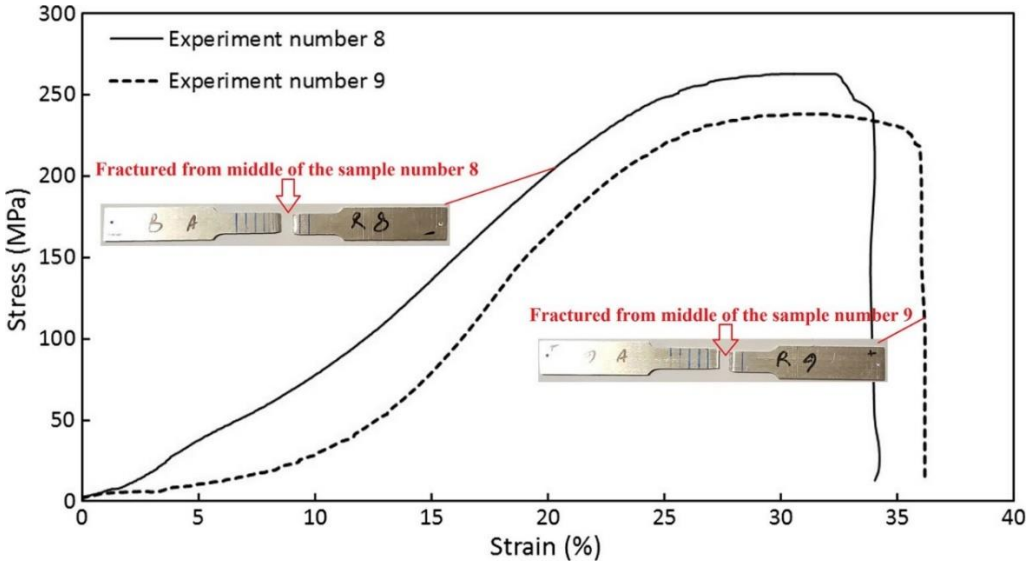

Figure 28: Stress–strain curves for the joints welded at lower heat input condition (experiment number 8) and higher heat input condition (experiment number 9)

Figure 12, fractography of the fractured tensile samples, and figure 28 prove that the higher El of the joints welded at higher heat input situations, which contains more and smaller dimples compared to the joint welded at the lower heat input situation.

For optimization aim, numerical and graphical methods were used in this investigation by selecting the favored goals for parameters and responses as summarized in Table 15.

Table 15: Goals and limitations considered for optimization process

Name	Goal	Lower limit	Upper limit
A: Rotational speed (rpm)	In range	1000	2500
B: Traverse speed (mm/min)	In range	50	350
UTS (MPa)	Maximize	48	262
El (%)	Maximize	3.9	5

The numerical method combines the goals into a global desirability function. The numerical method finds one point or more in the parameters area that would maximize the desirability function. In the case of graphical method with several responses, the software detects zones where necessities simultaneously encounter the suggested conditions. In addition, overlaying the critical response diagrams results in a distinct contour diagram, which makes a graphical search for the finest cooperation possible. The graphical method discloses the region of possible response in the parameter space.

The desirability and overlay diagrams for optimization aim are shown in Figure 29. These diagrams are achieved by maximizing both of the UTS and of El. Therefore, the optimization plots of Figure 29 disclose that the best condition for FSW (i.e., UTS = 237.3 MPa and El = 4.1%) was 1853 rpm and 50 mm/min for rotational and traverse

speeds, respectively. For more details, FSW of the dissimilar alloys was conducted under the optimized condition proposed by the model, and the UTS and El of the resulted joint were measured.

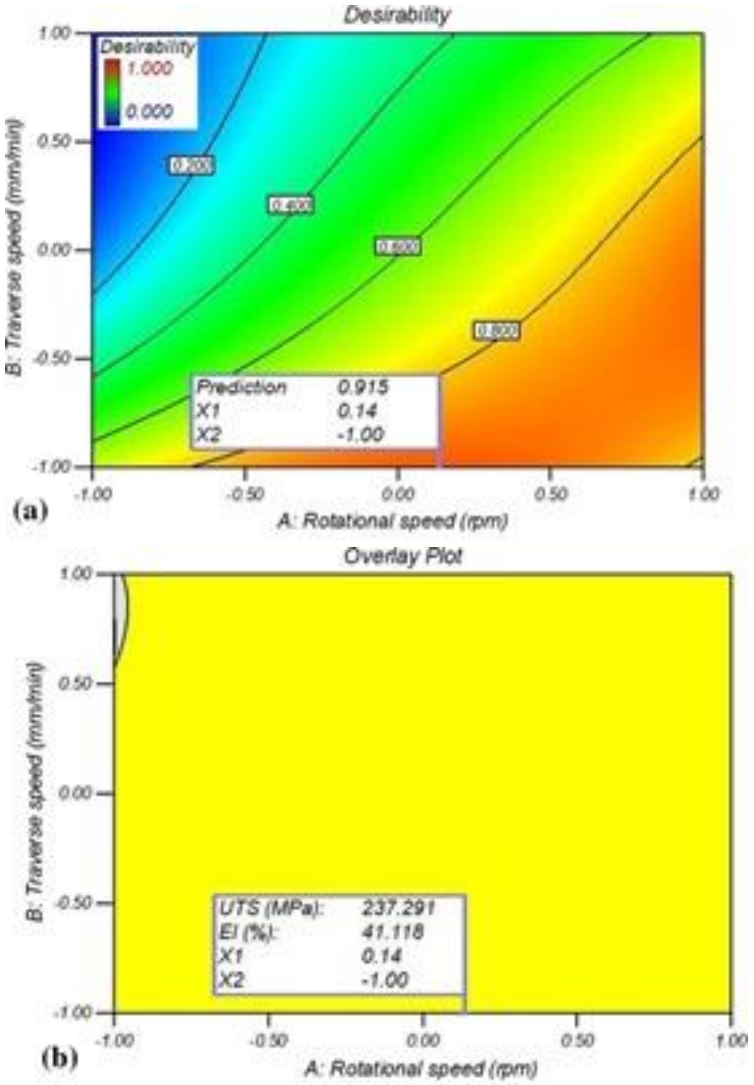

Figure 29: (a) Reliability and (b) overlay diagrams for optimizing the parameters

The UTS and El of the joint welded at optimized condition were 239 MPa and 39.4%, respectively.

Chapter 6

CONCLUSION

In this dissertation, underwater dissimilar FSW of AA6061-T6 and AA7075-T6 aluminum alloy plates was done and the effect of process parameters on the H, D_{av}, UTS and El of the produced joints was analyzed.

(i) By increasing the traverse speed up to 350 mm/min and increasing the rotational speed up 2125 rpm, heat input during FSW optimizes and the UTS of the joints increases up to the maximum value (80% efficacy) and then decreases. This behavior is related to the defect formation at lower heat inputs, and larger grain sizes and lower dislocation densities at higher heat inputs.

(ii) In the case of El, it increases continuously with decrease in traverse speed and increase in rotational speed when rise in heat input despite occurrence of the grain growth, which is related to the simultaneous defect elimination and reduction in the dislocation density. This behavior of the El is completely consistent with the more ductile fracture mode of the joints welded at higher heat inputs.

(iii) Hardness of the joints increases continuously with increase in traverse speed and decrease in rotational speed which lower the heat input. The strengthening mechanisms of grain boundary and dislocation effects are the main reasons for the higher hardness at lower heat inputs.

(iv) By decreasing the tool traverse speed up to 172 mm/min and decreasing the tool rotational speed up 1375 rpm, the D_{av} in the NZ of the joints decrease. This behavior is due to lower peak temperature and higher heating rate which cause lesser grain growth.

(v) Similar to the other types of massive plastic deformation processes, the H–P equation is deviated from the linear relationship for the joints. This deviation is due to formation of substructures such as different density of the dislocations inside the NZ grains.

Chapter 7

FUTURE WORK

7.1 Introduction

While this thesis has demonstrated significant improvement in efficiency of FSW joints of AA6061-T6 and AA7075-T6 by changing ambient condition to WC, many opportunities for extending the scope of this thesis remain. This section presents some of these directions.

7.2 Similar and Dissimilar WC-FSW for Other Heat Treated Aluminum Alloys

Sine there are relatively few articles regarding FSW in WC condition compare to what in AC condition and advantages of employing WC FSW to join the heat treated aluminum alloys, there are many opportunities to extend this research for similar and dissimilar materials.

7.3 Optimization with Fuzzy Logic Algorithm

The driven practical data from experiment can be simulated by artificial intelligence techniques such as neural networks, fuzzy logic, RPLLN and etc. The artificial intelligence based models can be utilized to model and predict the behavior of output(s) of the plan regard to the input(s). In the next step computational artificial intelligent technique such as genetic algorithms and hybrid algorithms can be utilized to optimize the generated model to get better resolution in predicted results.

7.4 Submerged FSW with Different Liquid as Coolant

In this thesis water was used as a coolant rather than air however, there are many other liquids with different thermal capacity can be used. It is expected each coolant plays a unique role in variation of thermal condition of submerged FSW.

7.5 Different Backing Plate Materials

In this thesis steel backing plate was employed. As it is acknowledged, metals have relatively good thermal conductivity thus, the backing plate plays a significant role in disposal of generated heat. Therefore, various materials with different thermal capacity can be employed as the backing plate to extent the investigation.

7.6 Splash Cooling versus Submerged Cooling in FSW Process

In this thesis the subjected plates was immersed in the coolant however, for industrial applications it may not be applicable. Therefore, instead of immersing the plates in coolant, the coolant can be splashed to a certain area just behind the tool.

7.7 Investigation on Material Transfer from the FSW Tool to the Wake of the Weld

Since the temperature of the FSW process raise up to 400 °C or more and pin is under the excessive wear, it is possible for the peripheral material of the pin comes of and stays on the wake of the weld. If this hypothesis is for real it affects the composition and homogeneity of the NZ.

REFERENCES

[1] R.S. Mishra, Z.Y. Ma, "*Friction Stir Welding and Processing",* Materials Science and Engineering R 50, 2005, p 1–78.

[2] F.C. Liu, Z.Y. Ma, "*Influence of Tool Dimension and Welding Parameters on Microstructure and Mechanical Properties of Friction-Stir-Welded 6061-T651 Aluminum Alloy*", Metall. Mater. Trans. A 39, 2008, p 2378–2388.

[3] M. Jayaraman, R. Sivasubramanian, V. Balasubramanian, "*Establishing Relationship between the Base Metal Properties and Friction Stir Welding Process Parameters of Cast Aluminum Alloys*", Materials and Design 31, 2010, p 4567–4576.

[4] S.R. Ren, Z.Y. Ma, L.Q. Chen, "*Effect of Welding Parameters on Tensile Properties and Fracture Behavior of Friction Stir Welded Al–Mg–Si Alloy*", Scr. Mater. 56, 2007, p 69–72.

[5] S. Benavides, Y. Li, L.E. Murr, D. Brown, J.C. McClure, "*Low-Temperature Friction-Stir Welding of 2024 Aluminum*", Scr. Mater. 41, 1999, p 809–815.

[6] Y.S. Sato, H. Kokawa, M. Enomoto, "*Microstructural Evolution of 6063 Aluminum during Friction- Stir Welding*", Metall. Mater. Trans. A 30 (1999) 2429.

[7] J.F. Guo, H.C. Chen, C.N. Sun, G. Bi, Z. Sun, J. Wei, "*Friction Stir Welding of Dissimilar Materials between AA6061and AA7075 Al Alloys Effects of Process Parameters*", Materials and Design 56, 2014, p 185–192.

[8] R.D. Fu, Z.Q. Sun, R.C. Sun, Y. Li, H.J. Liu, L. Liu, "*Improvement of Weld Temperature Distribution and Mechanical Properties of 7050 Aluminum Alloy Butt Joints by Submerged Friction Stir Welding",* Mater. Des. 32, 2011, p 4825–4831.

[9] L. Fratini, G. Buffa, R. Shivpuri, "*Mechanical and Metallurgical Effects of In Process Cooling During Friction Stir Welding of AA7075-T6 Butt Joints*", Acta Materialia 58, 2010, p 2056–2067.

[10] Y. Zhao, Q. Wang, H. Chen, K. Yan, "*Microstructure and Mechanical Properties of Spray Formed 7055 Aluminum Alloy by Underwater Friction Stir Welding*", Materials and Design 56, 2014, p 725–730.

[11] S.G. Epstein, J.G. Kaufman, P. Pollak, "*Aluminum and Its Alloys*", 1994, The Aluminum Association, Inc. Washington, D.C.

[12] S.W. Kallee, "*Friction Stir Welding in Series Production*", Automobil Produktion, December 2004.

[13] C.G. Rhodes, M.W. Mahoney, W.H. Bingel, R.A. Spurling, C.C. Bampton, "*Effects of Friction Stir Welding on Microstructure of 7075 Aluminum*" Scripta Materialia, 36(1), 1997, p 69-15.

[14] G. Liu, L.E. Murr, C-S. Niou, J.C. McClure, F.R. Vega, "*Microstructural Aspects of the Friction-Stir Welding of 6061-T6 Aluminum*", Scripta Materialia, 37(3), 1997, p. 355-361.

[15] K. V. Jata, S.L. Semiatin, "*Continuous Dynamic Recrystallization during Friction Stir Welding of High Strength Aluminum Alloys*", Scripta mater. 43, 2000, p 743–749.

[16] P.M.G.P. Moreira, T. Santos, S.M.O. Tavares, V. Richter-Trummer, P. Vilaça, P.M.S.T. de Castro, *"Mechanical and Metallurgical Characterization of Friction Stir Welding Joints of AA6061-T6 with AA6082-T6"*, Materials and Design 30, 2009, p 180–187.

[17] D. Muruganandam, S. Ravikumar, S.L. Das, "*Mechanical and Micro Structural Behavior of 2024–7075 Aluminium Alloy Plates joined by Friction Stir Welding*", IEEE, 2010, doi:978-1-4244-9082-0.

[18] R. Palanivel, P. Koshy Mathews, N. Murugan, I. Dinaharan, "*Effect of Tool Rotational Speed and Pin Profile on Microstructure and Tensile Strength of Dissimilar Friction Stir Welded AA5083-H111 and AA6351-T6 Aluminum Alloys*", Materials and Design 40, 2012, p 7–16.

[19] P. Cavaliere, A. de Santis, F. Panella, A. Squillace, "*Effect of Welding Parameters on Mechanical and Microstructural Properties of Dissimilar AA6082–AA2024 Joints Produced by Friction Stir Welding*" Materials and Design 30, 2009, p 609–616.

[20] S.A. Khodir, T. Shibayanagi, "*Friction Stir Welding of Dissimilar AA2024 and AA7075 Aluminum Alloys*", Materials Science and Engineering B 148, 2008, p 82–87.

[21] S.T. Amancio-Filho, S. Sheikhia, J.F. dos Santosa, C. Bolfarini, "*Preliminary Study on the Microstructure and Mechanical Properties of Dissimilar Friction Stir Welds in Aircraft Aluminum Alloys 2024-T351 and 6056-T4*", Materials Processing Technology 206, 2008, p 132–142.

[22] Y.C. Chen, J.C. Feng, H.J. Liu, "*Precipitate Evolution in Friction Stir Welding of 2219-T6 Aluminum Alloys*", Materials Characterization 60, 2009, p 476–481.

[23] C. Rathinasuriyana, V.S. Senthil Kumarb, A. G. Shanbhag, "*Radiography and Corrosion Analysis of Sub-merged Friction Stir Welding of AA6061-T6 alloy*", Procedia Engineering 97, 2014, p 810–818.

[24] Z. Zhang, B.L. Xiao, Z.Y. Ma, "*Influence of Water Cooling on Microstructure and Mechanical Properties of Friction Stir Welded 2014Al-T6 Joints*", Materials Science & Engineering A 614, 2014, p 6–15.

[25] L. Fratini, G. Buffa, R. Shivpuri, "*in-Process Heat Treatments to Improve FS-Welded Butt Joints*", Adv. Manuf. Technol. 43, 2009, p 664–670.

[26] S.K. Park, S.T. Hong, J.H. Park, K.Y. Park, Y.J. Kwon, H.J. Son, "*Effect of Material Locations on Properties of Friction Stir Welding Joints of Dissimilar Aluminium Alloys*", Sci. Technol. Weld Joining 15, 2010, p 331–336.

[27] Information provided by The Aluminum Association, Inc. from Aluminum Standards and Data 2000 and/or International Alloy Designations and Chemical Composition Limits for Wrought Aluminum and Wrought Aluminum Alloys (Revised 2001).

[28] Special Steels Catalogue, www.macsteel.co.za, Lea Road, Dunswart, P O Box 6130, Dunswart 1508 - South Africa

[29] M. Dehghani, S. A. A. akbari mousavi, A. Amadeh, "*Effects of Welding Parameters and Tool Geometry on Properties of 3003-H18 Aluminum Alloy to Mild Steel Friction Stir Weld*", Trans. Nonferrous Met. Soc. China 23, 2013, p 1957−1965.

[30] W. Xu, J. Liu, H. Zhu, L. Fu, "*Influence of Welding Parameters and Tool Pin Profile on Microstructure and Mechanical Properties Along the Thickness in a Friction Stir Welded Aluminum Alloy*", Materials and Design 47, 2013, p 599–606.

[31] R. Nandan, T. DebRoy, H.K.D.H. Bhadeshia, "*Recent Advances in Friction-Stir Welding – Process, Weldment Structure and Properties*", Progress in Materials Science 53, 2008, p 980–1023.

[32] M. Farhanchi, M Neysari, R.V. Barenji, A. Heiidarzadeh "*Mechanical Activation Process for Self-Propagation High-Temperature Synthesis of Ceramic-Based Composites*", J Therm Anal Calorim 122, 2015, p 123–133.

[33] A. Heidarzadeh, R.V. Barenji, M. Esmaily, A.R. Ilkhchi, "*Tensile Properties of Friction Stir Welds of AA 7020 Aluminum Alloy*", Trans Ind Inst Metal 68, 2015, p 757–767.

[34] A.R. Ilkhichi, R. Soufi, G. Hussain, R.V. Barenji, A. Heidarzadeh, "*Establishing Mathematical Models to Predict Grain Size and Hardness of the Friction Stir-Welded AA 7020 Aluminum Alloy Joints*", Metal Mater Trans B 46, 2015, p 357–365.

[35] R.V. Barenji, "*Influence of Heat Input Conditions on Microstructure Evolution and Mechanical Properties of Friction Stir Welded Pure Copper Joints*" Trans Indian Inst. Metal 69(5), 2015, doi:10.1007/s12666-015-0624-7.

[36] A. Heidarzadeh, T, Saeid, "*A Comparative Study of Microstructure and Mechanical Properties between Friction Stir Welded Single and Double Phase Brass Alloys*", Mater Sci Eng A 649, 2016, p 349–358.

[37] S. Mironov, K. Inagaki, Y.S. Sato, H. Kokawa, "*Development of Grain Structure during Friction-Stir Welding of Cu–30Zn Brass*", Philos Mag 94, 2014, p 3137–3148.

[38] A. Heidarzadeh, T, Saeid, V. Klemm, "*Microstructure, Texture, and Mechanical Properties of Friction Stir Welded Commercial Brass Alloy*", Mater Charact 119, 2016, p 84–91.

[39] S. Mironov, K. Inagaki, Y.S. Sato, H. Kokawa, "*Microstructural Evolution of Pure Copper during Friction-Stir Welding*", Philos Mag 95, 2015, p 367–381.

[40] E. Ghassemali, M-J. Tan, C.B. Wah, S.C.V Lim, A.E.W. Jarfors, "*Effect of Cold Work on the Hall–Petch Breakdown in Copper Based Micro-Components*", Mech Mater 80, 2015, p 124–135.

[41] D. Du, R. Fu, Y. Li, L. Jing, J. Wang, Y. Ren, K. Yang, "*Modification of the Hall–Petch Equation For Friction-Stir-Processing Microstructures of High-Nitrogen Steel*", Mater Sci. Eng. A 40, 2015, p 190–194.

[42] G. Gao, Z, Zhu, J. Han, H. Li "*Correlation of Microstructure and Mechanical Properties in Friction Stir Welded 2198-T8 Al–Li Alloy*", Mater Sci. Eng. A 639, 2015, p 489–499.

[43] Y.S. Sato, S.H.C. Park, H. Kokawa, "*Microstructural Factors Governing Hardness in Friction-Stir Welds of Solid-Solution-Hardened Al Alloys*", Metal Mater Trans A 32, 2001, p 3033–3042.

[44] M.J. Jones, P. Heurtier, C. Desrayaud, F. Montheillet, D. Allehaux, J.H. Driver, "*Correlation between Microstructure and Microhardness in a Friction Stir Welded 2024 Aluminium Alloy*", Scripta Mater 52, 2005, p 693–697.

[45] Y.S. Sato, M. Urata, H. Kokawa, K. Ikeda, "*Hall–Petch Relationship in Friction Stir Welds of Equal Channel Angular Pressed Aluminium Alloys*", Mater Sci. Eng. A 354, 2003, p 298–305.

[46] A. Heidarzadeh, H. Khodaverdizadeh, A. Mahmoudi, E. Nazari, "*Tensile Behavior of Friction Stir Welded AA 6061-T4 Aluminum Alloy Joints"*, Mater. Des. 37, 2012, p 166–173, doi:10.1016/j.

[47] S. Rajakumar and V. Balasubramanian, "*Establishing Relationships Between Mechanical Properties of Aluminium Alloys and Optimized Friction Stir Welding Process Parameters*", Mater. Des. 40, 2012, p 17–35. doi:10.1016/j.

[48] S. Rajakumar, C. Muralidharan, V. Balasubramanian, "*Predicting Tensile Strength, Hardness and Corrosion Rate of Friction Stir Welded AA6061-T6 Aluminium Alloy Joints*", Mater. Des. 32(5), 2011, p 2878–2890. doi:10.1016/j.

APPENDICES

Appendix A: Temperature Profiles of the Joints

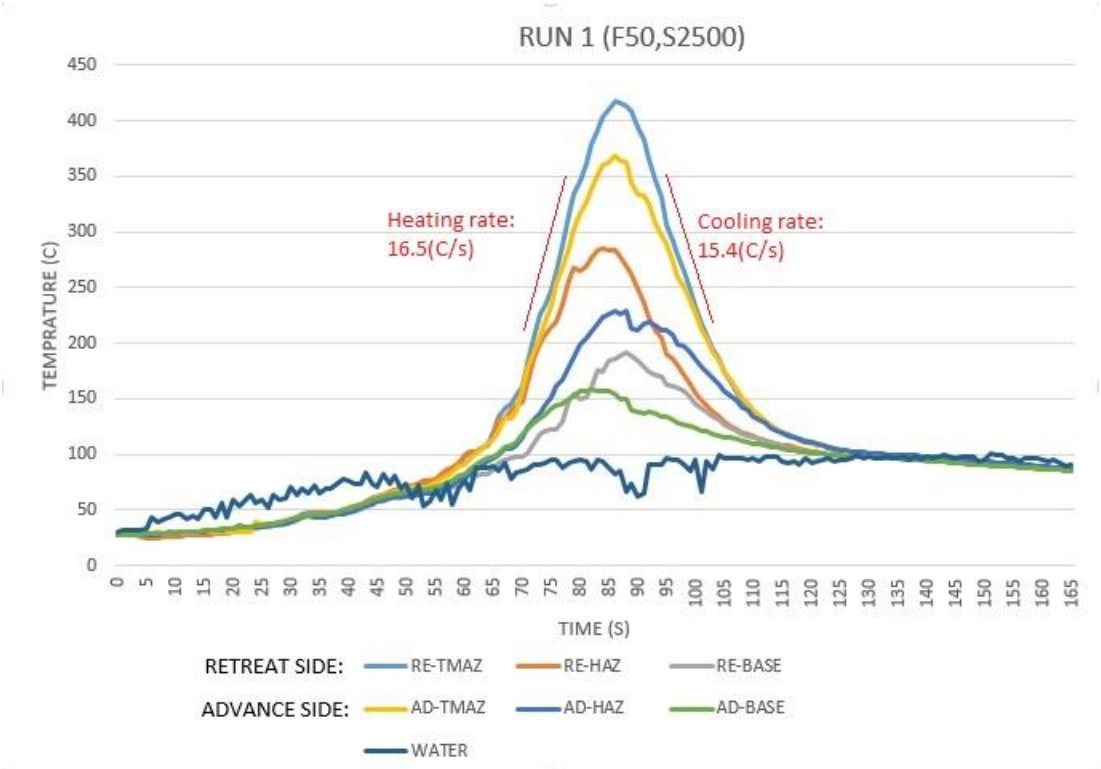

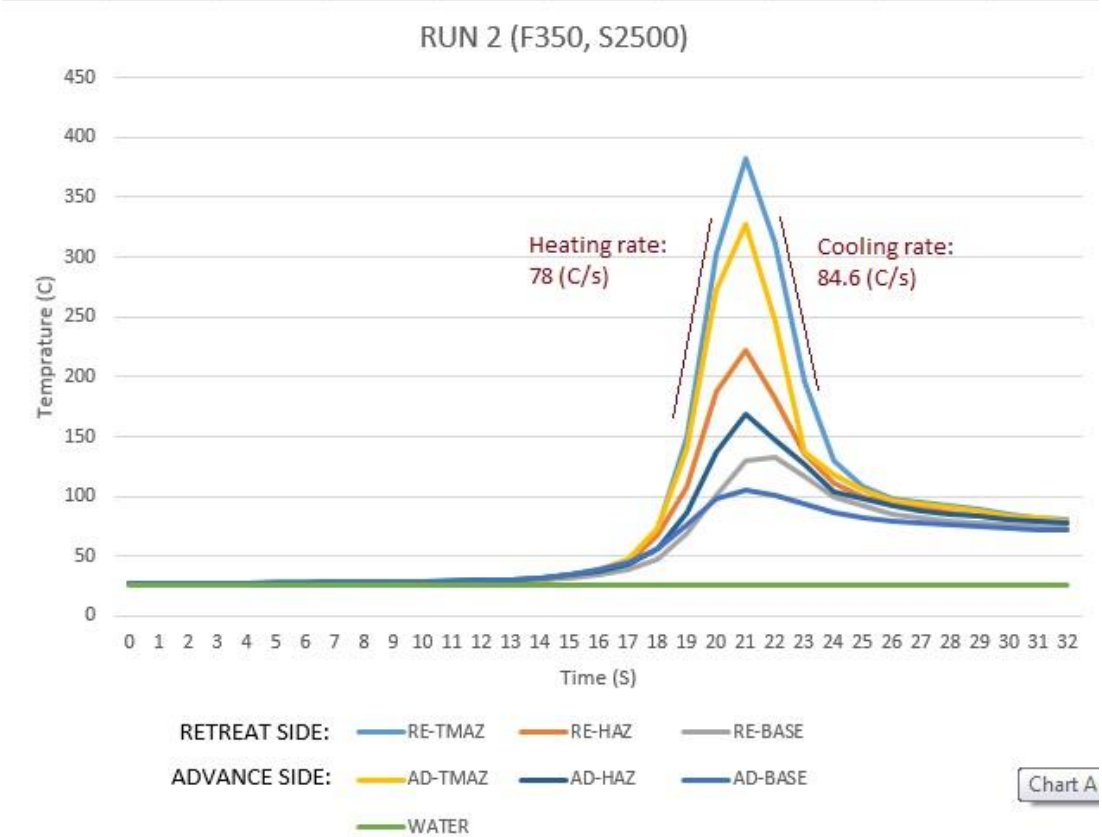

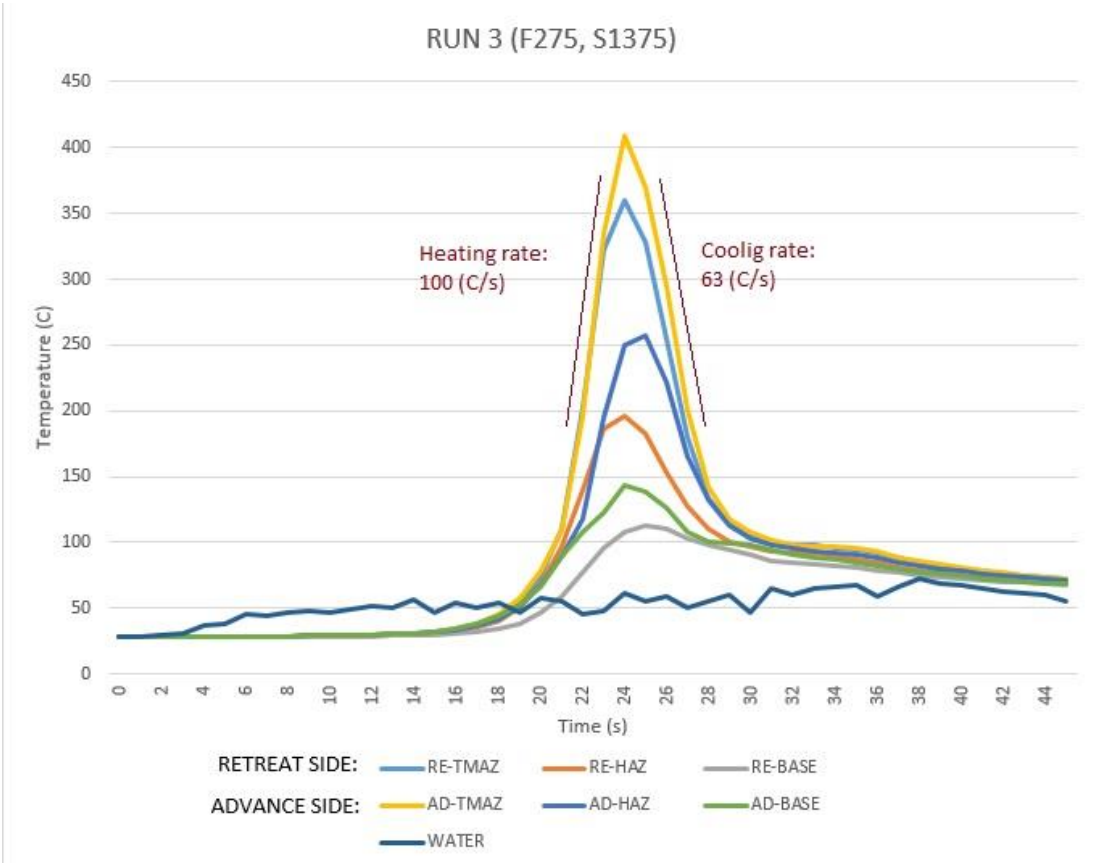
RUN 3 (F275, S1375)
Temperature (C)
Time (s)
Heating rate:
100 (C/s)
Coolig rate:
63 (C/s)
RETREAT SIDE:
RE-TMAZ
RE-HAZ
RE-BASE
ADVANCE SIDE:
AD-TMAZ
AD-HAZ
AD-BASE
WATER

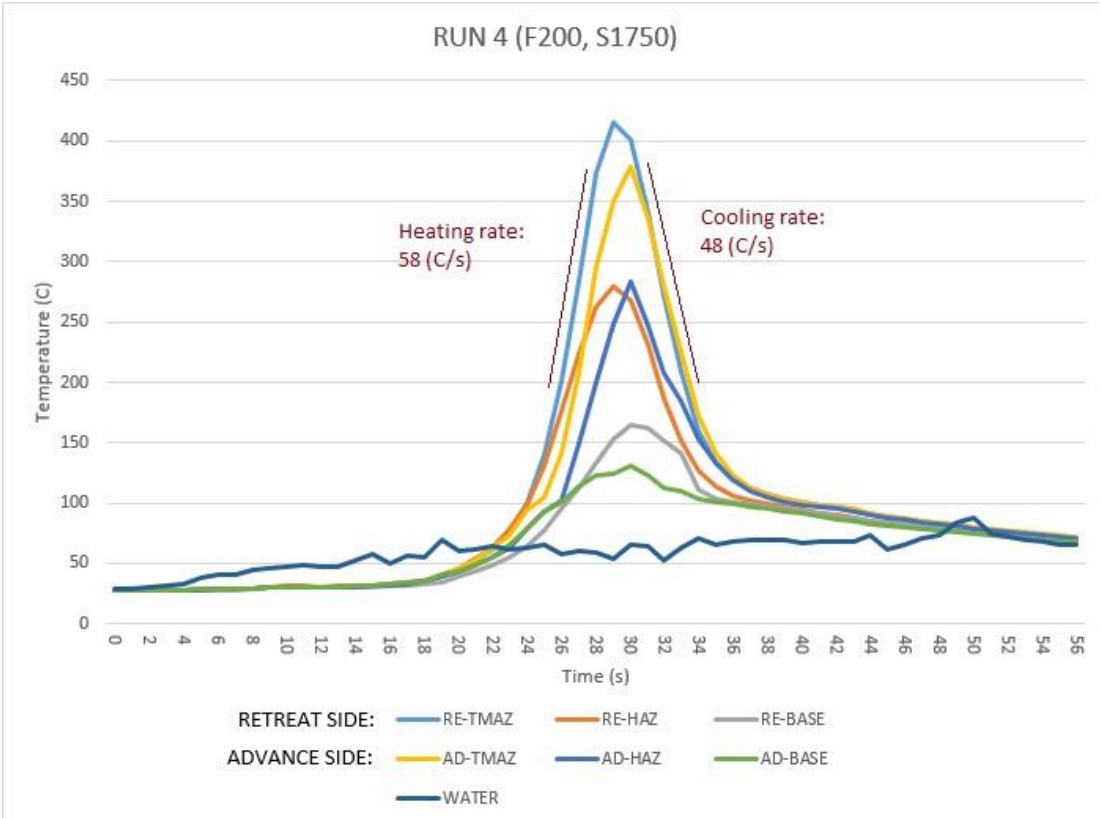
RUN 4 (F200, S1750)
Temperature (C)
Time (s)
Heating rate:
58 (C/s)
Cooling rate:
48 (C/s)
RETREAT SIDE:
RE-TMAZ
RE-HAZ
RE-BASE
ADVANCE SIDE:
AD-TMAZ
AD-HAZ
AD-BASE
WATER

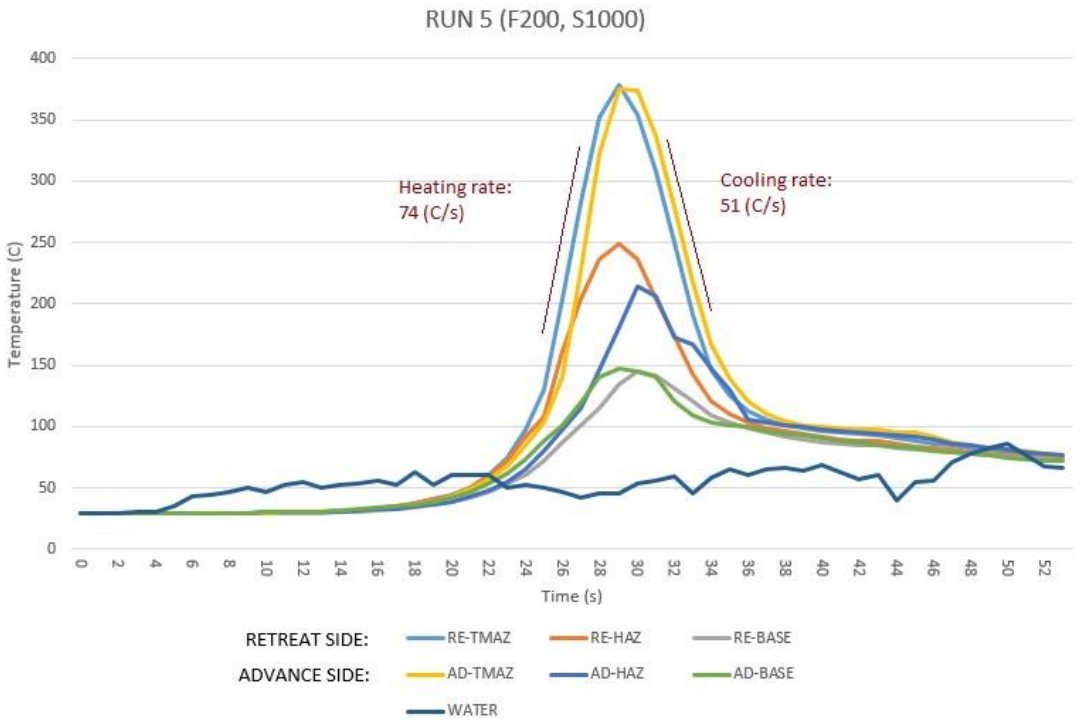
RUN 5 (F200, S1000)
Temperature (C)
Time (s)
Heating rate:
74 (C/s)
Cooling rate:
51 (C/s)
RETREAT SIDE:
RE-TMAZ
RE-HAZ
RE-BASE
ADVANCE SIDE:
AD-TMAZ
AD-HAZ
AD-BASE
WATER

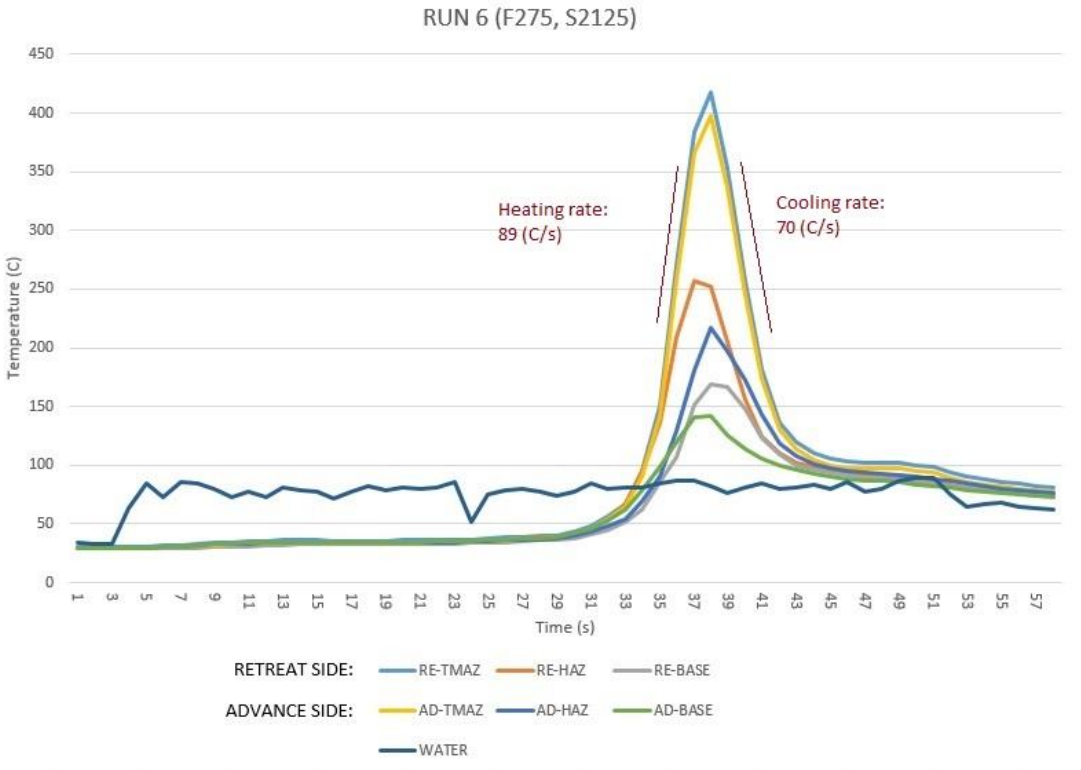
RUN 6 (F275, S2125)
Temperature (C)
Time (s)
Heating rate:
89 (C/s)
Cooling rate:
70 (C/s)
RETREAT SIDE:
RE-TMAZ
RE-HAZ
RE-BASE
ADVANCE SIDE:
AD-TMAZ
AD-HAZ
AD-BASE
WATER

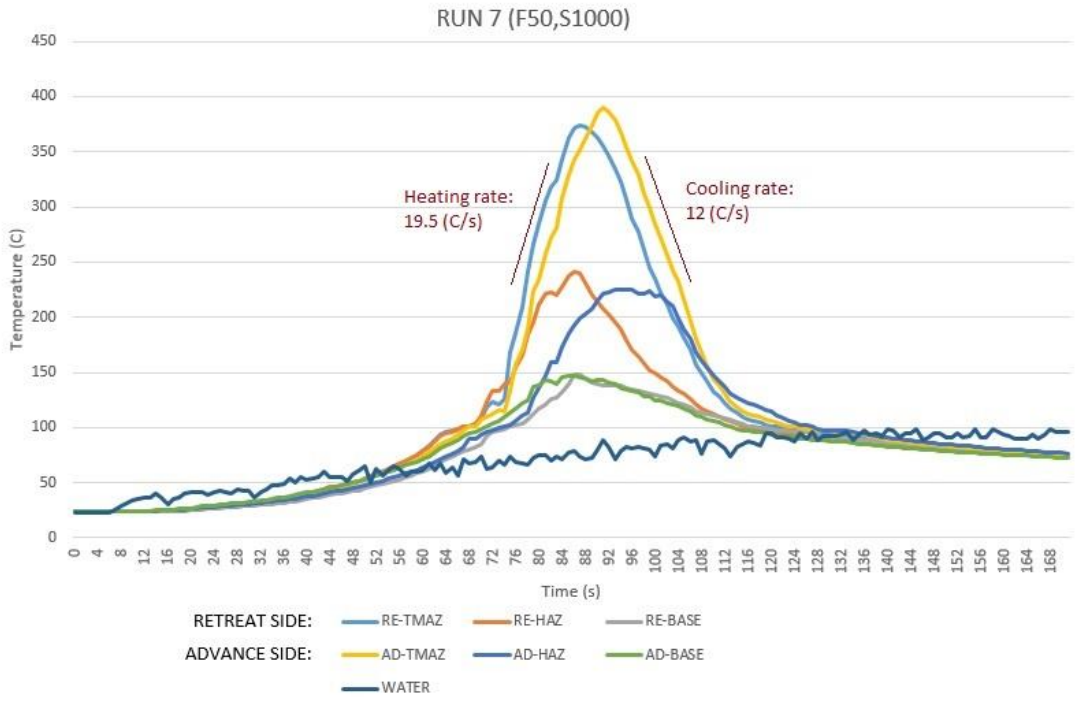
RUN 7 (F50,S1000)
Heating rate:
19.5 (C/s)
Cooling rate:
12 (C/s)
Temperature (C)
Time (s)
RETREAT SIDE:
RE-TMAZ
RE-HAZ
RE-BASE
ADVANCE SIDE:
AD-TMAZ
AD-HAZ
AD-BASE
WATER

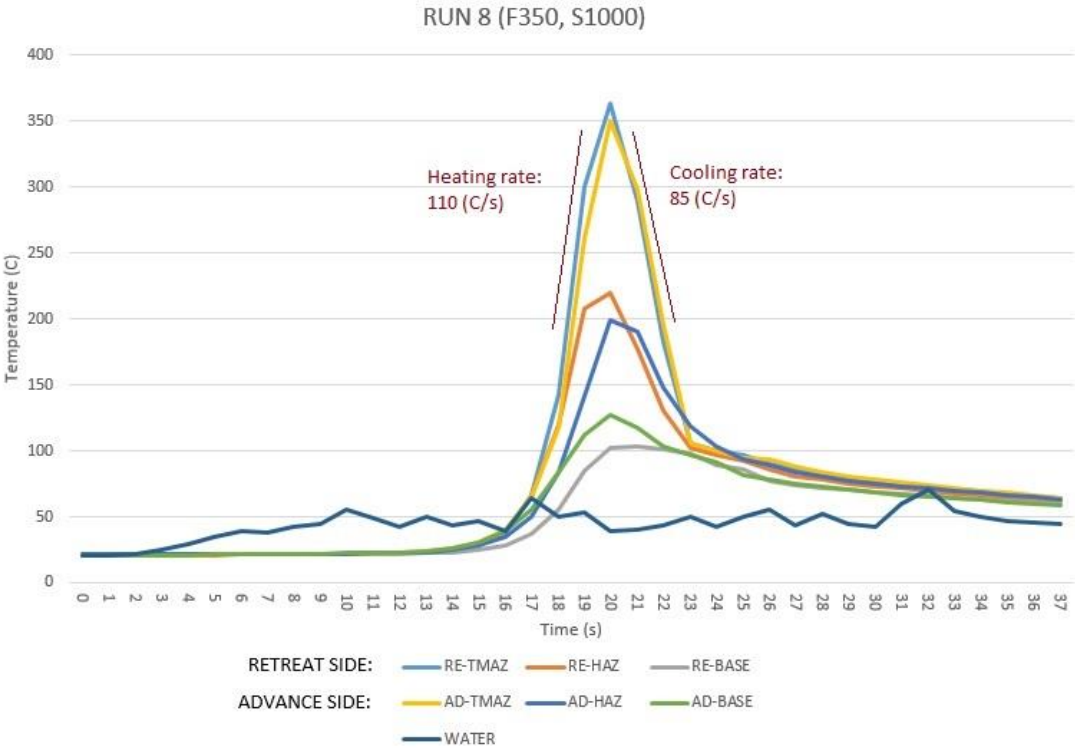
RUN 8 (F350, S1000)
Heating rate:
110 (C/s)
Cooling rate:
85 (C/s)
Temperature (C)
Time (s)
RETREAT SIDE:
RE-TMAZ
RE-HAZ
RE-BASE
ADVANCE SIDE:
AD-TMAZ
AD-HAZ
AD-BASE
WATER

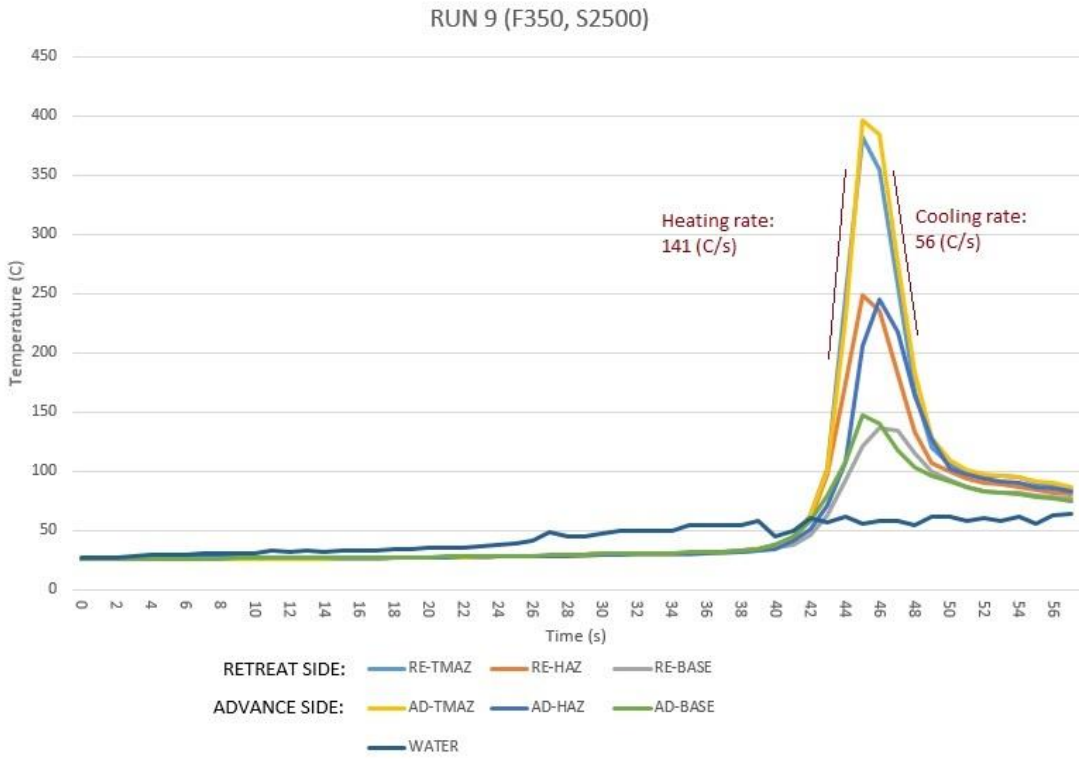
RUN 9 (F350, S2500)
Temperature (C)
Time (s)
Heating rate:
141 (C/s)
Cooling rate:
56 (C/s)
RETREAT SIDE:
RE-TMAZ
RE-HAZ
RE-BASE
ADVANCE SIDE:
AD-TMAZ
AD-HAZ
AD-BASE
WATER

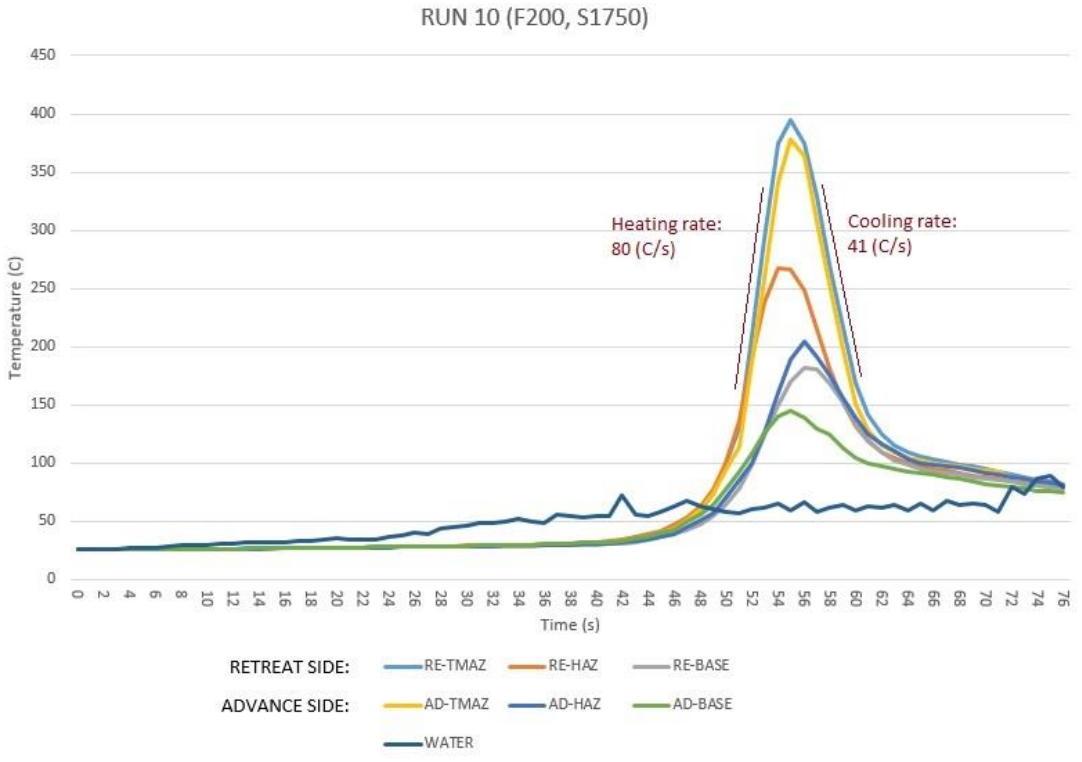
RUN 10 (F200, S1750)
Temperature (C)
Time (s)
Heating rate:
80 (C/s)
Cooling rate:
41 (C/s)
RETREAT SIDE:
RE-TMAZ
RE-HAZ
RE-BASE
ADVANCE SIDE:
AD-TMAZ
AD-HAZ
AD-BASE
WATER

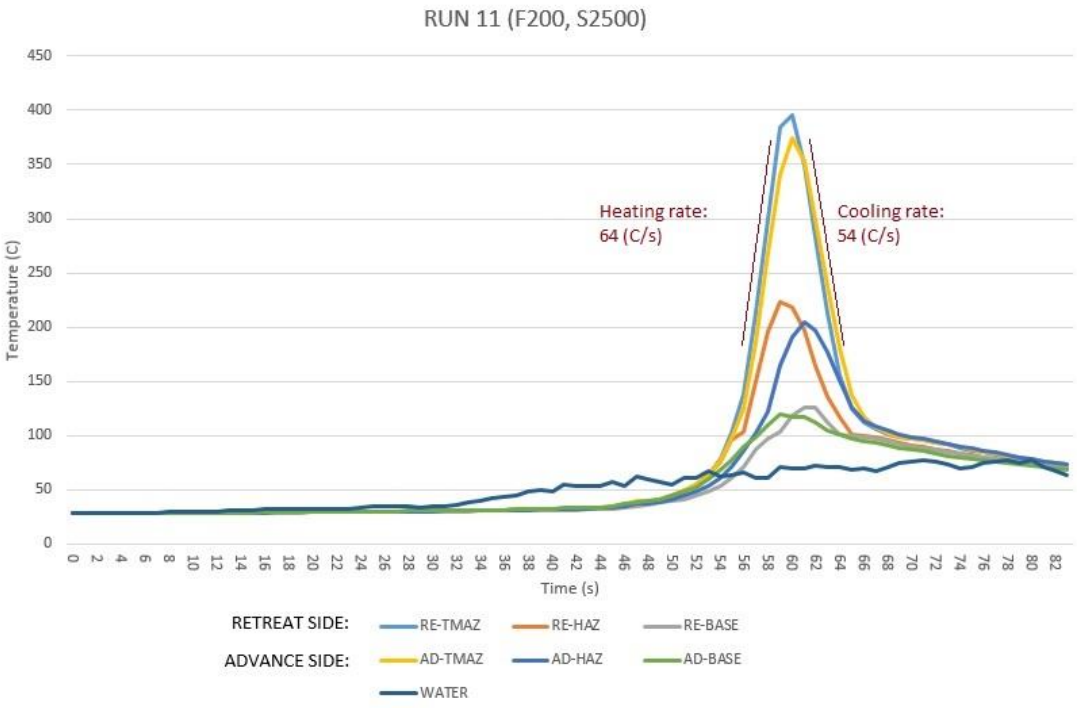
RUN 11 (F200, S2500)
Temperature (C)
Time (s)
Heating rate:
64 (C/s)
Cooling rate:
54 (C/s)
RETREAT SIDE:
RE-TMAZ
RE-HAZ
RE-BASE
ADVANCE SIDE:
AD-TMAZ
AD-HAZ
AD-BASE
WATER

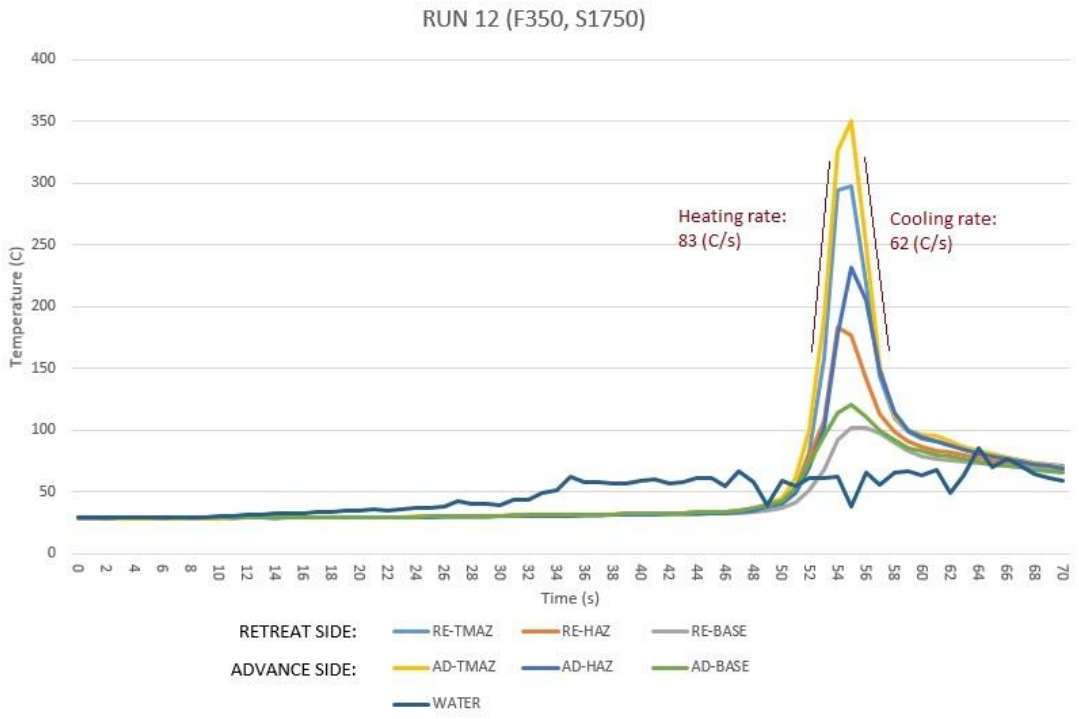
RUN 12 (F350, S1750)
Temperature (C)
Time (s)
Heating rate:
83 (C/s)
Cooling rate:
62 (C/s)
RETREAT SIDE:
RE-TMAZ
RE-HAZ
RE-BASE
ADVANCE SIDE:
AD-TMAZ
AD-HAZ
AD-BASE
WATER

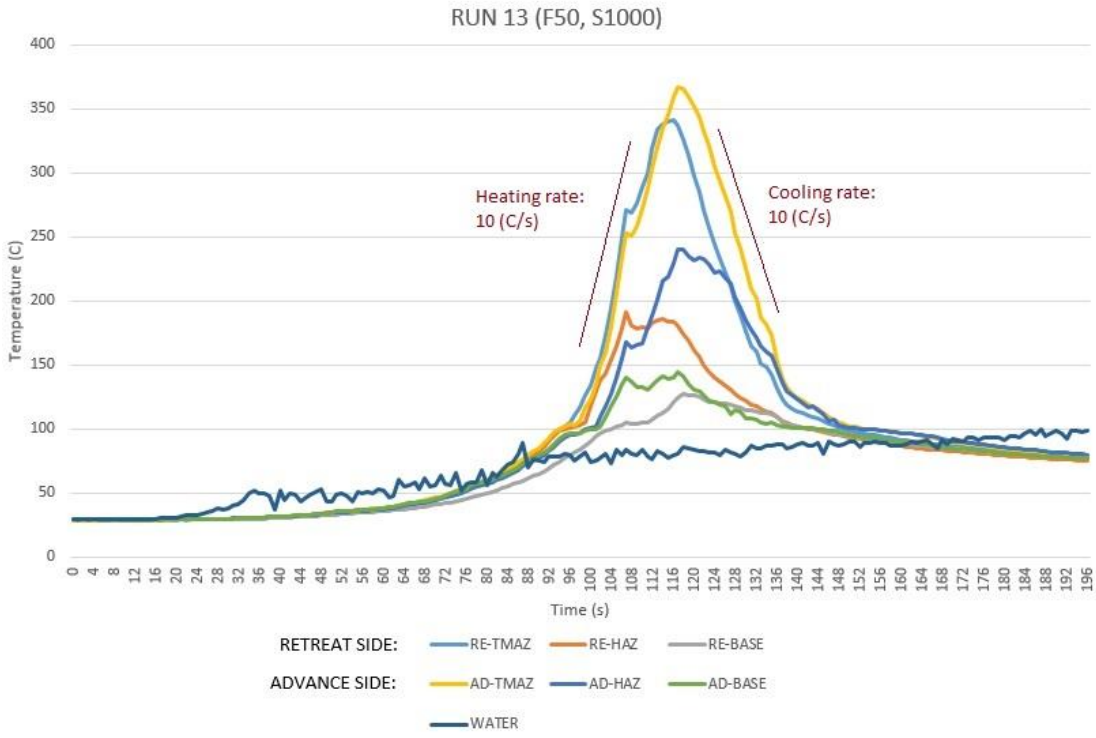
RUN 13 (F50, S1000)
Heating rate:
10 (C/s)
Cooling rate:
10 (C/s)
Temperature (C)
Time (s)
RETREAT SIDE:
RE-TMAZ
RE-HAZ
RE-BASE
ADVANCE SIDE:
AD-TMAZ
AD-HAZ
AD-BASE
WATER

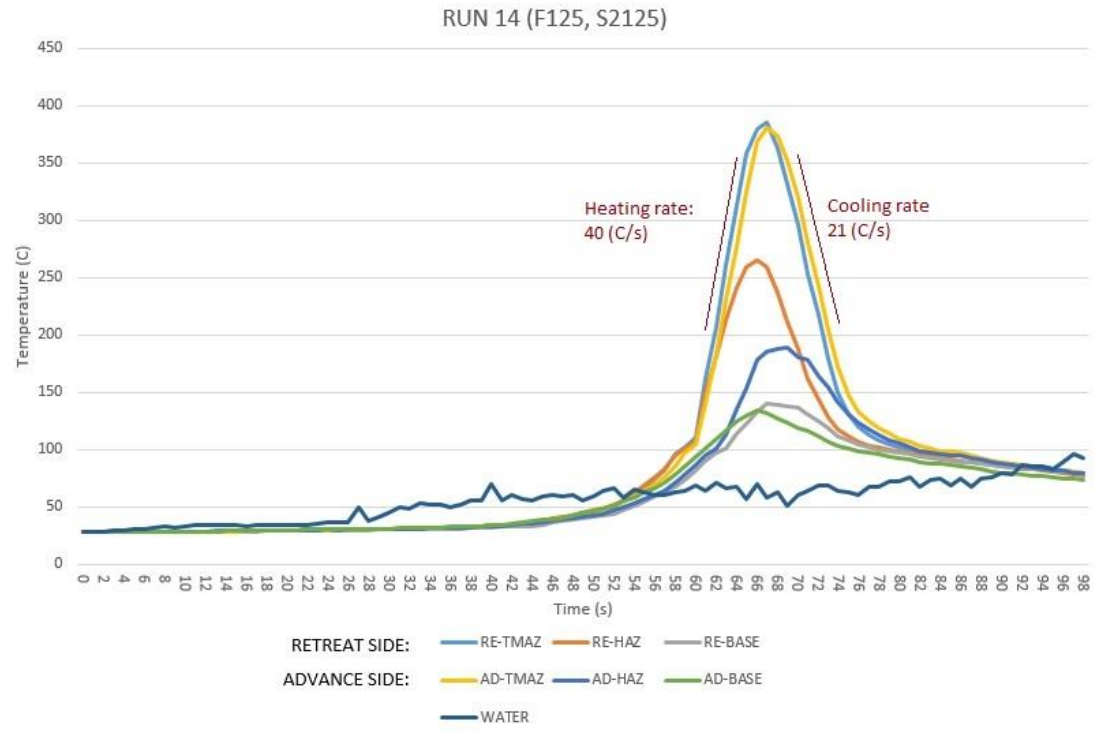
RUN 14 (F125, S2125)
Heating rate:
40 (C/s)
Cooling rate
21 (C/s)
Temperature (C)
Time (s)
RETREAT SIDE:
RE-TMAZ
RE-HAZ
RE-BASE
ADVANCE SIDE:
AD-TMAZ
AD-HAZ
AD-BASE
WATER

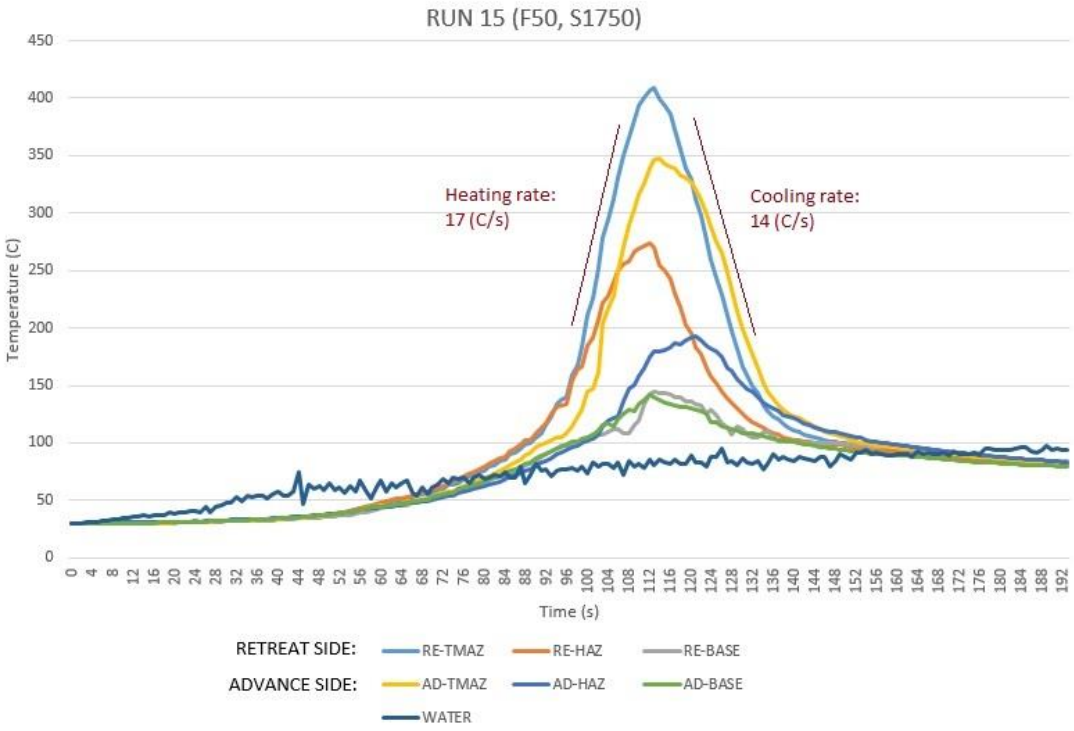
RUN 15 (F50, S1750)
Heating rate:
17 (C/s)
Cooling rate:
14 (C/s)
Temperature (C)
Time (s)
RETREAT SIDE:
RE-TMAZ
RE-HAZ
RE-BASE
ADVANCE SIDE:
AD-TMAZ
AD-HAZ
AD-BASE
WATER

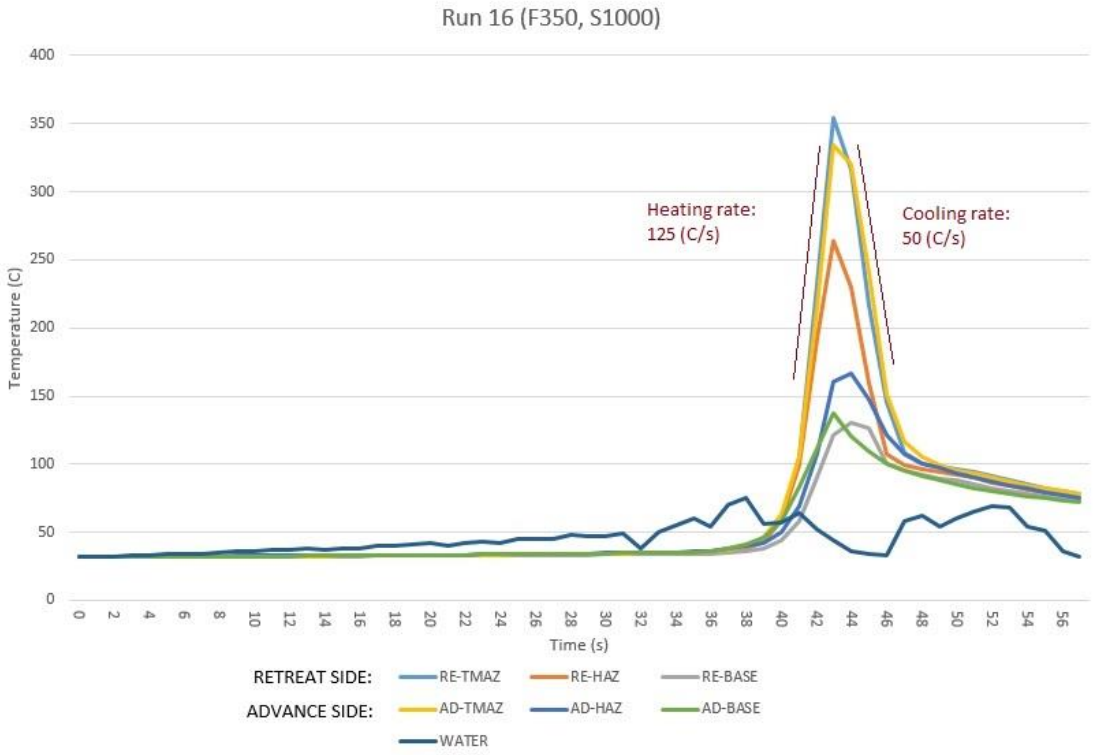
Run 16 (F350, S1000)
Heating rate:
125 (C/s)
Cooling rate:
50 (C/s)
Temperature (C)
Time (s)
RETREAT SIDE:
RE-TMAZ
RE-HAZ
RE-BASE
ADVANCE SIDE:
AD-TMAZ
AD-HAZ
AD-BASE
WATER

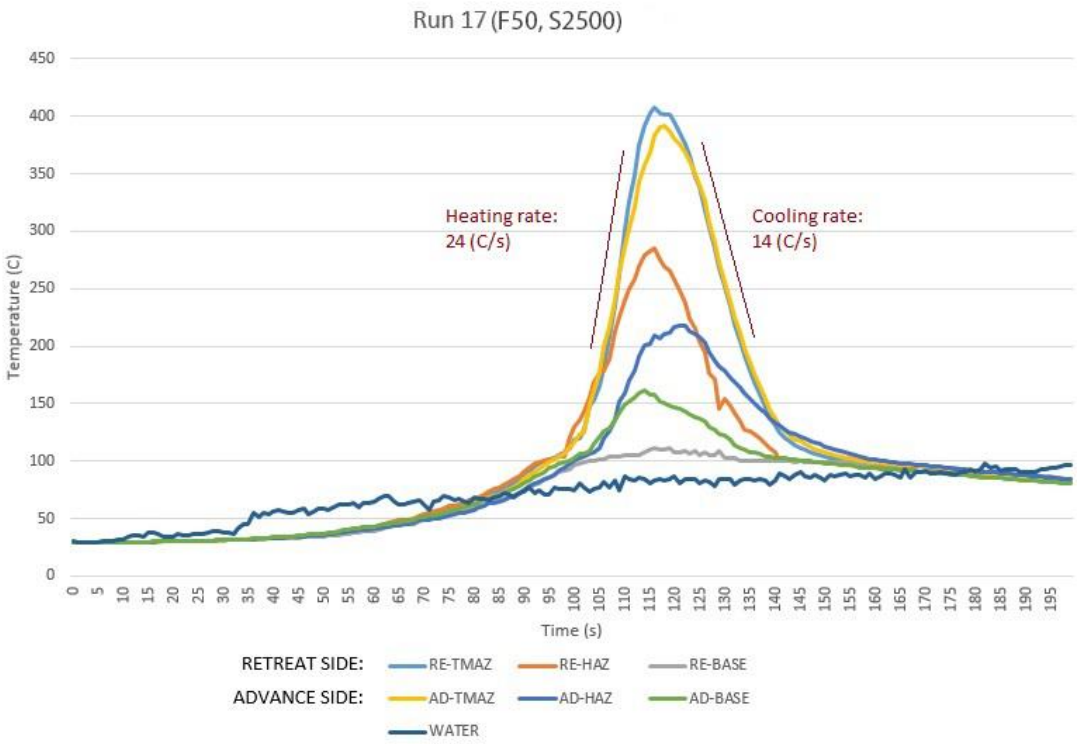
Run 17 (F50, S2500)
Temperature (C)
Time (s)
Heating rate:
24 (C/s)
Cooling rate:
14 (C/s)
RETREAT SIDE:
RE-TMAZ
RE-HAZ
RE-BASE
ADVANCE SIDE:
AD-TMAZ
AD-HAZ
AD-BASE
WATER

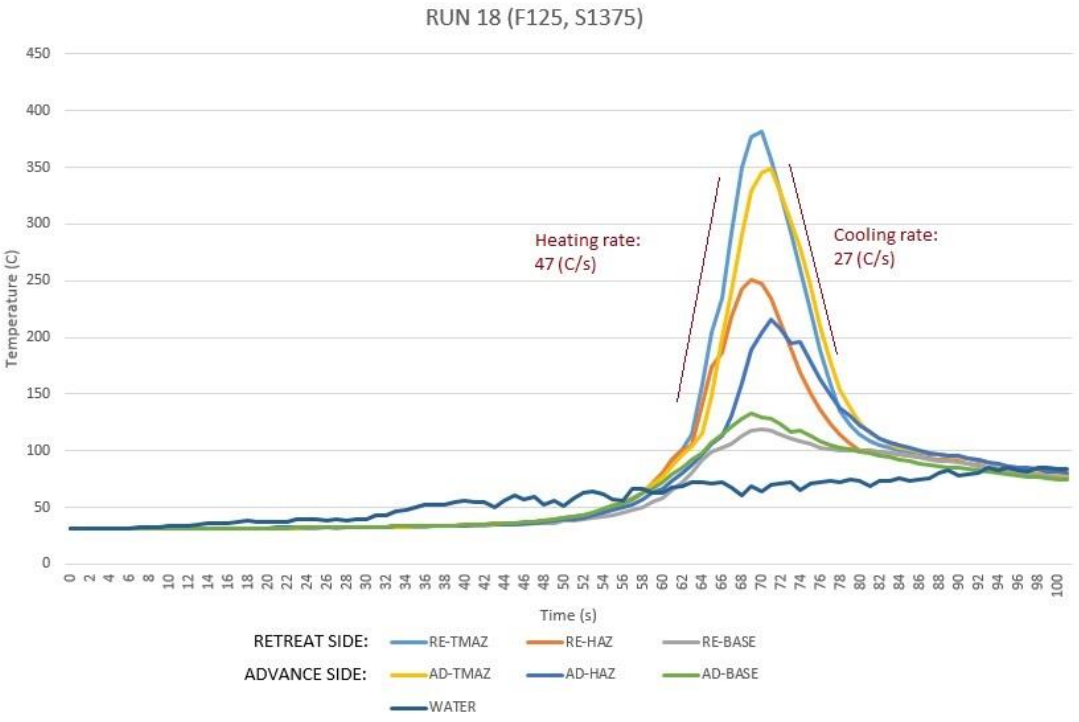
RUN 18 (F125, S1375)
Temperature (C)
Time (s)
Heating rate:
47 (C/s)
Cooling rate:
27 (C/s)
RETREAT SIDE:
RE-TMAZ
RE-HAZ
RE-BASE
ADVANCE SIDE:
AD-TMAZ
AD-HAZ
AD-BASE
WATER

Appendix B: Macrohardness Graph of the Joints

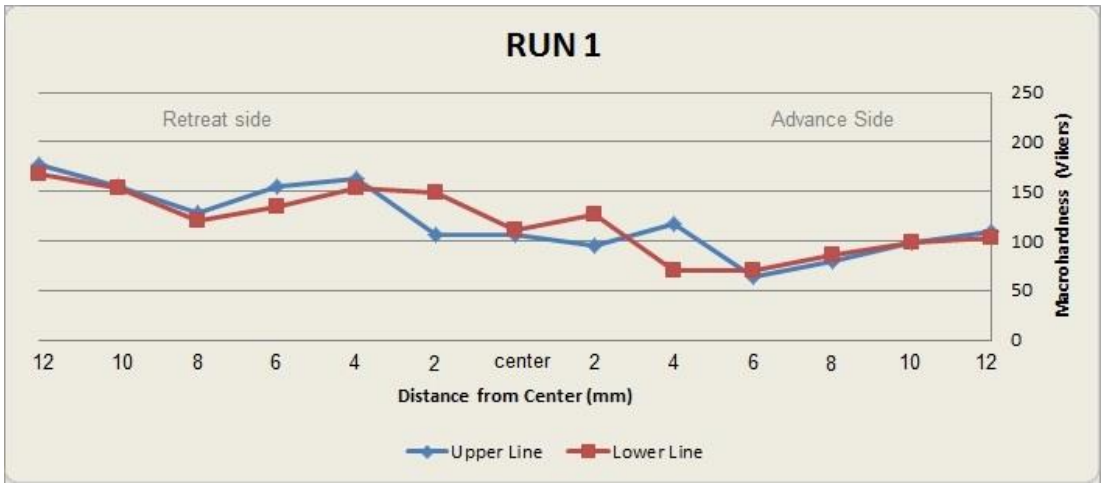

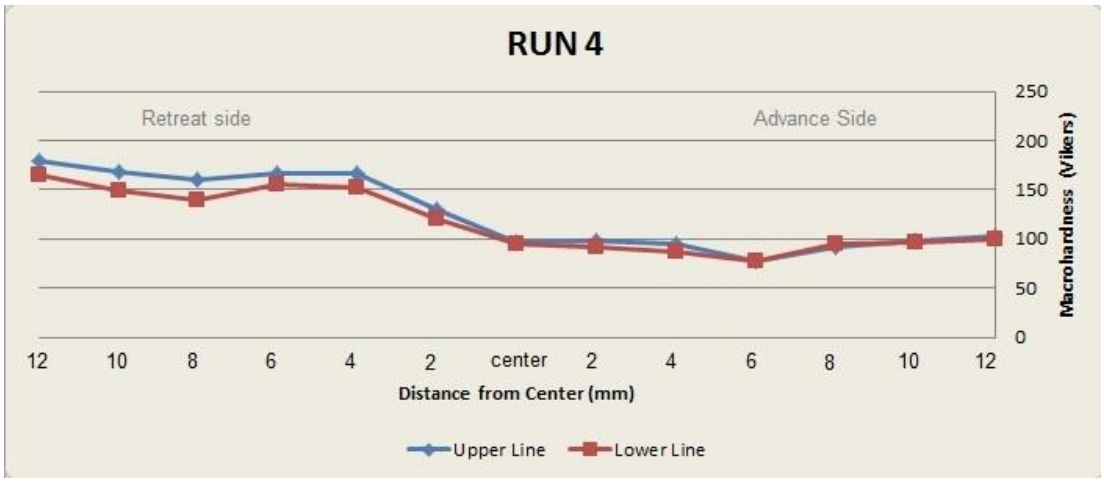
RUN 4
Retreat side
Advance Side
250
200
150
100
50
0
Macrohardness (Vikers)
12 10 8 6 4 2 center 2 4 6 8 10 12
Distance from Center (mm)
Upper Line
Lower Line


RUN 5
Retreat side
Advance Side
250
200
150
100
50
0
Macrohardness (Vikers)
12 10 8 6 4 2 center 2 4 6 8 10 12
Distance from Center (mm)
Upper Line
Lower Line

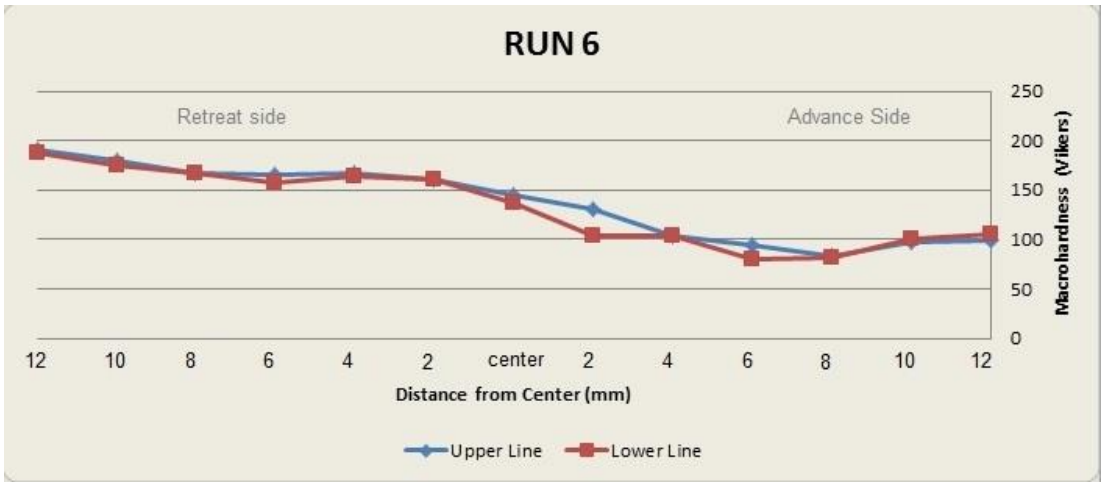
RUN 6
Retreat side
Advance Side
250
200
150
100
50
0
Macrohardness (Vikers)
12 10 8 6 4 2 center 2 4 6 8 10 12
Distance from Center (mm)
Upper Line
Lower Line

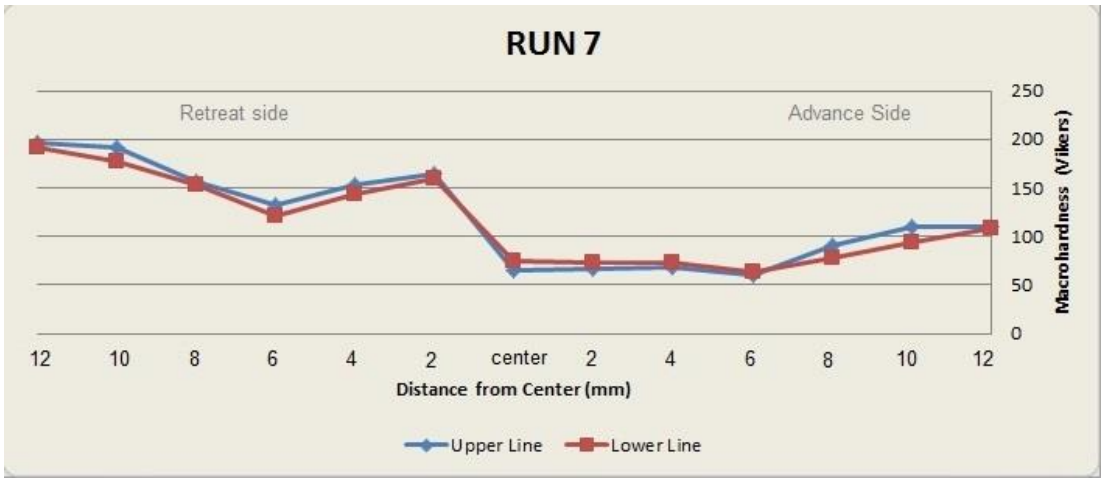
RUN 7
Retreat side
Advance Side
250
200
150
100
50
0
Macrohardness (Vikers)
12 10 8 6 4 2 center 2 4 6 8 10 12
Distance from Center (mm)
Upper Line
Lower Line

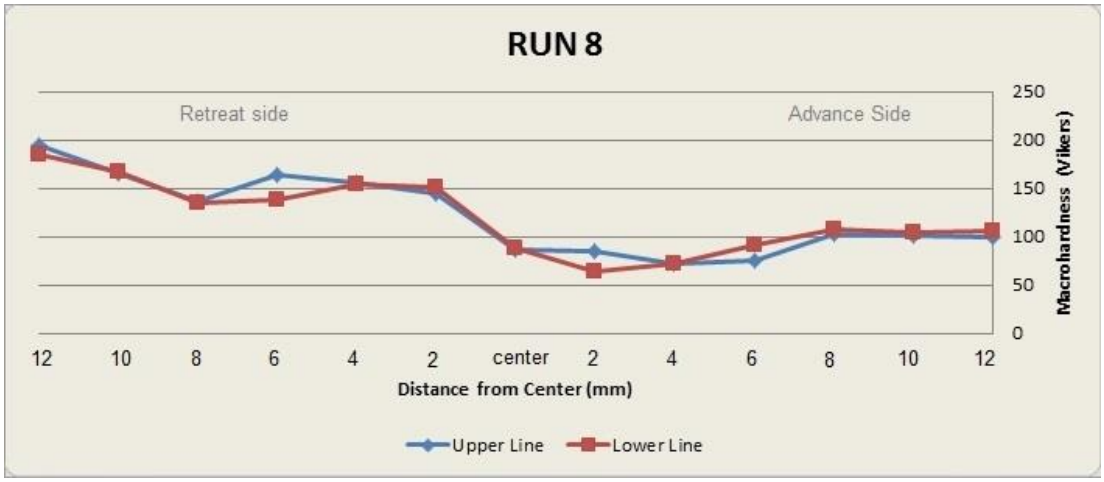
RUN 8
Retreat side
Advance Side
250
200
150
100
50
0
Macrohardness (Vikers)
12 10 8 6 4 2 center 2 4 6 8 10 12
Distance from Center (mm)
Upper Line
Lower Line

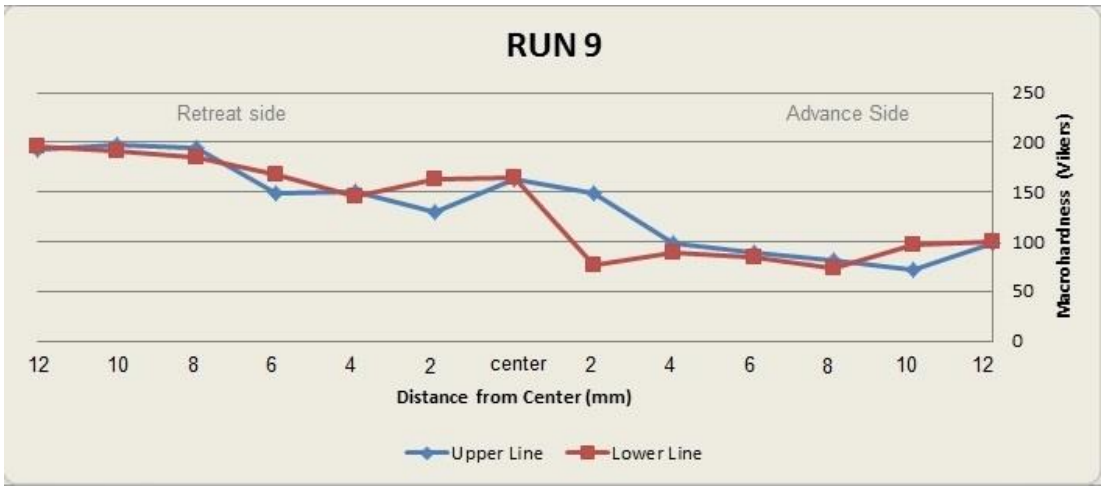
RUN 9
Retreat side
Advance Side
250
200
150
100
50
0
Macrohardness (Vikers)
12 10 8 6 4 2 center 2 4 6 8 10 12
Distance from Center (mm)
Upper Line
Lower Line


RUN 10
Retreat side
Advance Side
250
200
150
100
50
0
Macrohardness (Vikers)
12 10 8 6 4 2 center 2 4 6 8 10 12
Distance from Center (mm)
Upper Line
Lower Line

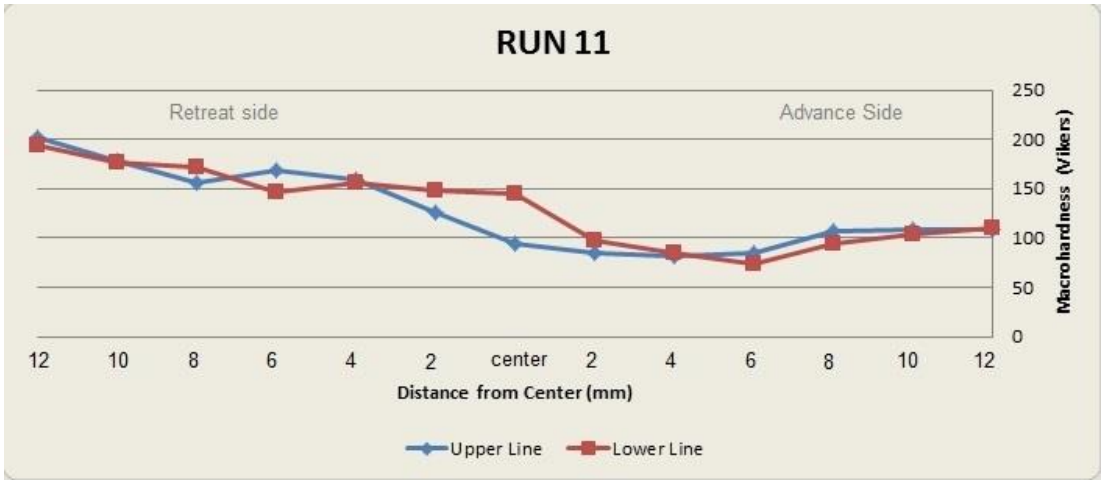
RUN 11
Retreat side
Advance Side
250
200
150
100
50
0
Macrohardness (Vikers)
12 10 8 6 4 2 center 2 4 6 8 10 12
Distance from Center (mm)
Upper Line
Lower Line


RUN 12
Retreat side
Advance Side
250
200
150
100
50
0
Macrohardness (Vikers)
12 10 8 6 4 2 center 2 4 6 8 10 12
Distance from Center (mm)
Upper Line
Lower Line

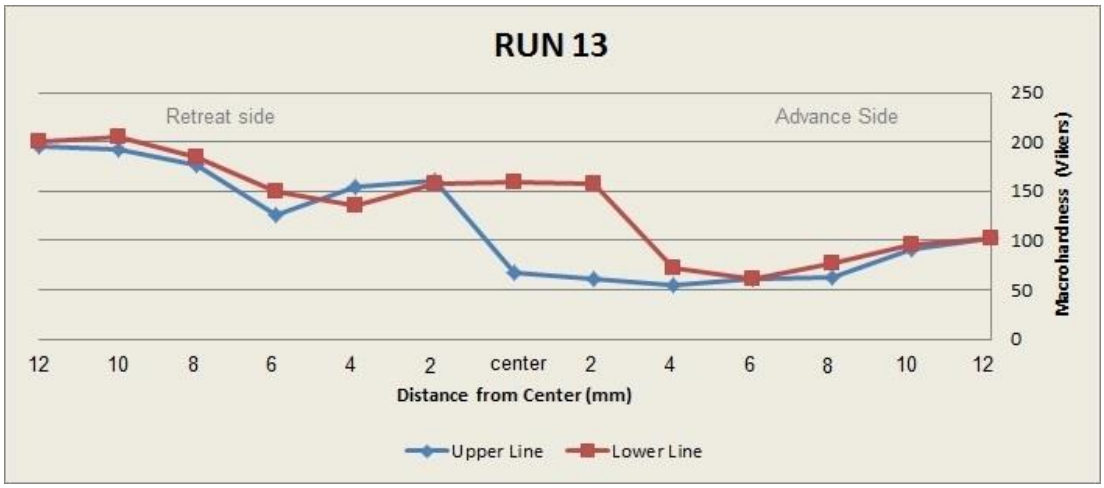
RUN 13
Retreat side
Advance Side
250
200
150
100
50
0
Macrohardness (Vikers)
12 10 8 6 4 2 center 2 4 6 8 10 12
Distance from Center (mm)
Upper Line
Lower Line

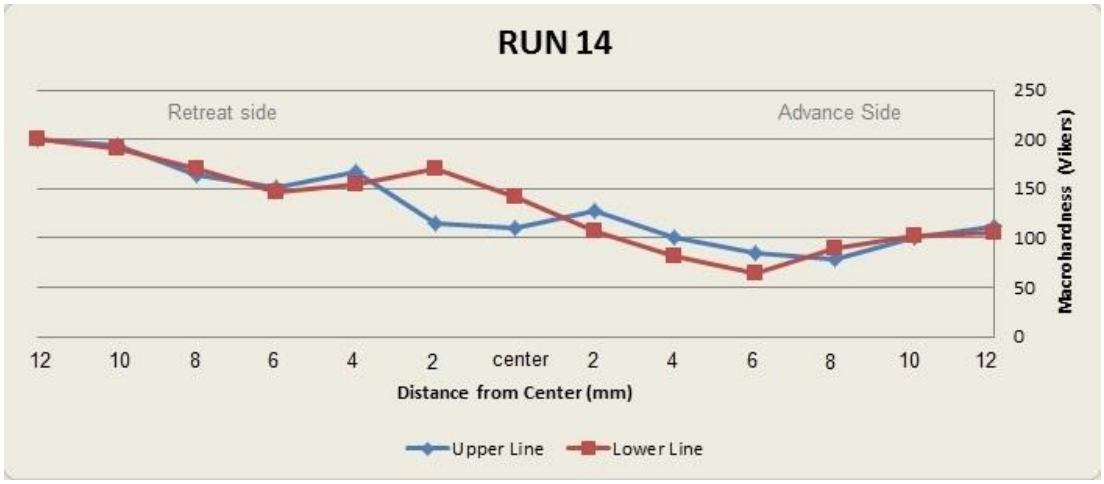
RUN 14
Retreat side
Advance Side
250
200
150
100
50
0
Macrohardness (Vikers)
12 10 8 6 4 2 center 2 4 6 8 10 12
Distance from Center (mm)
Upper Line
Lower Line

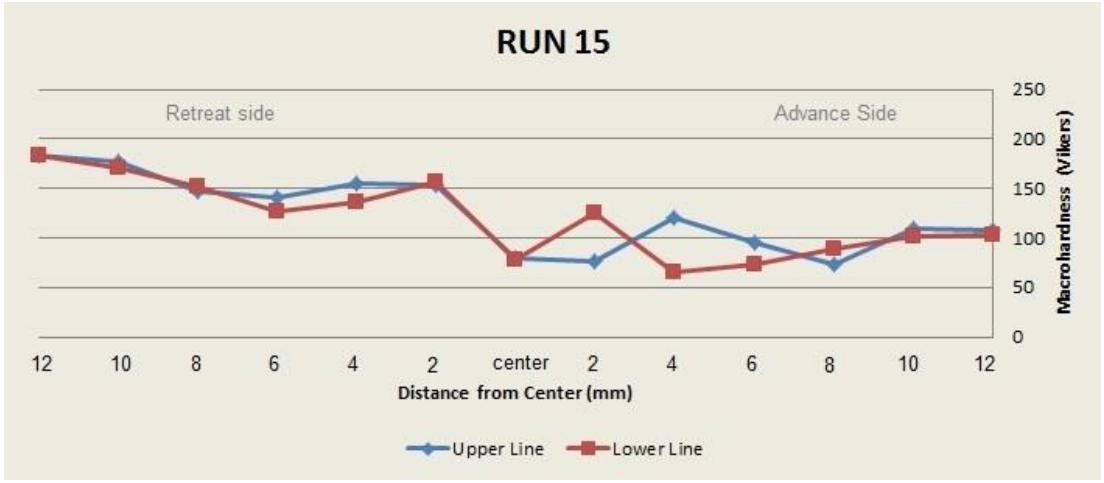
RUN 15
Retreat side
Advance Side
250
200
150
100
50
0
Macrohardness (Vikers)
12 10 8 6 4 2 center 2 4 6 8 10 12
Distance from Center (mm)
Upper Line
Lower Line

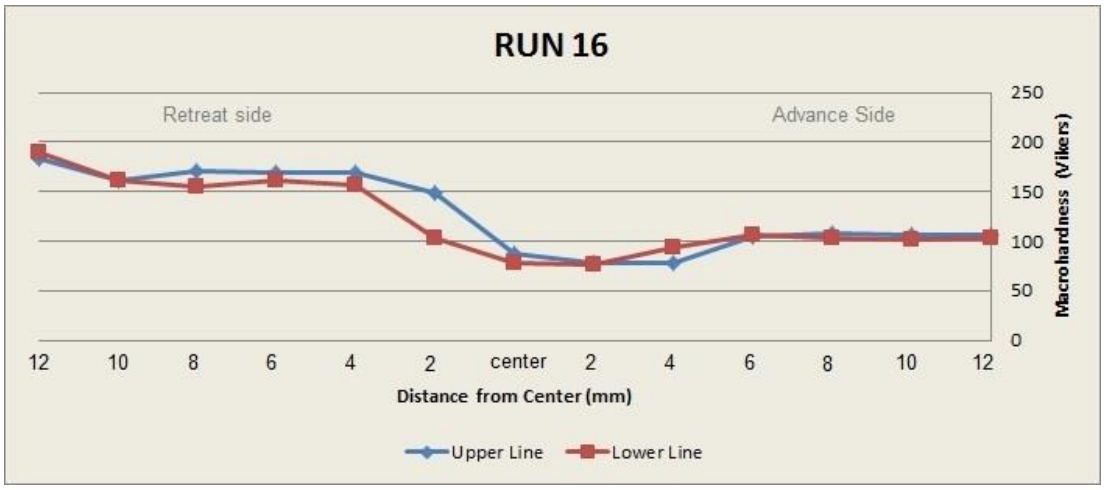
RUN 16
Retreat side
Advance Side
250
200
150
100
50
0
Macrohardness (Vikers)
12 10 8 6 4 2 center 2 4 6 8 10 12
Distance from Center (mm)
Upper Line
Lower Line

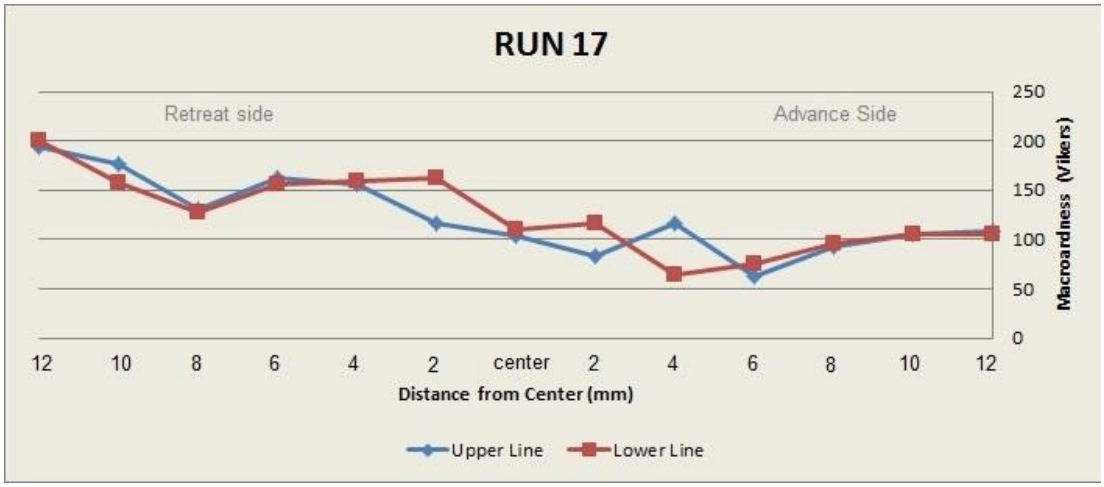
RUN 17
Retreat side
Advance Side
250
200
150
100
50
0
Macroardness (Vikers)
12 10 8 6 4 2 center 2 4 6 8 10 12
Distance from Center (mm)
Upper Line
Lower Line

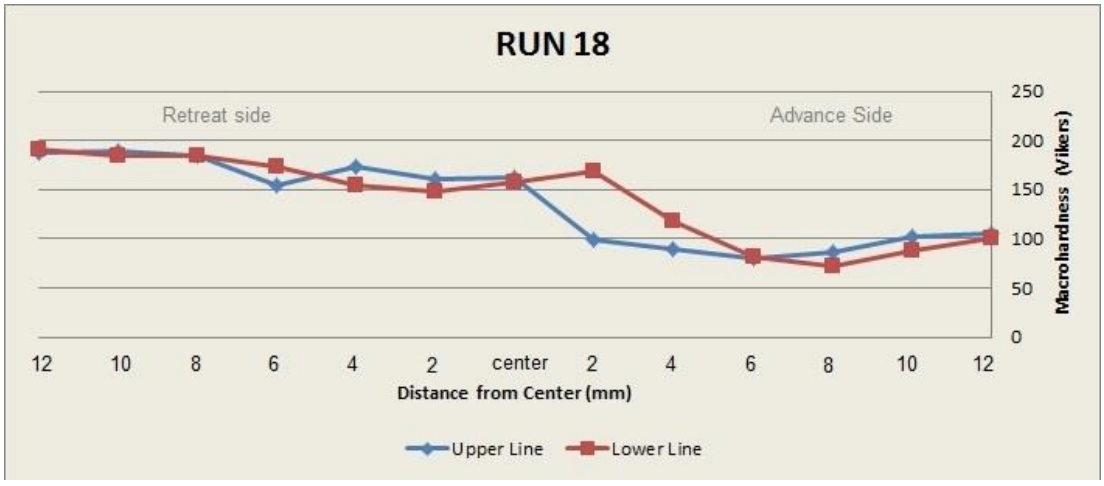
RUN 18
Retreat side
Advance Side
250
200
150
100
50
0
Macrohardness (Vikers)
12 10 8 6 4 2 center 2 4 6 8 10 12
Distance from Center (mm)
Upper Line
Lower Line

Appendix C: Stress-Strain Curve of the Joints

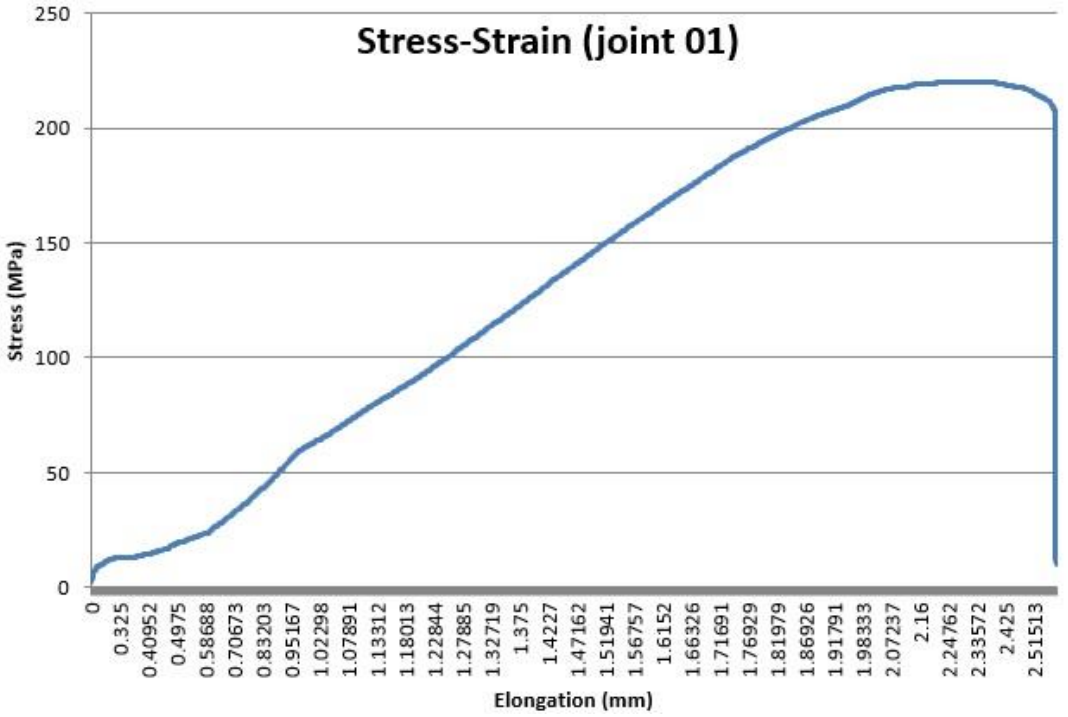

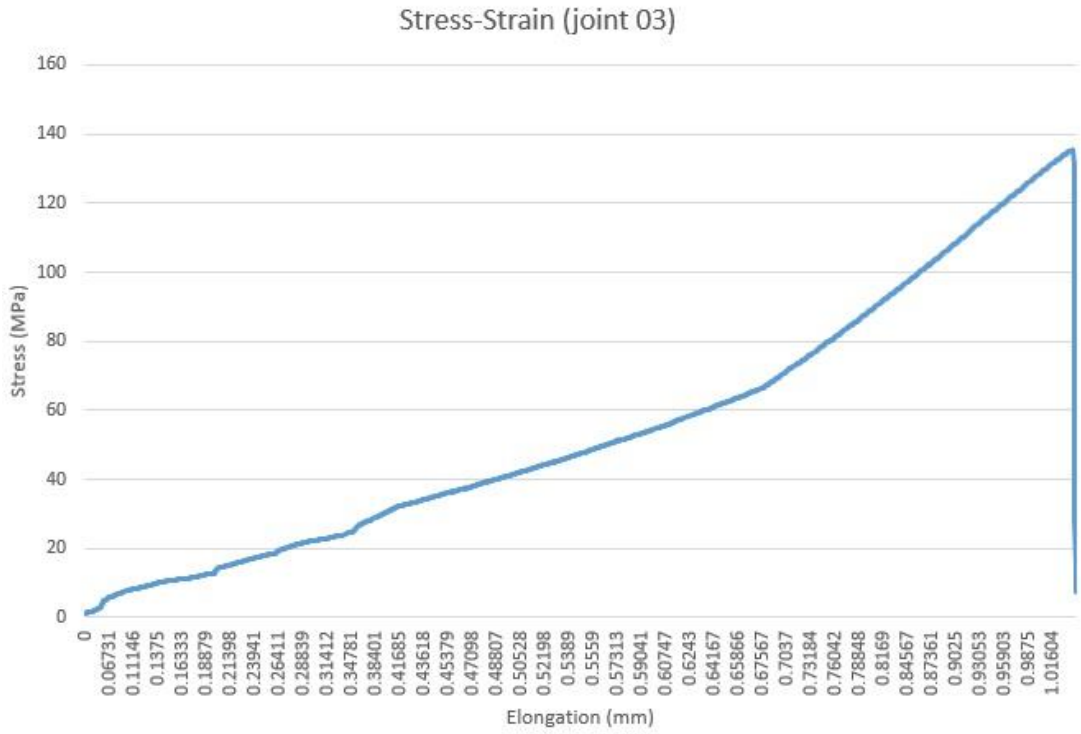

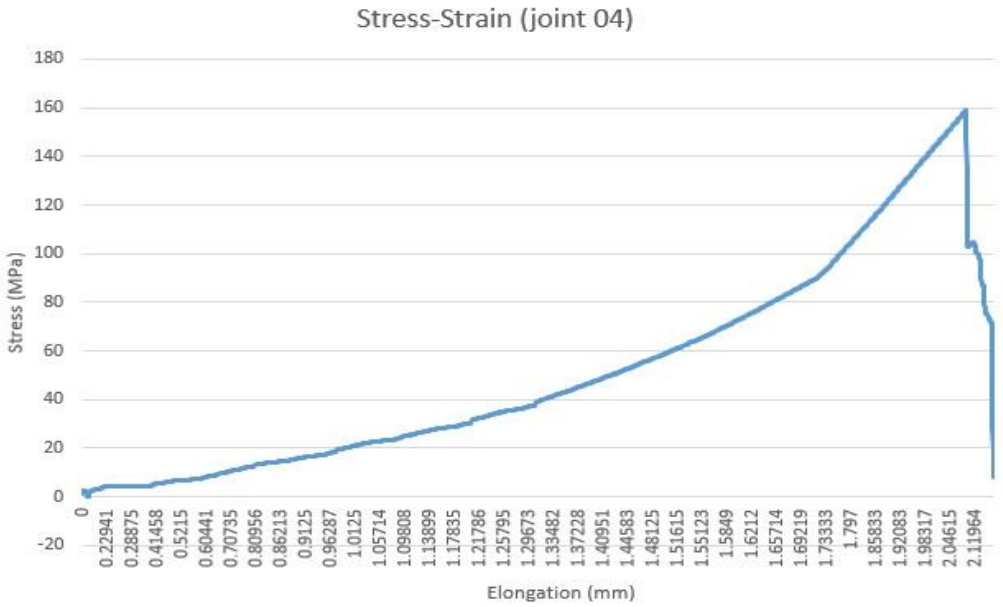
Stress-Strain (joint 04)
Stress (MPa)
Elongation (mm)

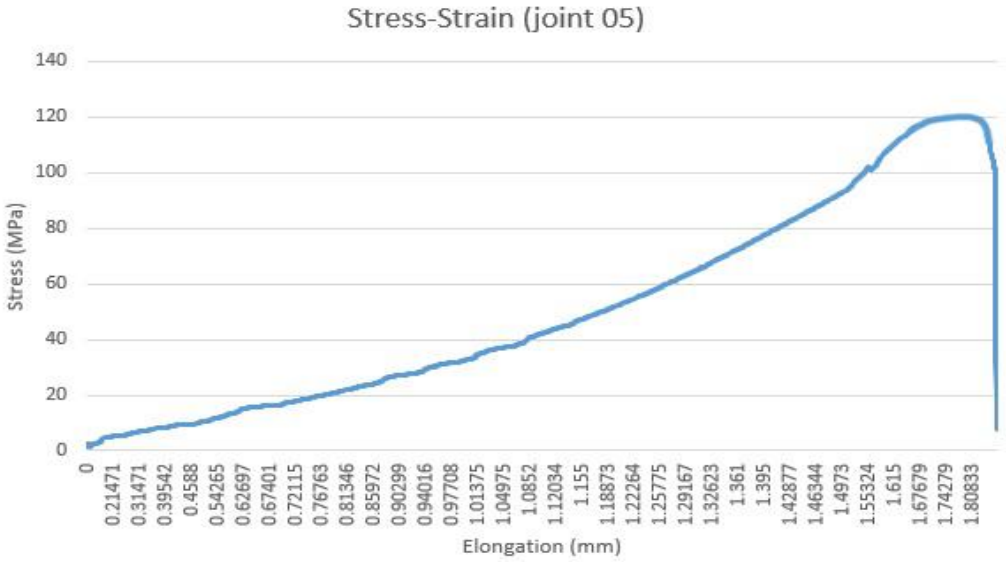
Stress-Strain (joint 05)
Stress (MPa)
Elongation (mm)

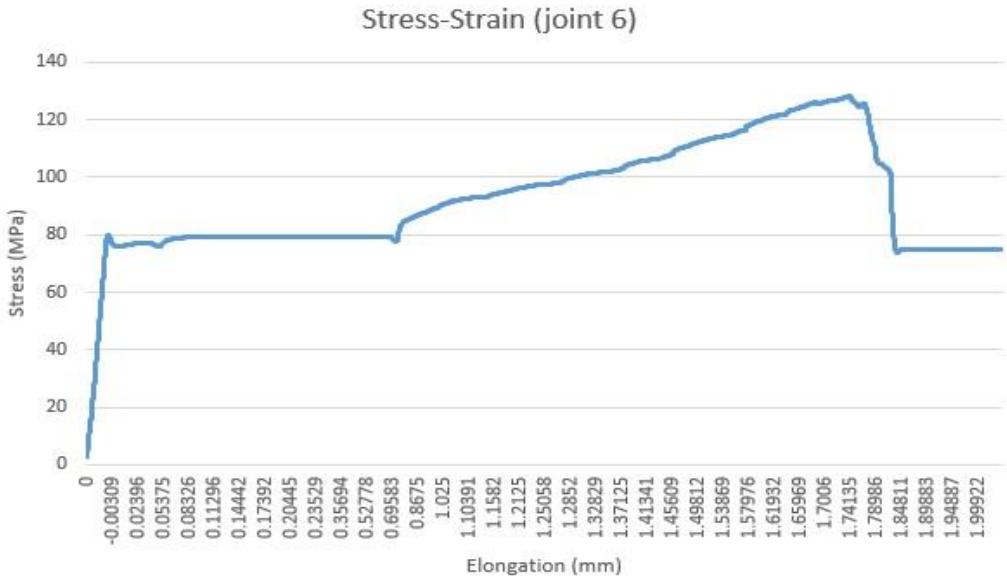
Stress-Strain (joint 6)
Stress (MPa)
Elongation (mm)

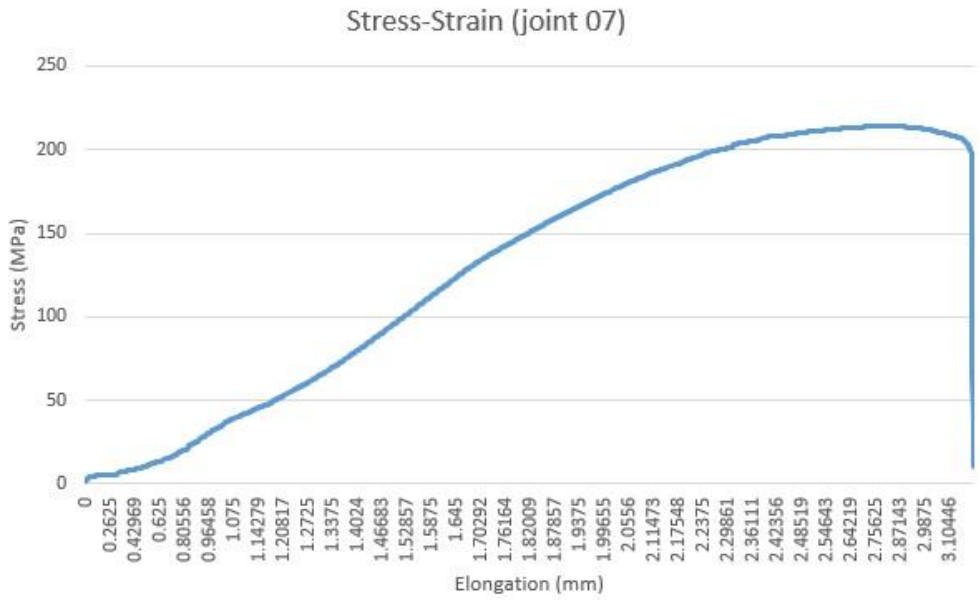
Stress-Strain (joint 07)
Stress (MPa)
250
200
150
100
50
0
0
0.2625
0.42969
0.625
0.80556
0.96458
1.075
1.14279
1.20817
1.2725
1.3375
1.4024
1.46683
1.52857
1.5875
1.645
1.70292
1.76164
1.82009
1.87857
1.9375
1.99655
2.0556
2.11473
2.17548
2.2375
2.29861
2.36111
2.42356
2.48519
2.54643
2.64219
2.75625
2.87143
2.9875
3.10446
Elongation (mm)

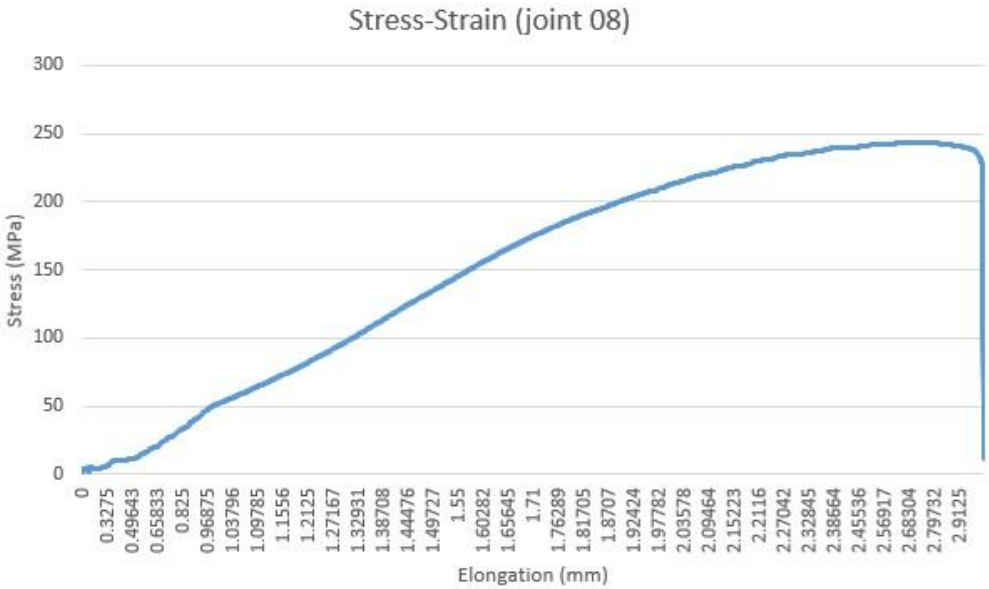
Stress-Strain (joint 08)
Stress (MPa)
300
250
200
150
100
50
0
0
0.3275
0.49643
0.65833
0.825
0.96875
1.03796
1.09785
1.1556
1.2125
1.27167
1.32931
1.38708
1.44476
1.49727
1.55
1.60282
1.65645
1.71
1.76289
1.81705
1.8707
1.92424
1.97782
2.03578
2.09464
2.15223
2.2116
2.27042
2.32845
2.38664
2.45536
2.56917
2.68304
2.79732
2.9125
Elongation (mm)

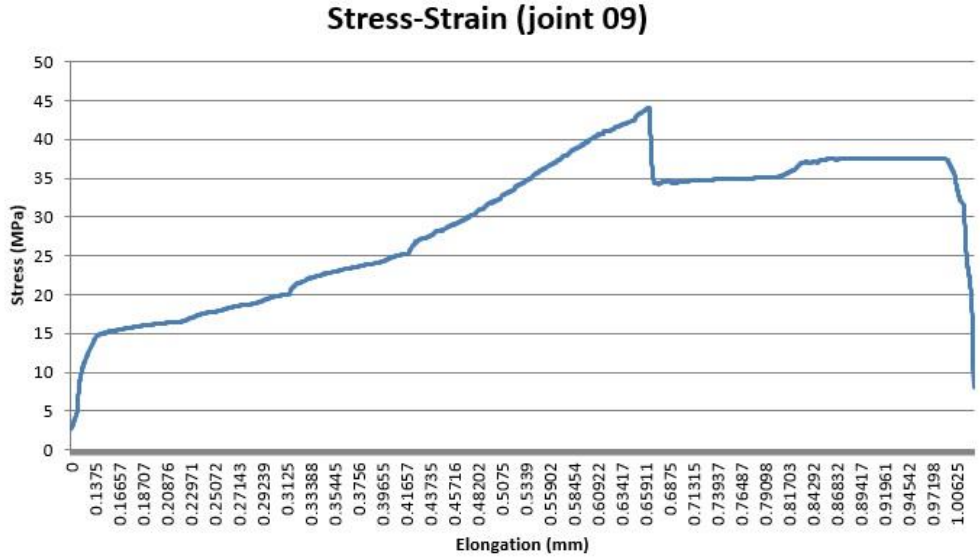
Stress-Strain (joint 09)
Stress (MPa)
50
45
40
35
30
25
20
15
10
5
0
0
0.1375
0.16657
0.18707
0.20876
0.22971
0.25072
0.27143
0.29239
0.3125
0.33388
0.35445
0.3756
0.39655
0.41657
0.43735
0.45716
0.48202
0.5075
0.5339
0.55902
0.58454
0.60922
0.63417
0.65911
0.6875
0.71315
0.73937
0.76487
0.79098
0.81703
0.84292
0.86832
0.89417
0.91961
0.94542
0.97198
1.00625
Elongation (mm)

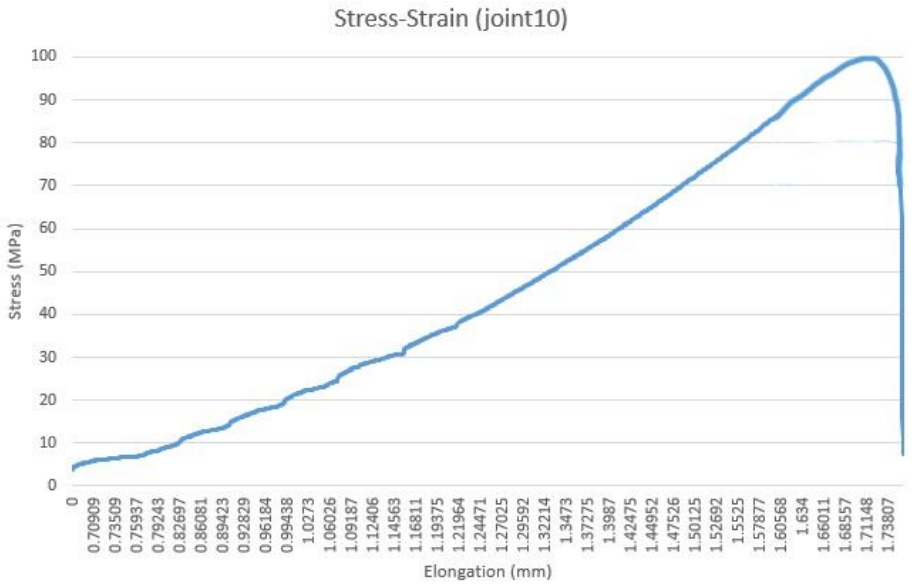
Stress-Strain (joint10)
Stress (MPa)
Elongation (mm)

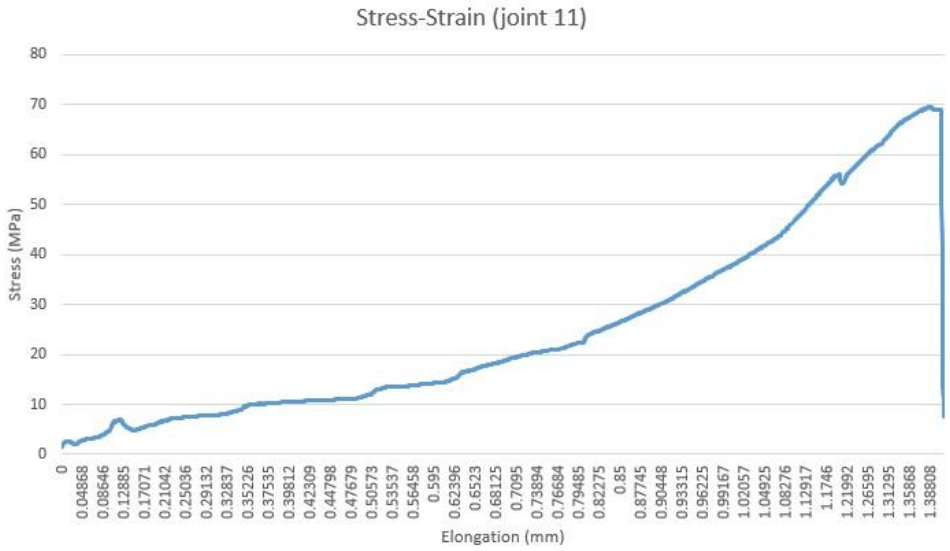
Stress-Strain (joint 11)
Stress (MPa)
Elongation (mm)

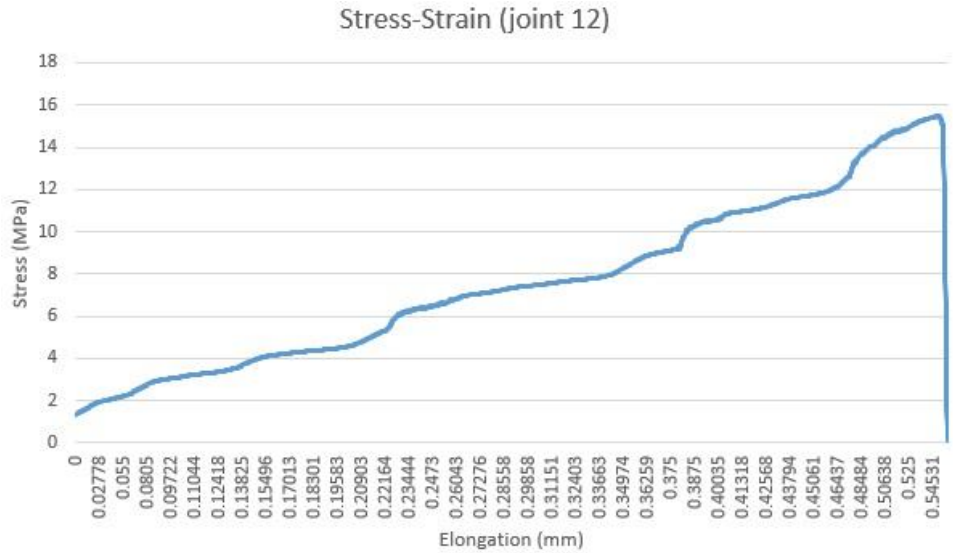
Stress-Strain (joint 12)
Stress (MPa)
Elongation (mm)

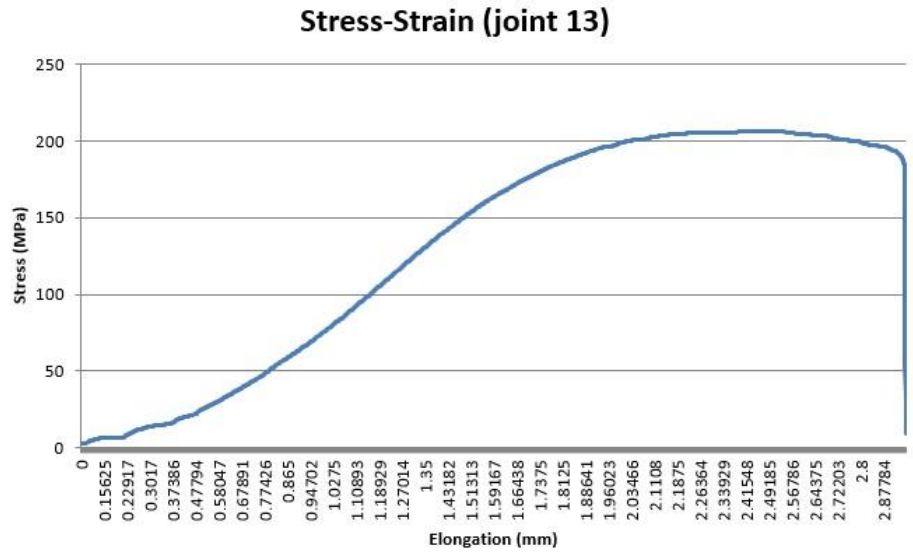
Stress-Strain (joint 13)
Stress (MPa)
250
200
150
100
50
0
0
0.15625
0.22917
0.3017
0.37386
0.47794
0.58047
0.67891
0.77426
0.865
0.94702
1.0275
1.10893
1.18929
1.27014
1.35
1.43182
1.51313
1.59167
1.66438
1.7375
1.8125
1.88641
1.96023
2.03466
2.1108
2.1875
2.26364
2.33929
2.41548
2.49185
2.56786
2.64375
2.72203
2.8
2.87784
Elongation (mm)

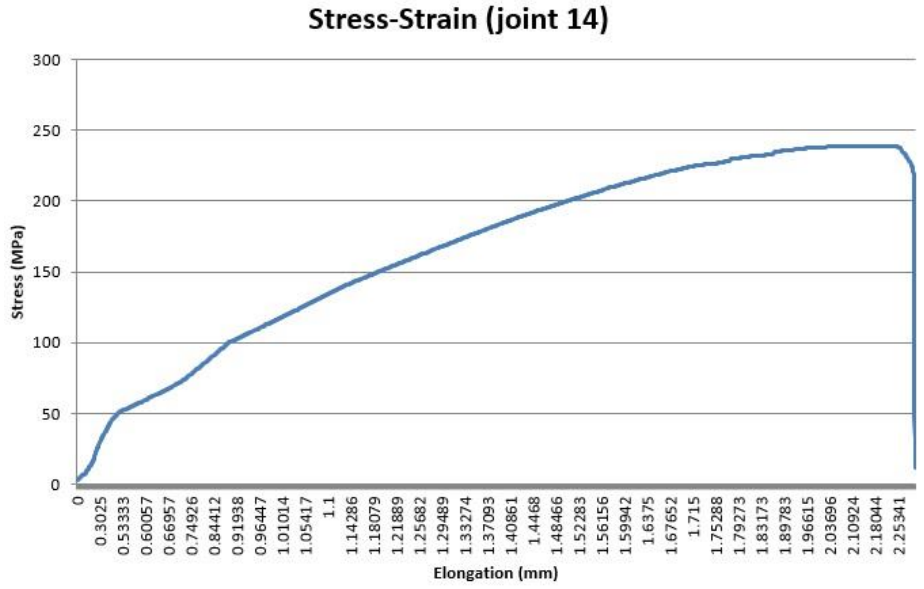
Stress-Strain (joint 14)
Stress (MPa)
300
250
200
150
100
50
0
0
0.3025
0.53333
0.60057
0.66957
0.74926
0.84412
0.91938
0.96447
1.01014
1.05417
1.1
1.14286
1.18079
1.21889
1.25682
1.29489
1.33274
1.37093
1.40861
1.4468
1.48466
1.52283
1.56156
1.59942
1.6375
1.67652
1.715
1.75288
1.79273
1.83173
1.89783
1.96615
2.03696
2.10924
2.18044
2.25341
Elongation (mm)

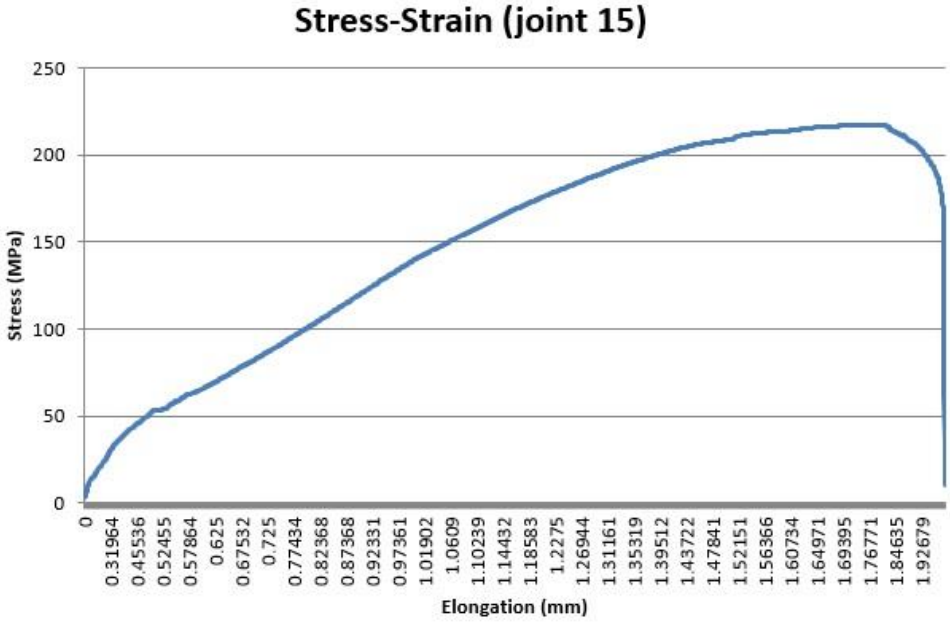
Stress-Strain (joint 15)
Stress (MPa)
250
200
150
100
50
0
0
0.31964
0.45536
0.52455
0.57864
0.625
0.67532
0.725
0.77434
0.82368
0.87368
0.92331
0.97361
1.01902
1.0609
1.10239
1.14432
1.18583
1.2275
1.26944
1.31161
1.35319
1.39512
1.43722
1.47841
1.52151
1.56366
1.60734
1.64971
1.69395
1.76771
1.84635
1.92679
Elongation (mm)

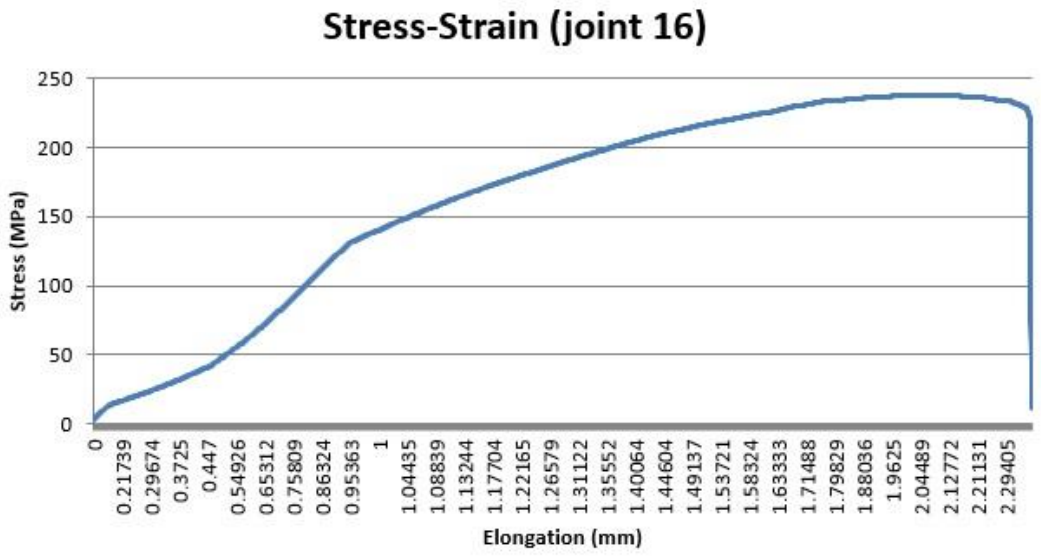
Stress-Strain (joint 16)
Stress (MPa)
250
200
150
100
50
0
0
0.21739
0.29674
0.3725
0.447
0.54926
0.65312
0.75809
0.86324
0.95363
1
1.04435
1.08839
1.13244
1.17704
1.22165
1.26579
1.31122
1.35552
1.40064
1.44604
1.49137
1.53721
1.58324
1.63333
1.71488
1.79829
1.88036
1.9625
2.04489
2.12772
2.21131
2.29405
Elongation (mm)

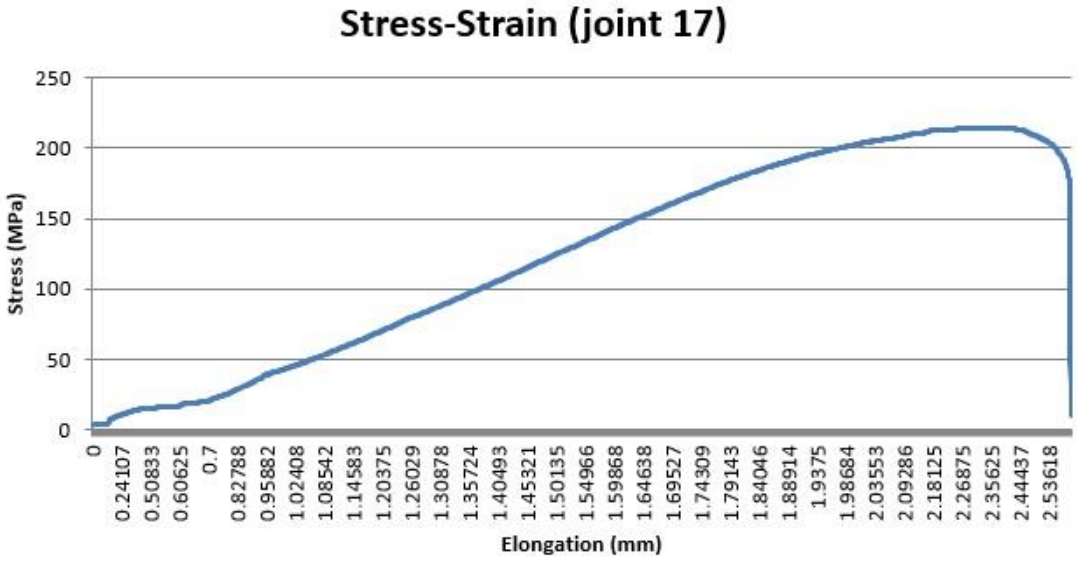
Stress-Strain (joint 17)
Stress (MPa)
250
200
150
100
50
0
0
0.24107
0.50833
0.60625
0.7
0.82788
0.95882
1.02408
1.08542
1.14583
1.20375
1.26029
1.30878
1.35724
1.40493
1.45321
1.50135
1.54966
1.59868
1.64638
1.69527
1.74309
1.79143
1.84046
1.88914
1.9375
1.98684
2.03553
2.09286
2.18125
2.26875
2.35625
2.44437
2.53618
Elongation (mm)

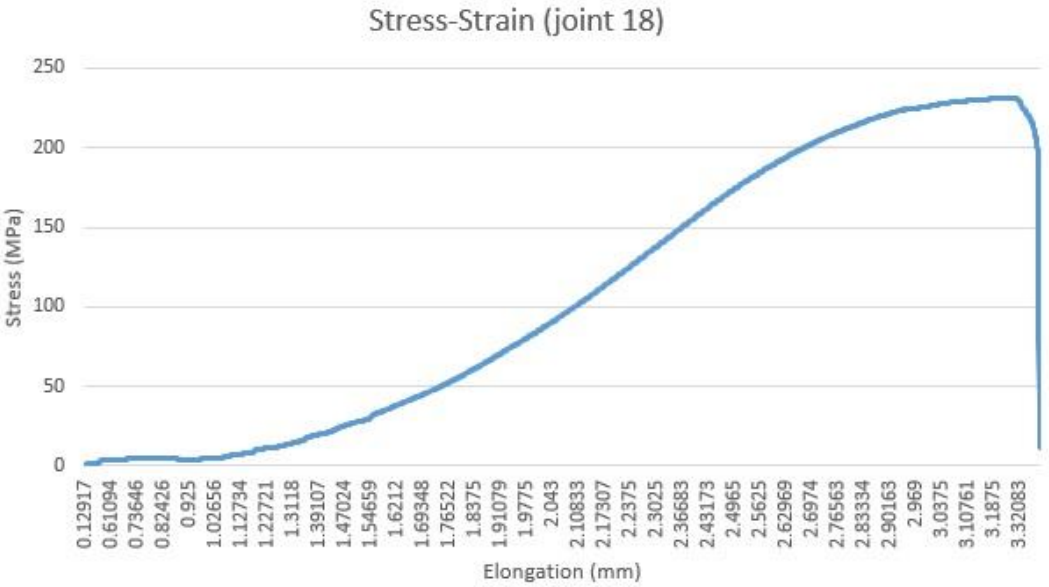
Stress-Strain (joint 18)
Stress (MPa)
250
200
150
100
50
0
0.12917
0.61094
0.73646
0.82426
0.925
1.02656
1.12734
1.22721
1.3118
1.39107
1.47024
1.54659
1.6212
1.69348
1.76522
1.8375
1.91079
1.9775
2.043
2.10833
2.17307
2.2375
2.3025
2.36683
2.43173
2.4965
2.5625
2.62969
2.6974
2.76563
2.83334
2.90163
2.969
3.0375
3.10761
3.1875
3.32083
Elongation (mm)